Doctoral thesis on

Ab initio Molecular Dynamics Simulations of the Structural Response of Solids to Ultrashort Laser and XUV Pulses

Fairoja Cheenicode Kabeer

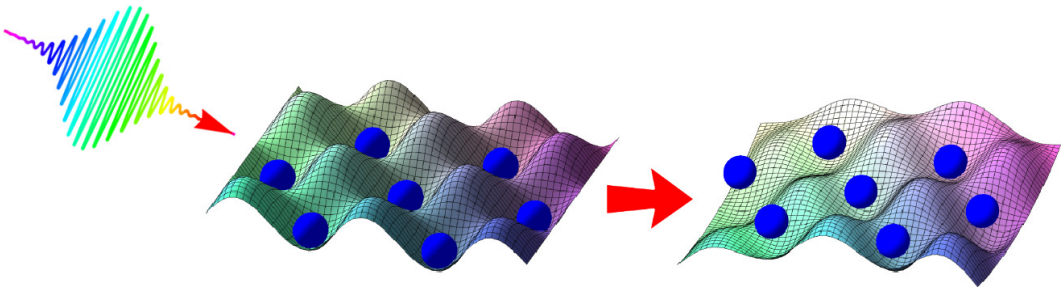

Supervisor : Prof. Dr. Martin E. Garcia
Co-supervisor : Dr. Eeuwe S. Zijlstra

UNIKASSEL
VERSITÄT

Date of defense: 28^{th} October 2014

Ab initio Molecular Dynamics Simulations of the Structural Response of Solids to Ultrashort Laser and XUV Pulses

submitted by

Fairoja Cheenicode Kabeer

Dissertation to fulfill the requirements for the doctoral degree
Doktor der Naturwissenschaften
(Dr. rer. nat.)

Supervisor:
Prof. Dr. Martin E. Garcia

Co-supervisor:
Dr. Eeuwe S. Zijlstra

Department of Theoretical Physics II
Faculty of Mathematics and Natural Sciences
University of Kassel, Germany

Date of defense: 28^{th} October 2014

Ehrenwörtliche Erklärung

Nachname: Vorname:

Hiermit versichere ich, dass ich die vorliegende Dissertation selbstständig, ohne unerlaubte Hilfe Dritter angefertigt und andere als die in der Dissertation angegebenen Hilfsmittel nicht benutzt habe. Alle Stellen, die wörtlich oder sinngemäß aus veröffentlichten oder unveröffentlichten Schriften entnommen sind, habe ich als solche kenntlich gemacht. Dritte waren an der inhaltlich-materiellen Erstellung der Dissertation nicht beteiligt; insbesondere habe ich hierfür nicht die Hilfe eines Promotions beraters in Anspruch genommen. Kein Teil dieser Arbeit ist in einem anderen Promotions- oder Habilitationsverfahren verwendet worden.

Ort, Datum Unterschrift

"Seek Knowledge from the cradle to the grave"

Dedicated with extreme affection and gratitude to

my husband Mr. Sameer Abdul Aziz

and

my parents Mr. V. M. Kabeer and Mrs. Jameela Kabeer

Abstract

The theoretical model and underlying physics described in this thesis are about the interaction of femtosecond-laser and XUV pulses with solids. The key to understand the basics of such interaction is to study the structural response of the materials after laser interaction. Depending on the laser characteristics, laser-solid interaction can result in a wide range of structural responses such as solid-solid phase transitions, vacuum phonon squeezing, ultrafast melting, generation of coherent phonons, etc. During my research work, I have modeled the systems irradiated by low-, medium- and high-laser intensities, and studied different types of structural dynamics of solids at various laser fluences.

In the high fluence regime, I have studied warm dense matter [F. Cheenicode Kabeer, E. S. Zijlstra, and M. E. Garcia, Phys. Rev. B **89**, 100301(Rapid Communication) (2014); E. S. Zijlstra, F. Cheenicode Kabeer, B. Bauerhenne, T. Zier, N. S. Grigoryan, and M. E. Garcia, Appl. Phys. A **110**, 519 (2013)]. The changes in the bonding properties of warm dense noble metals, in particular copper and silver, are analyzed by performing electronic-temperature-dependent density functional theory (DFT) calculations using the all-electron full-potential linearized augmented plane wave code WIEN2k. I found that the extreme hardening of phonon modes shown by noble metals in the warm dense regime cause their relaxation processes to be 3 to 6 times faster than the theoretically expected values. I also found that such a system relaxes thermally (not nonthermally) into a plasma state.

Vacuum phonon squeezed states can be generated at intermediate laser intensities depending upon the electron-phonon coupling and bonding properties of the systems upon laser excitation [F. Cheenicode Kabeer, N. S. Grigoryan, E. S. Zijlstra, and M. E. Garcia, Phys. Rev. B **90**, 104303 (2014)]. I have computed the laser-excited potential energy surfaces of noble metals, namely, copper and silver, by all-electron ab initio theory and analyzed the resulting quantum lattice dynamics. The incoherent lattice heating due to electron-phonon interactions are considered using the generalized two-temperature model. I found phonon hardening, which I attribute to the excitation of s electrons. I demonstrate that this may result in phonon vacuum squeezed states with an optimal squeezing factor of ~ 0.001 at the L-point longitudinal mode. This finding implies that ultrafast laser-induced bond hardening may be used as a tool to manipulate the quantum state of opaque materials, where, so far, the squeezing of phonons below the zero-point motion has only been realized in transparent crystals by a different mechanism. On the basis of my finding I further propose a method for directly measuring bond hardening.

I have studied the coherent phonon dynamics of antimony in the low fluence regime from molecular dynamics simulations using our in-house DFT code 'Code for Highly-excIted Valence Electron Systems (CHIVES)'. I have computed the A_{1g} phonon mode decay constant for the laser fluence leading to electronic temperature, T_e = 3000 K for supercells with N = 72, 144, and 192 atoms and I found that our results are in perfect agreement with experimental data [T. K. Cheng *et al.,* Appl. Phys. Lett, **59**, 1923 (1991)]. I Have extended my studies about the A_{1g} phonon mode decay using the 72 atom supercell for different laser fluences (T_e =1000, 2000, 3000, and 4000 K), in order to analyze the temperature-dependent A_{1g} phonon decay in antimony. The decay channel(s) of the A_{1g} mode are analyzed from phonon-phonon coupling.

Zusammenfassung

Das theoretische Modell und die zugrunde liegende Physik, welche in dieser Arbeit beschrieben werden, befassen sich mit der Interaktion von Femtosekunden Laserpulsen und XUV Pulsen mit Festkörpern. Der Schlüssel zum Verständnis der Grundlagen solcher Interaktionen ist, sich mit der strukturellen Antwort von Materialien nach der Laseranregung auseinanderzusetzen. Abhängig von der Charakteristik des Laserpulses können vielseitige strukturelle Antworten nach solchen Laseranregung auftreten, z.B. solid-solid Phasenübergänge, *vacuum phonon squeezing, ultrafast melting*, oder die Erzeugung kohärenter Phononen. Während meiner wissenschaftlichen Arbeit habe ich Anregungen von verschiedenen Systemen mit niedriger, mittlerer und hoher Laserintensität simuliert und dabei verschiedene strukturelle Dynamiken in Festkörpern studiert.

Bei der Anregung mit relativ hoher Intensität habe ich mich mit dem Phänomen *warm dense matter* ausseinandergesetzt [F. Cheenicode Kabeer, E. S. Zijlstra, and M. E. Garcia, Phys. Rev. B **89**, 100301(Rapid Communication) (2014); E. S. Zijlstra, F. Cheenicode Kabeer, B. Bauerhenne, T. Zier, N. S. Grigoryan, and M. E. Garcia, Appl. Phys. A **110**, 519 (2013)]. Die Änderungen in den Bindungseigenschaften von Edelmetallen, vor allem von Kupfer und Silber, im *warm dense* Zustand, wurden mit der *electronic-temperature dependent density functional theory (DFT)* untersucht, indem Berechnungen mit dem Code WIEN2k gemacht wurden. Ich habe dabei festgestellt, dass das extreme Hartwerden der Phononen-Moden in Edelmetallen, die sich im *warm dense* Zustand befinden, dazu führt, dass die Relaxionsprozesse 3 bis 6 mal schneller sind, als theoretisch vorausgesagt. Ich habe außerdem herausgefunden, dass solch ein System thermisch in einen Plasma-Zustand übergeht.

Vacuum phonon squeezed Zustände können mit mittlerer Laserintensität, abhängig von der Elektron-Phonon-Kopplung und den Bindungseigenschaften des Systems nach der Laseranregung, generiert werden [F. Cheenicode Kabeer, N. S. Grigoryan, E. S. Zijlstra, and M. E. Garcia, Phys. Rev. B **90**, 104303 (2014)]. Ich habe die laserangeregten Potentialenergieoberflächen der Edelmetalle Kupfer und Silber mit Hilfe von *all-electron ab initio* Theorie berechnet und die durch die Laseranregung enstandenen quantenmechanischen Gitterbewegungen analysiert. Das inkohärente Aufheizen des Gitters wurde durch die Elektron-Phonon-Kopplung und durch das generalisierte *two-temperature model* berücksichtigt. Ich habe herausgefunden, dass durch die Anregung der *s*-Elektronen die Phononen Hartwerden, was dazu führt, dass das System in einen *vacuum squeezed* Zustand übergeht. Der optimale *squeezing factor* ist am größten für die longitudinale Mode am L-Punkt und ist von der Größenordnung ~ 0.001. Diese Erkenntnis eröffnet die Möglichkeit der Manipulation von opaquen Materialien mit Hilfe von laserinduzierten Änderungen der Bindungsstärke. Das *squeezing* der Phononen unterhalb der Nullpunktbewegung wurde bis jetzt nur in transparenten

Materialien beobachtet, wobei dort andere Mechanismen zu Grunde liegen. Auf der Basis meiner Erkenntnisse schlage ich außerdem eine neue Methode zur direkten Messung von hartwerdenden Bindungen vor.

Des Weiteren habe ich kohärente Phononen-Dynamik in Antimon nach einer Laseranregung mit niedriger Intensität untersucht. Dazu habe ich unseren *in-house Code "Code for Highly excIted Valence Electron Systems (CHIVES)"* benutzt und die Zerfallskonstante der A_{1g} Phononen für Superzellen mit N = 72, 144 und 192 Atomen bei einer laserinduzierten Temperatur von T_e = 3000 K berechnet. Die Resultate sind in perfekter Übereinstimmung mit den experimentell gewonnenen Daten [T. K. Cheng *et al.,* Appl. Phys. Lett, **59**, 1923 (1991)]. Ich habe die Studie über die A_{1g} Phononen hierbei noch ausgeweitet, indem ich die Zerfallskonstante für die Zelle mit N = 72 Atomen auch für verschiedene elektronische Temperaturen (T_e = 1000, 2000, 3000 und 4000 K) berechnet habe. Die Zerfallskanäle der A_{1g} Phononen habe ich aus der Phonon-Phonon-Kopplung gewonnen.

Acknowledgements

First of all I would like to thank Prof. Dr. Martin E. Garcia for giving me an opportunity to work highly interesting project and benefit from the experience of international atmosphere and collaboration. Only under his supervision was I able to learn the right way of doing research in the field of theoretical physics. It was pleasure to work in his group and I thank him for having confidence in me and for being an excellent and experienced supervisor.

I consider myself lucky to have worked together with Dr. Eeuwe S. Zijlstra. I learned a lot while working with him. He answered all my questions, made uncountable helpful suggestions and gave guidance to solve many difficult problems. His positive and happy attitude was always a great inspiration for me. I want to thank him for his sincere and open-minded character.

I would also like to thank my examiners, Dr. Harald O. Jeschke, Prof. Dr. Martin E. Garcia, Prof. Dr. J.P. Reithmaier and Prof. Dr. Thomas Baumert, who provided encouraging and constructive feedback. It is no easy task, reviewing a thesis, and I am grateful for their thoughtful and detailed comments.

I am very grateful to Naira S. Grigoryan, for her discussions and contributions to the theory of phonon hardening, and for being friendly colleague with a helping hand. I am indebted to Bernd Bauerhenne for his supports to solve the technical problems and for the discussions about the code to generate the dynamical matrices. I would like to thank Tobias Zier for proof reading this thesis and for various usefull comments. A special mention for Dr. Muhammad Tanveer, thanks for being such a dear friend and an awesome colleague.

During the four years of my PhD-work at the Theoretical Physics department of University of Kassel, I was lucky to have a lot of nice people around, that would help me with dozens of different things and without whom achieving a doctor's degree would not have been possible. All members of the research group have contributed to the nice atmosphere to work. Without intense scientific debates during the informal coffee breaks and students paper discussions, many aspects of ultrafast phenomena would never have open to me. I would like to thank all members of the group for being there. It would be incomplete, if I not mention our secretaries Katharina Wedemeyer, Nicole Heitmeier, and Kim Böhling, who did their job very well and were ready to help at any time.

One of the most important ingredient for a theoretical work is computers. I am very thankful to IT-service center of University of Kassel for providing us powerful computer clusters and I appreciate the technical support offered by Mr. Peter Zanger.

Without financial support I couldn't stay abroad, for that I am grateful to University of Kassel, BMBF (German Federal Ministry of Education and Research) and DFG (Deutsche Forschungsgemeinschaft).

Finally, I would probably never have achieved this without the support of my family and friends. I am very lucky to have a wonderful person Sameer Abdul Aziz as my husband. I deeply thank him for his love, unconditional support and patience. I want to express my deep gratitude to my parents and sister for their support and prayers from far away. I met a lot of nice people during my time in Kassel, thanks for sharing nice moments with me. Last but not least I am taking this as an opportunity to thank all my teachers from childhood onwards ...

The utmost gratitude goes to God almighty for my healthy life and life of those who contributed in several ways towards this work.

Contents

List of Figures

List of Tables

CHAPTER 1

Introduction

The field of high-intensity laser-interaction with matter, although barely two decades old, is already bursting with enough exotic phenomena to keep researchers buzy for years to come. Pulse duration have come down from picoseconds ($10^{-12}s$) to femtoseconds ($10^{-15}s$) and less, and its contributing fields are numerous and diverse: They include atomic physics, plasma physics, astrophysics, laser physics, etc. The extreme conditions existing during the laser-matter interactions have posed a continual challenge to both theoreticians and experimentalists alike.

The developments in ultrafast laser techniques offer a considerable number of applications. A complete and exact understanding of the ultrafast dynamical processes which take place during and after an intense excitation of materials still remains a scientific and technological challenge. New and developing experimental techniques such as time-resolved diffuse x-ray diffraction and reflectivity measurements allow to follow the detailed dynamics of solids within the timescale on which the effect of a laser pulse is considered.

The theoretical model and underlying physics described in the present research work are about the interaction of femtosecond-laser and extreme ultraviolet (XUV) pulses with solids. The key to understand the basics of such interaction is to study the structural response of the materials after the laser interaction. By exciting solids appropriately, many different structural changes can be induced. In fact, depending on the laser characteristics (frequency, pulse duration and energy) and density of excited carriers, laser-solid interaction can result in a wide range of reversible and irreversible structural changes such as solid-solid phase transitions, vacuum phonon squeezing, ultrafast melting, generation of coherent phonons, etc. Femtosecond-laser pulses create an extreme nonequilibrium condition in solids in which electrons acquire very high temperatures while the lattice remains cold. This is due to the fact that on the timescale

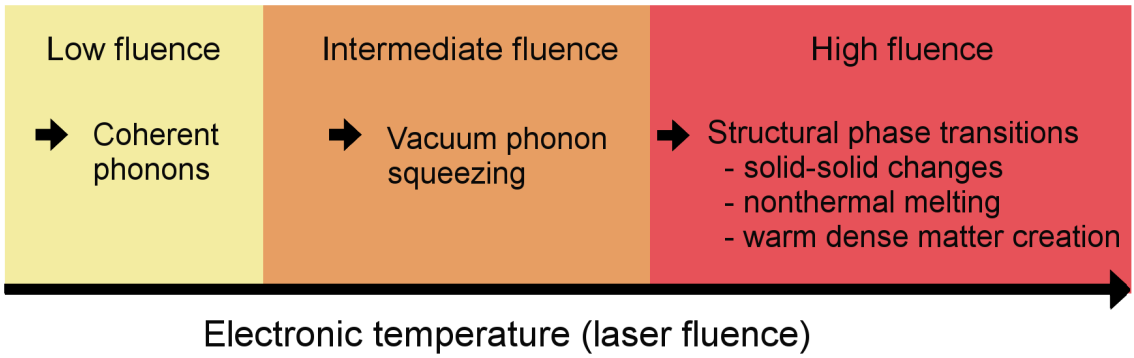

Figure 1.1: Illustration of possible structural responses of solids to femtosecond-laser pulses as a function of its fluences.

on which the laser interacts with solids, the laser energy is initially coupled with the carriers yielding to the creation of electron-hole pairs (the excited electrons and holes thermalize on a very short timescale). The relaxation between electrons and ions takes place usually in some picoseconds after the laser excitation. The electron-phonon coupling time causes delayed heating of the lattice. Therefore, the immediate change of the lattice structure after laser excitation is entirely due to the presence of a hot electron-hole plasma and no thermal heating effects are involved. The presence of hot electrons and holes created by the laser pulse leads to a change in the bonding properties of the solid. The structural response of solids is determined by the rate of energy transfer from the excited electrons to the lattice and the change on the interatomic potential energy landscape. The degree of potential changes depends on the amount of laser energy absorbed by the solid.

The structural response of solid after laser excitation can be divided into three main classes as a function of laser fluences (figure 1.1), namely at low-, medium- and high-intensities. In the case of low laser energy, depending on the symmetry of the system, coherent phonons can be generated. At higher laser energies, vacuum phonon squeezed states can be generated, if the system shows laser-excited bond hardening and has a low electron-phonon coupling constant. When a certain fluence threshold is exceeded, the interaction may give rise to the creation of an extreme transient state, warm dense matter, which afterwards relaxes either thermally into the plasma state or by nonthermal melting.

Among the theoretical and experimental studies regarding structural responses of solids to femtosecond-laser excitation done so far, the following examples attract our attention and are part of the motivations of this theoretical work:

1. In 2011, using time-resolved x-ray absorption spectroscopy, B. I. Cho *et al.* [1] investigated the electronic density of states of warm dense copper produced iso-

chorically through the absorption of an ultrafast optical pulse. The dynamics of the electronic and lattice temperatures were studied with the two-temperature model, using a temperature-dependent electron-phonon coupling parameter [2]. The fast-changing XANES (x-ray absorption near-edge spectroscopy) data indicates that the electron temperature peaks ($\sim$ 10,000 K) with optical excitation, then drops and reaches equilibrium with the lattice ($\sim$ 5000 K) in 10 ps. This is faster than the known electron-phonon coupling constant of copper ($>$ 20 ps). The results suggested that in the WDM regime, the energy exchange rate between electron and atomic vibration is temperature dependent and is about 3 - 6 times faster than previously assumed.

2. In recent years there has been a growing interest in the study of dynamical properties of phonons. 17 years ago, the generation of squeezed phonons by second-order Raman scattering has been predicted [3] and the signature of phonon squeezing has been observed by pump-probe spectroscopy in transmission geometry [4] as well as recently by femtosecond x-ray diffraction [5].

   Garrett *et al.* [4] have shown that in a transparent $KTaO_3$ crystal, a femtosecond-laser pulse can induce a squeezed phonon state. The maximum reported squeezing factor was of the order of 10^{-6}.

   Recently, squeezed state of an opaque medium namely, bismuth have been studied by Johnson *et al.* [5] close to room temperature. Bismuth exhibits laser-induced bond softening [6, 7]. It was found that the variance of the atomic displacements first grows relative to the thermal motion, and then performs a damped oscillations, both processes caused by the laser-induced changes of bond strength. This time evolution is superimposed on a nearly linear increase due to lattice heating produced by incoherent electron-phonon coupling.

3. Excitation of coherent lattice vibrations by an impulsive perturbation of the atomic equilibrium position has been studied in variety of materials [8–12]. In these experiments, femtosecond-laser excitation was used to detect the atomic motion by measuring the oscillations in the optical reflectivity at the phonon frequency that are predicted by the lattice vibrations.

   The first observation of coherent A_{1g} phonons in antimony (Sb) was reported by Cheng *et al.* [8]. Two years later, Zeiger *et al.* [9] observed that in Sb a single exponential decay fails to fit the coherent phonon data, especially for long times. They measured two time constants for coherent phonon decay and reported the short decay time upto 5 ps [9] and the long decay time is not reported yet.

   The study on the dynamics of coherent phonons in bismuth generated by ultrashort laser pulses by Hase *et al.* [11] revealed that the main channel of the

relaxation process of the coherent A_{1g} phonon in bismuth is originating from the phonon-phonon interactions caused by anharmonicity of the lattice potential.

Motivated by the above works, I have studied the ultrafast structural responses of solids after intense femtosecond-laser excitation in three intensity regimes. The aim of this thesis is to provide theoretical approaches combined with simulation tools to study and explain structural dynamics of solids at different laser fluences:

1. Intense ultrashort XUV pulses can be used to create warm dense matter in the laboratory, which then develops to a plasma state. So far, however, it is unknown, whether this transition occurs via heat transfer from hot electrons to cold atoms or nonthermally due to a lattice instability. Here we computed the response of the phonon spectra of noble metals, namely, copper and silver in the presence of XUV-excited core holes and core holes together with very hot electrons. We found that copper and silver show extreme bond hardening in the warm dense regime, which causes faster electron-phonon coupling than the theoretically expected values. We discuss why these findings support the above-mentioned heat transfer scenario, meaning that such a system relaxes thermally (not nonthermally) into a plasma state.

2. Ultrashort optical pulses can both be used to create fundamental quasiparticles in crystals and to change their properties. In noble metals, femtosecond lasers induce bond hardening, but little is known about its origin and consequences. Here we simulate ultrafast-laser excitation of noble metals, in particular copper and silver, at high fluences leading to electronic temperature 6000 K. We find phonon hardening, which we attribute to the excitation of s electrons. We demonstrate that this may result in phonon vacuum squeezed states, with an optimal squeezing factor of ~ 0.001 at the L-point longitudinal mode. The possibility to generate such a quantum mechanical state depends on the electron-phonon coupling and on the bonding properties of the systems. Our finding implies that ultrafast laser-induced bond hardening may be used as a tool to manipulate the quantum state of opaque materials, where, so far, the squeezing of phonons below the zero-point motion has only been realized in transparent crystals by a different mechanism, see [4]. We have explained vacuum phonon squeezing as a direct evidence of bond hardening in noble metals.

3. The third and last purpose of the thesis is the description of the dynamical response of antimony to femtosecond-laser excitation. When a femtosecond-laser pulse interacts with an antimony crystal, due to the presence of hot electrons, large amplitude coherent phonons are excited. At the low fluence laser excitation regime, we have generated and studied the coherent phonon dynamics in

antimony. We analyzed the temperature-dependent A_{1g} phonon decay time on supercells with upto 192 atoms. We have also analyzed the phonon-phonon coupling to know the decay channel(s) of the A_{1g} mode in antimony. To this aim we have performed molecular dynamic simulations using density functional theory.

Although the existing ultrafast x-ray diffraction techniques and time-resolved reflectivity measurements allow monitoring of atomic motions in femtosecond timescales, there is still a considerable uncertainty in the correspondence between the macroscopic quantities and the atomic scale properties of solids. Therefore, there is need to go through the theoretical description of the response of materials to laser excitation. A realistic theoretical description of laser heating of solids must take into account explicitly the electronic as well as the atomic degrees of freedom. The reason is that the system subjected to intense laser excitation will respond strongly to the modification of the interatomic potential or potential energy surface due to the significant electronic excitation. To calculate the potential energy surface which governs the atomic motion, various theoretical methods exist at various level of sophistication: Density functional theory, Hartree-Fock theory, model Hamiltonians (like tight-binding) etc. Among these methods the most accurate ones are the first principle ab initio methods based on density functional theory.

Before presenting the results, in **Chapter 2** I describe the density functional theory and the codes used for the present research work. I present the results in **Chapter 3, 4 and 5**. Finally in **Chapter 6** I give conclusions and discuss about the future work perspectives.

CHAPTER 2

Theory of ab initio calculations to describe laser-excited solids

In the last decades many developments have set the stage for new theoretical understanding of condensed matter physics on the atomic length scale. Four major developments are the basis for most current research in theory and computational methods for electronic structure theory, which are the following:

1. Density functional theory for the electronic ground state and its extension for excited states.
2. Molecular dynamics simulation methods, which can deal directly with the interacting many-body systems of electrons and nuclei.
3. Many-body perturbation methods for the excitation of electronic systems.
4. Computational advances that make realistic calculations feasible and in turn influence the very development of the field.

The study of the electronic structure and properties of laser-irradiated materials is one of the most important subjects in condensed-matter physics for fundamental explorations. At present, a lot of theoretical schemes have been proposed to interpret experimental measurements on laser-excited properties of solids and to predict new effects from first principles (ab initio). A calculation is said to be *ab initio* if it starts from the basic equations of motion without the use of any empirical parameters.

This chapter gives an overview of ab initio theoretical approaches outlining the general aspects to describe laser-excited solids.

2.1 Many-body systems

A solid is a collection of heavy, positively charged nuclei and lighter, negatively charged electrons. The nuclei and electrons are treated as electromagnetically interacting point charges and the exact nonrelativistic many-body hamiltonian becomes:

$$\begin{aligned}\hat{H} = &-\frac{\hbar^2}{2}\sum_i \frac{\nabla^2_{\vec{R}_i}}{M_i} - \frac{\hbar^2}{2}\sum_i \frac{\nabla^2_{\vec{r}_i}}{m_e} \\ &+ \frac{1}{8\pi\epsilon_0}\sum_{i\neq j}\frac{e^2}{|\vec{r}_i - \vec{r}_j|} - \frac{1}{4\pi\epsilon_0}\sum_{i,j}\frac{e^2 Z_i}{|\vec{R}_i - \vec{r}_j|} + \frac{1}{8\pi\epsilon_0}\sum_{i\neq j}\frac{e^2 Z_i Z j}{|\vec{R}_i - \vec{R}_j|}.\end{aligned} \tag{2.1}$$

The mass of the nucleus at $\vec{R}_i$ is M_i and of the electrons at $\vec{r}_i$ is m_e. The first and second terms correspond to the kinetic energy operator of the nuclei and of the electrons, respectively. The last three terms describes the Coulomb interaction between electrons, between electrons and nuclei, and between nuclei, respectively.

In general, it is impossible to solve this problem exactly, without introducing some approximations.

2.2 Level 1: The Born-Oppenheimer approximation

The physical basis for the Born-Oppenheimer approximation [13] is the fact that the masses of atomic nuclei are much larger than the mass of electrons (more than 1000 times). Because of this difference, the electronic motion ($\approx 10^6 m/s$) is considerably faster than the nuclear motion ($\approx 10^3 m/s$). Since the nuclei move so slowly compared to the electrons, it is usually justified to assume that at any moment the electrons will be in their ground state with respect to the instantaneous nuclear configuration. If the nuclei do not move any more, their kinetic energy is zero and the first term in equation 2.1 disappears. The last term reduces to a constant. We are left with the kinetic energy of the electron gas ($\hat{T}$), the potential energy due to electron-electron interactions ($\hat{V}$) and the potential energy of the electrons in the potential of the nuclei ($\hat{V}_{ext}$). The resulting Hamilonian can be written as:

$$\hat{H} = \hat{T} + \hat{V} + \hat{V}_{ext}. \tag{2.2}$$

equation 2.2 is called the electron Hamiltonian. From now on, electrons and nuclei can be treated separately. This decoupling of the electronic and nuclear motion is known as the Born-Oppenheimer or adiabatic approximation.

2.3 Level 2: Density functional theory

Density functional theory is the most widely used approach for quantitative calculations on realistic problems. The quantum many body problem obtained after the Born-Oppenheimer approximation is much simpler than the original one, but still far too difficult to solve. In order to deal with realistic materials, relevant in solid state physics, further approximations have to be made. A historically very important approximation method is the Hartree-Fock method (HF) [14]. It performs very well for atoms and molecules, but for solids it is less accurate. Another breakthrough for computational physics was reached with the development of the density functional theory (DFT) by Hohenberg and Kohn [15] and Kohn and Sham [16].

2.3.1 The theorems of Hohenberg and Kohn

In 1964 Hohenberg and Kohn stated two theorems on which DFT has been built:

First theorem: *There is a one-to-one correspondence between the ground state density $\rho(r)$ of a many-electron system (atom, molecule, solid) and the external potential V_{ext}. An immediate consequence is that the ground state expectation value of any observable $\hat{O}$ is a unique functional of the exact ground state electron density:*

$$\langle\Psi|\hat{O}|\Psi\rangle = O[\rho]. \tag{2.3}$$

Second theorem: *For $\hat{O}$ being the hamiltonian $\hat{H}$, the ground state total energy functional $H[\rho] \equiv E_{V_{ext}}[\rho]$ is of the form*

$$\begin{aligned} E_{V_{ext}} &= \langle\Psi|\hat{T}+\hat{V}|\Psi\rangle + \langle\Psi|\hat{V}_{ext}|\Psi\rangle, \\ &= F_{HK[\rho]} + \int \rho(\vec{r})V_{ext}(\vec{r})d(\vec{r}). \end{aligned} \tag{2.4}$$

*where the Hohenberg-Kohn density functional $F_{HK}[\rho]$ is **universal** for any many-electron system. $E_{Vext}[\rho]$ reaches its **minimal** value (equal to the ground state total energy) for the ground state density corresponding to V_{ext}.*

Here I want to discuss their meaning only, not to prove the theorems: The one-to-one correspondence between the ground state density and the external potential has some important implications. It is obvious that, given the external potential of the system, it is possible to find a unique ground state density for the system. Solving the Schrödinger equation yields the ground state wave function, out of which the ground state density can be calculated. Intuitively, the ground state density seems to contain less information than the ground state wave function. If this were true, the inverse

correspondence (from ground state density to external potential) would not hold. The first theorem of Hohenberg and Kohn, however, states that this correspondence holds as well. In other words: the density contains as much information as the wave function.

As a consequence of the second theorem, and more precisely of the fact that the ground state density minimizes $E_{V_{ext}}[\rho]$, the Rayleigh-Ritz variational method can be used to obtain the ground state density. It is important to note that $E_{V_{ext}}[\rho]$ evaluated for the ground state density corresponding to V_{ext} equals the ground state energy. Only this value of $E_{V_{ext}}[\rho]$ has a physical meaning.

And finally, in the second theorem the Hohenberg-Kohn-functional F_{HK} contains no information on the nuclei and the nuclear positions. Consequently, the functional is the same for all many-electron systems (universal). Unfortunately F_{HK} is not known.

2.3.2 The Kohn-Sham equations

An important step towards applicability of DFT has been made by Kohn and Sham [16]. They proposed to rewrite F_{HK} as follows:

$$F_{HK} = T_0[\rho] + V_H[\rho] + \underbrace{(V_x[\rho] + V_c[\rho])}_{V_{xc}[\rho]}, \tag{2.5}$$

where $T_0[\rho]$ is the kinetic energy functional for noninteracting electrons and $V_H[\rho]$ is the Hartree contribution, which describes the interaction with the field obtained by averaging over the positions of electrons. Although no on-site electron-electron interaction is taken into account, $V_H[\rho]$ is already a good approximation for the electron interaction. Assuming we know the exchange-correlation functional $V_{xc}[\rho]$, we can now write $E_{V_{ext}}$ as:

$$E_{V_{ext}} = T_0[\rho] + V_H[\rho] + V_{xc}[\rho] + V_{ext}[\rho]. \tag{2.6}$$

equation 2.6 can be interpreted as the energy functional of noninteracting particles submitted to two external potentials $V_{ext}[\rho]$ and $V_{xc}[\rho]$, with corresponding Kohn-Sham hamiltonian:

$$\begin{aligned} \hat{H}_{KS} &= \hat{T}_0 + \hat{V}_H + \hat{V}_{xc} + \hat{V}_{ext}, \\ &= -\frac{\hbar^2}{2m_e}{\nabla_i}^2 + \frac{e^2}{4\pi\epsilon_0}\int \frac{\rho(\vec{r}')}{|\vec{r}-\vec{r}'|}d\vec{r}' + \hat{V}_{xc} + \hat{V}_{ext}, \end{aligned} \tag{2.7}$$

with the exchange-correlation operator given by the functional derivative:

$$\hat{V}_{xc} = \frac{\partial V_{xc}[\rho]}{\partial \rho}. \tag{2.8}$$

The Kohn-Sham theorem can now be stated as follows: *The exact ground state density* $\rho(r)$ *of an N-electron system is*

$$\rho(\vec{r}) = \sum_{i=1}^{N} \psi_i^*(\vec{r})\psi_i(\vec{r}), \tag{2.9}$$

where the single-particle wave functions $\psi_i(\vec{r})$ *are the N lowest-energy solutions of the Kohn-Sham equation*

$$\hat{H}_{KS}\psi_i = \epsilon_i\psi_i. \tag{2.10}$$

To obtain the ground state density of the many-body system the Schrödinger-like single-particle equation must be solved. The only unknown contributor to this problem is the exchange-correlation functional. Available approximations for this functional will be treated in the following section.

Two additional remarks have to be made. First, one has to realize that the single-particle wave functions $\psi_i(\vec{r})$ as well as the single-particle energies ϵ_i are no physical electron wave functions or electron energies. They are merely mathematical functions without a physical meaning. Only the total ground state density calculated from these quasi-particles equals the true ground state density. And second, the Kohn-Sham Hamiltonian depends on the electron density through the Hartree and the exchange-correlation term, while the electron density depends on the ψ_i to be calculated. This means that we are actually dealing with a self-consistent problem: The solutions determine the original equation. An iterative procedure is thus needed to solve the problem. In the first iteration a pondered guess is made for the starting density. The latter allows for the construction of the initial Kohn-Sham Hamiltonian. Solving the equation results in a new set of ψ_i and a new electron density. The new density will differ strongly from the previous one. With this density a new $\hat{H}_{KS}$ can be produced. In the end succeeding densities will converge, as will the Hamiltonians. A solution consistent with the Hamiltonian has been reached.

The Kohn-Sham equation proves to be a practical tool to solve many-body problems.

2.3.3 The exchange-correlation functional

As mentioned in the previous section, the Kohn-Sham equation can be solved if the exchange-correlation functional is known. Given the fact that an exact expression is not available and the introduction of an approximation is needed to solve it. Two such often used approximations are LDA (Local Density Approximation) and GGA (Generalized Gradient Approximation). The oldest approximation is the LDA [15–17]

which defines the exchange-correlation functional as:

$$V_{xc}^{LDA}[\rho] = \int \rho(\vec{r})\ \epsilon_{xc}(\rho(\vec{r}))\ d\vec{r}, \tag{2.11}$$

here $\epsilon_{xc}(\rho(\vec{r}))$ stands for the exchange-correlation function (not functional) for the homogeneous electron gas with interacting electrons. The underlying idea is very simple. At each point in space the exchange-correlation energy is approximated locally by the exchange-correlation energy of a homogeneous electron gas with the same electron density as present at that point. LDA is based on the local nature of exchange-correlation and the assumption that the density distribution does not vary too rapidly. In spite of its simplicity, LDA performs quite well even for realistic systems, where the density distribution is a rapidly varying function.

A more sophisticated approach is made with GGA [18,19]. While LDA only depends on the local density $\rho(\vec{r})$ itself, GGA also incorporates the density gradient:

$$V_{xc}^{GGA}[\rho] = \int \rho(\vec{r})\ \epsilon_{xc}(\rho(\vec{r}), |\nabla\rho(\vec{r})|)\ d\vec{r}. \tag{2.12}$$

For GGA, because the density gradient can be implemented in various ways, several versions exist. Moreover, many versions of GGA contain free parameters which have to be fitted to experimental data. Strictly spoken, these GGA versions are no longer ab initio.

In the present work we are using the LDA approximation to study the structural dynamics of laser-irradiated solids.

2.4 Level 3: Solving the equations

The final task is to solve the Kohn-Sham equation that resulted from DFT:

$$\underbrace{\left(-\frac{\hbar^2}{2m_e}{\nabla_m}^2 + \frac{e^2}{4\pi\epsilon_0}\int \frac{\rho(\vec{r}')}{|\vec{r}-\vec{r}'|}d\vec{r}' + \hat{V}_{xc} + \hat{V}_{ext}\right)}_{\hat{H}_{KS}} \psi_m(\vec{r}) = \epsilon_m\psi_m(\vec{r}), \tag{2.13}$$

where m is an integer number that count the number of states. An important step towards the final solution will be to expand the single-particle wave functions in a suitable basis set, say $\{\phi_p^b\}_{p=1,\ldots,P}$:

$$\psi_m = \sum_{p=1}^{P} c_p^m \phi_p^b. \tag{2.14}$$

The wave functions ψ_m belong to a function space which has an infinite dimension: P is therefore in principle infinite. In practise one works with a limited set of basis functions. Note however that the use of a limited basis set makes it impossible to describe ψ_m exactly. It is therefore important to search for suitable limited basis sets, from which good approximations of ψ_m can be constructed. More details on such basis sets will be given further on in this chapter.

By substituting equation 2.14 into equation 2.13 an eigenvalue problem appears:

$$\begin{bmatrix} \cdots & \cdots & \cdots \\ \vdots & \langle\phi_i^b|\hat{H}_{KS}|\phi_j^b\rangle - \epsilon_m\langle\phi_i^b|\phi_j^b\rangle & \vdots \\ \cdots & \cdots & \cdots \end{bmatrix} \begin{bmatrix} c_1^m \\ \vdots \\ c_p^m \end{bmatrix} = \begin{bmatrix} 0 \\ \vdots \\ 0 \end{bmatrix}. \tag{2.15}$$

Diagonalization of the hamiltonian matrix will lead to P eigenvalues and P sets of coefficients that express each of the P eigenfunctions in the given basis. The larger P, the better the approximation of the eigenfunction, but the more time-consuming the diagonalization of the matrix in equation 2.15. Thus the many-body problem of equation 2.1 has thus been reduced to a solvable problem.

As mentioned before, the choice of a good basis set will be very important. The accuracy of the approximation as well as the needed computation time will strongly depend on the basis set. Every system needs its own optimized basis set. Such a basis is very efficient for a specific system. The art of theoretical condensed matter physics is to find an efficient basis set. In the following sections, two families of basis sets will be described — augmented plane waves and Gaussians — that each in their own way describe the wave function.

2.5 Augmented plane wave method (LAPW)

According to the Bloch theorem, eigenfunctions of a periodic Hamiltonian can be expanded in a plane wave basis. However, too many plane wave basis functions are needed to describe the rapidly oscillating behavior of the eigenfunctions near the nucleus, which makes it a very time consuming method. For this reason another approach is needed for the region around atomic nuclei.

The Augmented Plane Wave basis (APW) has been proposed by Slater in 1937 [20]. The APW method is based on the knowledge that the strongly varying, nearly spherical potential and wave functions near an atomic nucleus are very similar to those of an isolated atom. In the region between the atoms the potential is almost constant and hence the wave functions are better described by plane waves. Based on this observation, space is divided in two regions where different basis expansions are

used. Centered around the atomic nuclei (α) nonoverlapping muffin-tin (MT) spheres ($S_{MT,\alpha}$) of radius $R_{MT,\alpha}$ are constructed. The region in between the spheres is called the interstitial region (I). An APW basis function can be defined as:

$$\phi^{\vec{k}}_{\vec{K}}(\vec{r},E) = \begin{cases} \frac{1}{\sqrt{V}}\, e^{i(\vec{k}+\vec{K})\cdot\vec{r}} & \vec{r}\in I \\ \sum_{l,m} A^{\alpha,\vec{k}+\vec{K}}_{lm} u^{\alpha}_{l}(r_i,E) Y^{l}_{m}(\hat{r}_i) & \vec{r}\in S_{MT,\alpha} \end{cases} \tag{2.16}$$

where $\vec{k}$ is the wave vector in the first Brillouin zone, $\vec{K}$ is the reciprocal lattice vector and V the unit cell volume. The $Y^{l}_{m}(\hat{r}_i)$ are spherical harmonics with $\{l,m\}$ angular momentum index and $\vec{r}_i = \vec{r} - \vec{r}_\alpha$ where $\vec{r}_\alpha$ is the atomic position of atom α within the unit cell. $A^{\alpha,\vec{k}+\vec{K}}_{lm}$ are expansion coefficients and $u^{\alpha}_{l}(r_i,E)$ is a solution of the radial Schrödinger equation with spherical averaged crystal potential $V(r)$ centered on the atom, at given energy E:

$$\Big[\frac{\mathrm{d}^2}{\mathrm{d}r^2} + \frac{l(l+1)}{r^2} + V(r) - E\Big] r u^{\alpha}_{l}(r,E) = 0. \tag{2.17}$$

Imposing continuity of $u^{\alpha}_{l}(r,E)$ and the corresponding plane wave on the muffin-tin sphere determines the coefficients $A^{\alpha,\vec{k}+\vec{K}}_{lm}$.

In order to describe an eigenfunction ψ_m of the Kohn-Sham equation 2.13 properly, the corresponding eigenvalue ϵ_m must be used for E. Since ϵ_m is not known yet a guess must be made for the value of E. For this value the APW basis can be constructed and the Kohn-Sham equation can be solved. The guessed E should be a root of this equation. If not, a new value for E must be tried until the chosen value turns out to be an eigenvalue of the equation. This procedure has to be repeated for every eigenvalue.

A general solution to this problem consists in some kind of enhancement of the basis in the muffin-tin spheres in order to remove the energy dependence.

2.5.1 Linearized augmented plane wave method

The eigenenergy (E) problem from the APW method can be solved using the linearized augmented plane wave method (LAPW) [21]. The solution consists of making the energy independent within a certain energy region, where the resulting secular equation 2.15 will become linear in E. An LAPW basis function has the same form as an APW basis function, but to the part of the basis function in the muffin-tin region, the augmentation, has been applied:

$$\phi^{\vec{k}}_{\vec{K}}(\vec{r}) = \begin{cases} \frac{1}{\sqrt{V}}\, e^{i(\vec{k}+\vec{K})\cdot\vec{r}} & \vec{r}\in I \\ \sum_{l,m}\Big[A^{\alpha,\vec{k}+\vec{K}}_{lm} u^{\alpha}_{l}(r_i,E_0) + B^{\alpha,\vec{k}+\vec{K}}_{lm} \dot{u}^{\alpha}_{l}(r_i,E_0)\Big] Y^{l}_{m}(\hat{r}_i) & \vec{r}\in S_{MT,\alpha} \end{cases} \tag{2.18}$$

The APW augmentation has been replaced by a linear combination of the original function u_l^α and its energy derivative $\frac{\partial u_l^\alpha(r_i,E)}{\partial E}$, evaluated at a fixed linearization energy E_0. One can interpret the new term between square brackets (equation 2.18) as a first order Taylor expansion around a fixed energy E_0:

$$u_l^\alpha(r_i,E) = u_l^\alpha(r_i,E_0) + (E-E_0)\dot{u}_l^\alpha(r_i,E_0) + O(E-E_0)^2. \tag{2.19}$$

If the energy E_0 differs slightly from the true band energy E, such a linear combination will reproduce the APW radial function at the band energy. This yields a basis set that is flexible enough to represent all eigenstates in a region around E_0. The coefficients $A_{lm}^{\alpha,\vec{k}+\vec{K}}$ and $B_{lm}^{\alpha,\vec{k}+\vec{K}}$ can be determined by imposing continuity of the LAPW on the muffin-tin sphere.

At this stage, E_0 is still the same for all values of l. We can go one step further by choosing a different E_0, say E_l^α, for every l-value of atom α. In this case E_l^α is normally chosen at the center of the corresponding band. This gives the final definition for an LAPW:

$$\phi_{\vec{K}}^{\vec{k}}(\vec{r}) = \begin{cases} \frac{1}{\sqrt{V}}\, e^{i(\vec{k}+\vec{K})\cdot\vec{r}} & \vec{r}\in I \\ \sum_{l,m}\Big[A_{lm}^{\alpha,\vec{k}+\vec{K}}u_l^\alpha(r_i,E_l^\alpha) + B_{lm}^{\alpha,\vec{k}+\vec{K}}\dot{u}_l^\alpha(r_i,E_l^\alpha)\Big]Y_m^l(\hat{r}_i) & \vec{r}\in S_{MT,\alpha} \end{cases} \tag{2.20}$$

If the energy parameters E_l^α are carefully chosen for each value of the angular momentum, a single diagonalization will yield an entire set of accurate energy bands for the corresponding $\vec{k}$-point. This is a major improvement in comparison with the APW method, where a diagonalization is needed for every energy band.

Two additional parameters have to be introduced to limit these sizes of the basis set as well as the basis functions. The first parameter, l_{max}, controls the size of the LAPW augmentation which consists of an infinite sum over angular momenta l. While the second parameter, the plane wave cutoff K_{max}, determines the size and accuracy of the basis set. A better quantity to judge the accuracy is the dimensionless $R_{MT}^{min}K_{max}$, between the smallest muffin-tin radius and K_{max}. If the smallest muffin-tin radius is increased, the closest point a plane wave can come to a nucleus moves farther away from the nucleus. Less plane waves are needed to describe the remaining, smoother parts of the wave function. R_{MT}^{min} cannot be too large on the other hand, as the spherical harmonics are not suited to describe the wave functions in the region far away from the nuclei. As a consequence, l_{max} and K_{max} control the accuracy of the calculations.

2.5.2 LAPW with local orbitals (LAPW+LO)

An even more efficient method is the Local Orbital (LO) extension to the LAPW method [21]. The electron states located closest to the nucleus (core states) are strongly

bound to the nucleus and behave almost as if they were free atom states. They do not participate in chemical bonding and are entirely contained inside the muffin-tin sphere, which are subjected to the potential of all the other states. States that cross the muffin-tin sphere and thus participate in chemical bonding are called valence states. Unlike the core states, these valence states are treated with LAPW. The LAPW method works very well for describing valence states as long as all states have a different l-value. But the LAPW method fails in a situation, in which two valence states exist with the same l quantum number, say l', but different principle quantum number n. In such a case the state with the lowest n-value lies far below the Fermi level and is a core-like state which is not completely contained inside the muffin-tin sphere. It is called a semi-core state. Constructing a suitable LAPW basis set for this case is difficult, because it is not clear how to choose $E^{\alpha}_{l'}$. This problem is solved in the LAPW+LO method where a new type of basis function, a Local Orbital, is added to the LAPW basis:

$$\phi^{lm}_{\alpha,LO}(\vec{r}) = \begin{cases} 0 & \vec{r} \notin S_{MT,\alpha} \\ \Big[A^{\alpha,LO}_{lm} u^{\alpha}_{l}(r_i, E^{\alpha}_{1,l}) + B^{\alpha,LO}_{lm} \dot{u}^{\alpha}_{l}(r_i, E^{\alpha}_{1,l}) & \\ +C^{\alpha,LO}_{lm} u^{\alpha}_{l}(r_i, E^{\alpha}_{2,l})\Big] Y^{l}_{m}(\hat{r}_i) & \vec{r} \in S_{MT,\alpha} \end{cases} \tag{2.21}$$

A Local Orbital basis function is independent of $\vec{k}$ and $\vec{K}$. It belongs to only one atom (α) and has a specific l-character. For a specific l-value $2l+1$ Local Orbitals are added ($m = -l, -l+1, ..., l$). The Local Orbitals are local in the sense that they are identically zero outside the muffin-tin spheres. The three coefficients $A^{\alpha,LO}_{lm}$, $B^{\alpha,LO}_{lm}$ and $C^{\alpha,LO}_{lm}$ are determined by imposing the constraint that the Local Orbital is normalized and has zero slope at the muffin-tin boundary. The $u^{\alpha}_{l}(r_i, E^{\alpha}_{1,l})$ and $\dot{u}^{\alpha}_{l}(r_i, E^{\alpha}_{1,l})$ are the same as in the regular LAPW method with as linearization energy $E^{\alpha}_{1,l}$, an energy value for the highest of the two valence states. Since the lowest valence state, or semi-core state, resembles a free atom state it will be sharply peaked at an energy $E^{\alpha}_{2,l}$. A single radial function $u^{\alpha}_{l}(r_i, E^{\alpha}_{2,l})$ is therefore included in the Local Orbital, which is sufficient to describe this state.

Adding Local Orbitals will increase the basis set size and consequently also the computation time. Moreover, the slight increase in computation time is largely compensated by the gain in accuracy.

2.5.3 Wien2k-code

The theory of ab initio calculations using plane wave basis function has been discussed. To perform the calculation a software package is needed in which the theory is implemented. More than half of the calculations performed for this thesis were executed with the Wien2k-code, an Augmented Plane Wave + Local Orbitals Program.

The code is divided in two parts: the first part processes the input files while the second part performs a self-consistent calculation. The input routine starts from a structure file containing information on the atomic configuration of the system: lattice parameters, atomic species, atomic positions, muffin-tin radii, etc. In the next step LSTART calculates the atomic densities for all atoms in the unit cell and in combination with the other input files KGEN determines a suitable $\vec{k}$-mesh. And in the final initialization step, DSTART, a starting electron density ρ is constructed based on a superposition of the atomic densities. During this initialization all the necessary parameters are fixed as well: the exchange-correlation approximation (LDA, GGA, LSDA), $R_{MT}K_{max}, l_{max}$ and the energy parameter that separates the core states from the valence states. For an optimal use of computation time a good choice of $R_{MT}K_{max}$ and the $\vec{k}$-mesh is needed.

Once the starting density is generated, the self-consistent calculation can start. This process is divided into several subroutines which are repeated over and over until convergence is reached and the calculation is self-consistent. LAPW0 starts with calculating the Coulomb and the exchange-correlation potential. LAPW1 solves the secular equation for all the $\vec{k}$-values in the $\vec{k}$-mesh by diagonalization of the Kohn-Sham equation. The following subroutine, LAPW2, determines the Fermi-energy. Once this energy is known the eigenfunctions resulting from LAPW1 can be used to construct a valence density:

$$\rho_{val}(\vec{r}) = \sum_{\epsilon_{\vec{k},i}<E_F} \phi^*_{\vec{k},i}(\vec{r})\phi_{\vec{k},i}(\vec{r}). \tag{2.22}$$

The states and energies of the core electrons are calculated separately in a regular atomic calculation in the LCORE subroutine, which results in a total core density ρ_{core}. Both densities, ρ_{core} and ρ_{val}, together give the total density, $\rho_{tot} = \rho_{core} + \rho_{val}$. Since this density often differs a lot from the old density (the density from previous step) ρ_{old} , they are mixed by MIXER to avoid large fluctuations between iterations that would lead to divergence: $\rho_{new} = \rho_{old} \otimes (\rho_{core} + \rho_{val})$. Once the end of the cycle is reached Wien2k checks for convergence between the old and the new density. If they differ from each other a new iteration is started with a new density as input density. This procedure is repeated until the old and new densities are consistent.

2.6 A method based on Pseudopotential and Gaussian basis set

The basic idea that motivates the use of pseudopotentials is that mostly the valence electrons govern the chemical and physical properties of a crystalline system. The

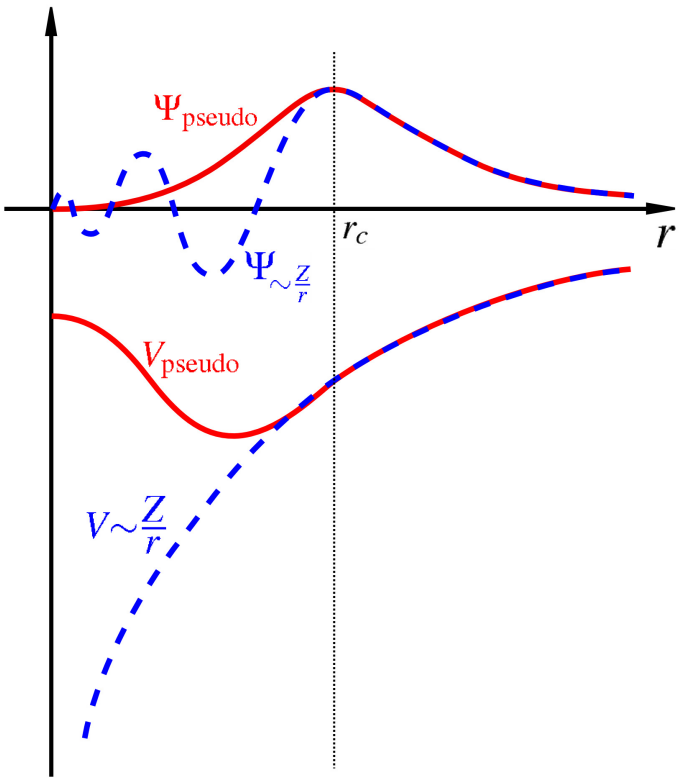

Figure 2.1: Schematic plot of the concept of pseudopotentials in real space [22].

valence electrons in the outermost shells of the atoms are nearly free and involved in bonding with neighboring atoms. Due to screening of the nucleus by the filled core shells, valence electrons are not affected by the full nuclear charge. The lower lying core electrons, however, are rigid and inert, which is typically described as the frozen core approximation. This implies that the low energy electronic states are insensitive to neighbouring atoms, and that they closely resemble the core orbitals of an isolated atom. Such atomic orbitals are known to have a highly oscillatory shape due to the strong interaction with the atomic nucleus, which makes them highly unsuitable to expand in a finite basis set of limited spatial resolutions. As a consequence, it would be convenient to exclude the core states from the many electron problem, subtracting out core-core and core-nucleus energy terms. This is done by replacing the nuclear potential by a pseudopotential, that models the core-valence and valence-nucleus interactions. As a result, there are no orbitals needed for the core states, and the valence is replaced by the so called pseudovalence, which diagonalizes the pseudo-Hamiltonian, i.e. the Hamiltonian that contains the pseudopotential. Since the nucleus is electrostatically shielded by the core states treated via the pseudopotential, the attractive interaction resulting from the pseudopotential is much weaker than the bare nuclear potential with its singularity. This is one reason why the pseudovalence is expected to be much smoother and easier to resolve near the nucleus than the true valence orbitals.

The concept of pseudization is illustrated in figure 2.1. The upper two curves show the radial density distribution of a valence orbital Ψ and its pseudovalence counterpart Ψ_{pseudo}, which is smoother near the nucleus. The pseudopotential V_{pseudo} reproduces the central potential V outside of the core region r_c , but the singularity in the origin is smoothened out. With the pseudopotential method, the computational effort is decreased significantly, not only since the number of orbitals is lowered, but mainly because smaller basis sets can be employed.

2.6.1 Goedecker-Teter-Hutter Pseudopotentials

The norm conserving pseudopotentials proposed by Goedecker, Teter and Hutter (GTH) [23] have some unique properties that make them highly efficient and reliable. A key feature of the GTH pseudopotentials is their purely analytic form with a small number of free parameters. In contrast to most other semilocal pseudopotentials, there is no need to tabulate a radial grid for the local part or any of the projector elements that constitute the separable part. The analytic form is well localized with a smooth shape in both real space and Fourier space. Gaussians serve as a natural choice for the radial functions in the separable part to achieve optimal dual space decay properties. This is why the GTH pseudopotentials are referred as dual-space Gaussian pseudopotentials. As a direct consequence, efficient real space integration of the separable part is possible, which results in only a quadratic scaling with respect to the system size, in contrast to the cubic scaling of a Fourier space integration scheme [24]. The local part uses an error function term (equation 2.23) to cut away the singularity from the central potential within the local radius r_{loc}. Furthermore, a short range potential is added in form of a spherical Gaussian times an even polynomial with up to four coefficients.

The local part $V_{loc}(r)$ of the GTH pseudopotential is given by,

$$\begin{aligned} V_{loc}(r) = -\frac{Z_{ion}}{r}\ \mathrm{erf}\Big(\frac{r}{\sqrt{2}r_{loc}}\Big) + \exp\Big[-\frac{1}{2}\Big(\frac{r}{r_{loc}}\Big)^2\Big] \\ \times\Big[C_1 + C_2\Big(\frac{r^2}{r_{loc}}\Big)^2 + C_3\Big(\frac{r^2}{r_{loc}}\Big)^4 + C_4\Big(\frac{r^2}{r_{loc}}\Big)^6\Big], \end{aligned} \tag{2.23}$$

where erf denotes the error function, Z_{ion} is the ionic charge, r_{loc} is the local radius, which gives the range of the gaussian ionic charge distribution leading to the erf potential, and C_1, C_2, C_3 and C_4 are pseudopotential parameters.

The nonlocal part takes a separable form, where each l component contains several projectors. For a GTH pseudopotential, the weights h^l_{ij} for summing up the projectors as well as a radial length scale r_l are the free parameters of each l- channel in the

separable part. The non-local contribution $V_{nl}(\hat{r}, \hat{r'})$ is

$$V_{nl}(\hat{r}, \hat{r'}) = \sum_{i=1}^{3} \sum_{j=1}^{3} \sum_{m=-l}^{+l} Y_{l,m}(\hat{r})\, P_i^l(r)\, h_{ij}^l\, P_j^l(r')\, Y_{l,m}^*(\hat{r'}), \tag{2.24}$$

where Y_{lm} are the spherical harmonics and l is the angular momentum quantum number. The separable pseudopotentials are computationally much more efficient than conventional forms.

The radial projectors $P_i^l(r)$ are atom centered gaussians, where l takes on the values 0,1,2,... for s,p,d,... orbitals,

$$P_i^l(r) = \frac{\sqrt{2}\, r^{l+2(i-1)}\, \exp\left[-\frac{1}{2}(\frac{r}{r_l})^2\right]}{r_l^{l+\frac{(4i-1)}{2}} \sqrt{\Gamma\left[l+\frac{(4i-1)}{2}\right]}}, \tag{2.25}$$

here Γ denotes the gamma function. The projectors satisfy the normalization condition,

$$\int_0^\infty P_i^l(r)\, P_i^l(r)\, r^2\, dr = 1. \tag{2.26}$$

The nonlocal potential converges rapidly to zero outside the core region.

2.6.2 Cartesian Gaussian functions

For our atomic DFT code that solves the Kohn Sham equations in the presence of a pseudopotential, a Gaussian basis set is employed. As discussed before, the pseudopotential method results in smooth wavefunctions, such that the discretization of the Kohn Sham orbitals with some ten to thirty Gaussians centered on the atom is perfectly accurate. The use of the Gaussian basis set allows to tackle a general eigenvalue problem of conveniently low dimensionality. This has to be done iteratively to solve the Kohn Sham equations self consistently.

We can write an unnormalized cartesian gaussian function [25, 26] centered at $A = \{A_x, A_y, A_z\}$ as

$$\phi(r, \alpha, n, A) = (x - A_x)^{n_x}\, (y - A_y)^{n_y}\, (z - A_z)^{n_z}\, \exp\Big[-\alpha(r - A)^2\Big], \tag{2.27}$$

with the coordinates of electrons $r = (x, y, z)$, orbital exponents α and $n = n_x + n_y + n_z$ is a non-negative integer, which denotes the angular momentum index, such that $n_x + n_y + n_z$ = 0,1,2,... for s,p,d,...

Properties of Gaussian functions:

1). Product of two Gaussian functions located at A and B is another Gaussian located at a point P, somewhere between A and B. It can be expressed as,

$$\begin{aligned}\phi(r,\alpha,a,A)\cdot\phi(r,\beta,b,B) &= (x-A_x)^{a_x}\,(y-A_y)^{a_y}\,(z-A_z)^{a_z}\,\exp\Big[-\alpha(r-A)^2\Big]\\ &\times (x-B_x)^{b_x}\,(y-B_y)^{b_y}\,(z-B_z)^{b_z}\,\exp\Big[-\beta(r-B)^2\Big],\\ &= \exp\Big[-\frac{\alpha\beta}{\alpha+\beta}\mid A-B\mid^2\Big]\,\exp\Big[-(\alpha+\beta)\mid r-P\mid^2\Big].\end{aligned} \tag{2.28}$$

with $P=\frac{\alpha A+\beta B}{\alpha+\beta}$.
2). The derivative of a Gaussian function can be expressed as a sum of Gaussians of higher and lower angular values.

$$\frac{\partial}{\partial A}\phi(r,\alpha,a,A) = 2\alpha\;\phi(r,\alpha,a+1,A) - N(a)\;\phi(r,\alpha,a-1,A). \tag{2.29}$$

Two-center overlap integrals:

Two-center overlap integrals over unnormalized cartesian Gaussian functions are of the form:

$$\langle a\mid b\rangle = \int_{-\infty}^{+\infty}\;\phi(r,\alpha,a,A)\;\phi(r,\beta,b,B)dr, \tag{2.30}$$

and are located at A and B having orbital exponents α and β respectively.

The recurrence formula for $\langle a+1\mid b\rangle$ which will be used to generate the two-center overlap integrals over s, p and d cartesian Gaussian functions (see Appendix A for the derivation) is given by,

$$\langle a+1\mid b\rangle = (P-A)\;\langle a\mid b\rangle + \frac{N(a)}{2(\alpha+\beta)}\;\langle a-1\mid b\rangle + \frac{N(b)}{2(\alpha+\beta)}\;\langle a\mid b-1\rangle. \tag{2.31}$$

Recurrence relations let us efficiently calculate two-center overlap integrals of higher angular values using previously obtained results with lower angular values (see Appendix A). The overlap integral between two s orbitals centered at A and B, can be written as the following,

$$\begin{aligned}\langle s\mid s\rangle &= \int_{-\infty}^{+\infty}\;\phi(r,\alpha,0,A)\;\phi(r,\beta,0,B)\;dr,\\ &= \Big(\frac{\pi}{\alpha+\beta}\Big)^{\frac{3}{2}}\;\exp\Big[-\frac{\alpha\beta}{\alpha+\beta}\mid A-B\mid^2\Big].\end{aligned} \tag{2.32}$$

The overlap integral between s orbital centered at A with the projector of s orbital centered at B can be calculated by,

$$\langle s \mid r^2 s\rangle = \frac{\partial}{\partial\beta}\big(\langle s \mid s\rangle\big). \tag{2.33}$$

2.6.3 Code for Highly-excIted Valence Electron Systems (CHIVES)

During the last years, our group (mainly Eeuwe S. Zijlstra) has developed a density-functional-theory code, 'Code for Highly-excIted Valence Electron Systems' (CHIVES), based on localized basis functions, which provides a more natural description of laser-excited solids and is orders of magnitude faster than other existing codes [27]. This is an essential advantage, since it permits us to perform ab initio molecular dynamics simulations on relatively large supercells and to analyze the pathways of the atoms immediately after laser excitation.

Treatment of core electrons

In CHIVES the electrons are subdivided into core electrons and valence electrons. The electronic structure of the core electrons is not explicitly computed in CHIVES, but their effects on the valence electrons are described by pseudopotentials. we implemented a relativistic pseudopotential of [24], which is of the Goedecker-Teter-Hutter type.

Treatment of valence electrons

Valence electrons in CHIVES are described in terms of an uncontracted atom-centered Gaussian basis set. The basis functions are characterized by Gaussian exponents. By multiplying a Gaussian function, $e^{-\beta r^2}$, by 1, by x, y, and z, or by xy, xz, yz, x^2-y^2, and $2z^2-x^2-y^2$ we obtain one s-type, three p-type, or five d-type Gaussian basis functions in which the angular momentum is included for in the exponent β. The basis set defines, how many different exponents and which types of Gaussian functions for every exponent are included.

Figure 2.2: Periodic table with elements for which pseudopotentials are presently implemented in CHIVES.

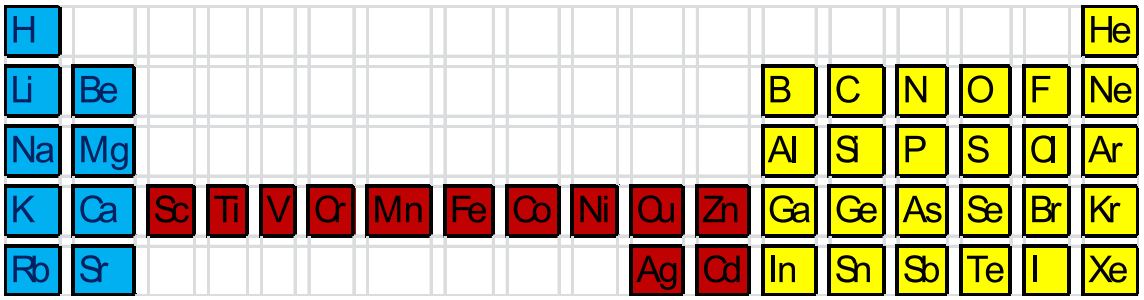

Optimization of basis sets

An uncontracted atom-centered Gaussian basis set can be fully specified by its Gaussian exponents. In order to perform fast, large-scale molecular dynamics simulations for a given system, we first have to find a basis set that is relatively small but still describes all physical effects of interest with sufficient accuracy, which is a nontrivial and rather cumbersome task. The exponents were optimized in the following way [28]: To begin with we choose a small increment, typically 0.01 or 0.1 a_0^{-2}. In a loop we first increase and then decrease each of the exponents from its present value. Every time when the total energy of the reference system decreased, the change in the exponents are accepted, otherwise they are rejected. We continued to loop over all exponents until none of them would vary any more. Then the increment is halved and the whole procedure is repeated. We stop optimizing the exponents when the increment become smaller than $10^{-7}a_0^{-2}$.

Usually Gaussian basis set exponents are optimized for atoms. Two recent publications [28, 29] have, however, indicated that molecular-optimized basis sets tend to be more localized and less linearly dependent. Besides these advantages, it is elegant that one can use the same reference system for all s-, p- and d-type basis functions and polarization orbitals.

Total energies were computed nonrelativistically and nonmagnetically in the local density approximation [30]. Electronic occupation numbers were assigned according to a Fermi-Dirac distribution with electronic temperature T_e. Naturally, the electronic Helmholtz free energy term $-T_eS_e$, where S_e is the electronic entropy, was included in the expression for total energy.

During my PhD, I have implemented the pseudopotential and Two-center overlap integrals upto d orbitals (see Appendix A for the expressions) in CHIVES. The list of elements that can currently be treated by CHIVES is given in figure 2.2. In this thesis, I present recent remarkable results obtained using WIEN2k and CHIVES.

2.7 Laser-excited potential energy surfaces

The structural response of a material to an ultrashort laser pulse is mostly indirect, i.e., via electrons and can best be understood by introducing the concept of a laser-excited potential energy surface. In the Born-Oppenheimer approximation, the ground-state potential energy surface $U_0(\{\vec{R}_i\})$ is obtained after solving the electron problem, i.e., from the ground state energy of the electronic system. Now, in the laser-excited solid the electrons will have a well-defined temperature T_e. Thus, solving the electron problem in this case means determining the function which uniquely describes electron at a given temperature, which is no longer the ground-state energy but the Helmholtz free energy of the electrons $F_e(\{\vec{R}_i\}, T_e(t))$, which in temperature-dependent density functional theory is given by

$$\begin{aligned} F_e(\{\vec{R}_i\}, T_e(t)) = \sum_m n(\epsilon_m, t)\epsilon_m + E_{xc}[\rho(r)] - \int V_{xc}(r)\rho(r)dr \\ -\frac{1}{2}\int \frac{\rho(r)\rho(r')}{|r-r'|}drdr' + V_{II}(\{R_i\}) - T_e(t)S_e(t), \end{aligned} \tag{2.34}$$

where $n(\epsilon_m, t)$ are the occupations of the electronic Kohn-Sham levels ϵ_m. Due to the presence of a laser pulse, these occupations are time dependent. The electronic charge density of the excited state, $\rho(r)$ is

$$\rho(r) = \sum_m n(\epsilon_m, t)\psi_m^*(r)\psi_m(r), \tag{2.35}$$

with $\psi_m(r)$ the Kohn-Sham orbitals.

The first term of equation 2.34 is an attractive contribution from the valence electrons, which is also present in tight-binding theory, and which is called band energy. The second, third and fourth terms are additional contributions from the valence electrons, which appear in density functional theory as a consequences of the fact that the Kohn-Sham orbitals are not physical single-electron wave functions, even though they are often interpreted as such. The fifth term refers to the ion-ion repulsive interaction, and the sixth term contains the electronic temperature and the electronic entropy , which is given by

$$S_e = -k_B \sum_m \big[n(\epsilon_m, t)\ \log(n(\epsilon_m, t)) + (1 - n(\epsilon_m, t))\ \log(1 - n(\epsilon_m, t))\big]. \tag{2.36}$$

Now, in view of the above discussion the laser-excited potential energy surface is just $U_0(\{\vec{R}_i\}, T_e(t)) = F_e(\{\vec{R}_i\}, T_e(t))$. This represents a generalization of the Born-Oppenheimer approximation. The resulting energy for a given T_e, represented as a function of all ionic coordinates, is called a laser-excited potential energy surface. The

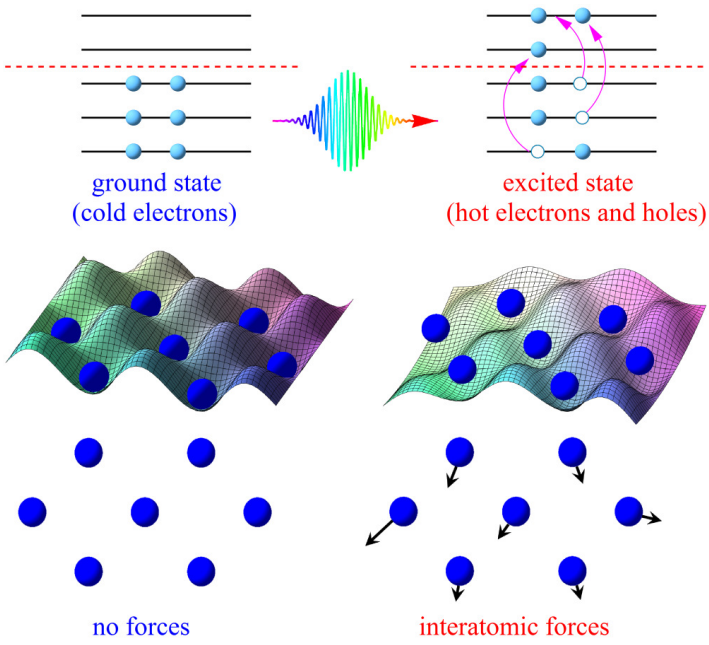

Figure 2.3: Illustration of the microscopic picture of laser-excited solids, adapted from figure 1 in [31].

usual Born-Oppenheimer approximation is recovered for $T_e = 0K$. Note that the functional dependence of $U_0(\{\vec{R}_i\}, t)$ on the atomic coordinates $\{R_i\}$ is strongly dominated by the electronic occupations $n(\epsilon_m, t)$ present in the first and sixth terms of equation 2.34 and also depends, albeit less strongly, on the self-consistent electronic charge density $\rho(r)$ present in the second, third and forth terms of equation 2.34. This implies that, if the electronic occupations undergo strong changes, then the potential energy landscape will change significantly.

A cartoon of the physical concepts involved in laser-induced structural changes is shown in figure 2.3. This figure also illustrate the role played by the laser-excited potential energy surface on structural changes in solids. Before the action of the laser pulse (see left side of figure 2.3) the solid is in thermodynamic equilibrium. At low temperature, electrons fill the states upto the Fermi level and the atoms are at the equilibrium positions of the ground state potential energy surface. The laser pulse changes (right side of figure 2.3) the electronic occupations by exciting a substantial fraction of electrons from bonding to anti-bonding states in a time that is short compared to the period of the fastest lattice vibration. This leads to a rapid changes in the potential energy landscape. As a consequence, the lattice may become unstable and forces appear on the atoms, driving a structural change.

In this thesis, I have modelled the systems irradiated by low-, medium- and high-laser intensities, and present results of ab-initio electronic-temperature dependent DFT calculations using all-electron full-potential linearized augmented plane wave

code WIEN2k and molecular dynamic simulations performed using our in-house code CHIVES for systems, which each show a distinctly different structural response to femtosecond-laser pulses at various fluences.

CHAPTER 3

Road of warm dense noble metals to the plasma state

3.1 Introduction

Warm Dense Matter (WDM) is a new state of matter, which constitutes a challenge to modern physics and whose investigation offers excellent means to understand strongly correlated multiparticle systems and their fast dynamics. The strong excitation of electrons in solids by an extreme ultraviolet (XUV) pulse results in a two-temperature WDM state [32–35], a regime that is of great interest in high-pressure science [36], the geophysics of large planets [37], astrophysics [38], plasma production, inertial confinement fusion [39], and condensed-matter physics [40, 41]. In the astrophysical context, WDM exists under stable and extreme density-temperature conditions, while in the laboratory, during the laser-matter interaction, WDM is generated as a transient (quasi-stationary for a short time) state between the condensed-matter and hot plasma regimes and its characterization involves ultrafast techniques and experimental facilities. While retaining the solid state density, it has two temperatures: The electronic temperature is of the order of tens of eV and the ions remain cold and keep their original crystallographic positions [42]. WDM is a partially degenerate state. Since WDM is encountered in high density systems, the kinetic energies of the electrons in the plasma is comparable to the Fermi energy. In addition, an XUV pulse may excite core-level electrons [43–46]. So, WDM is an intermediate state between condensed matter and the plasma, and the electrons effectively store the energy for times of the order of several picoseconds, where the exact time is governed by the electron-phonon coupling. Here we study the atomic pathways followed during the first few hundred femtoseconds in warm dense copper and silver and their role in the relaxation of WDM

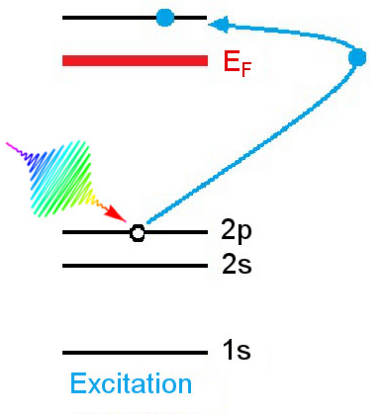

Figure 3.1: Illustration of core hole generation.

to equilibrium, *i.e.*, into the plasma state [1, 40, 47–49]. This is an interesting problem, because it is in general not known, whether this process occurs by nonthermal melting, where the atoms accelerate in the direction of a lattice instability [50], or thermally via the incoherent coupling of electrons and phonons, when the lattice has become sufficiently hot.

The study of WDM has drawn increasing attention during the last decade because of its importance in understanding the convergence between condensed matter and plasma physics. Recent experiments on thin gold films have suggested that electrical and optical properties of metals in the WDM regime can be measured by performing time-resolved measurements after the excitation of a metallic thin film by an XUV pulse [33]. A deeper understanding of the ultrafast dynamics of phonons is essential to study the above-mentioned relaxation of WDM to equilibrium, *i.e.*, into the plasma state. In this chapter we present microscopic calculations of the nonequilibrium phonon spectra in the warm dense noble metals copper and silver, and discuss the implications on their relaxation processes. Our observations are complementary to the previous theoretical [48] and experimental [1, 40] studies, and provide a more comprehensive view of the relevant structural dynamics of WDM. The main goal of this work is to demonstrate that it is possible to study the information on femtosecond nonequilibrium phonon dynamics of WDM.

3.2 Creation of warm dense matter by core-hole excitation

Insight into the dynamical properties of WDM can be obtained by studying the XUV-pulse-induced potential energy surface of the solid. As mentioned above, under strong

XUV excitation, the electronic temperature T_e of solid dense copper and silver increases to the order of 10,000 K (corresponding to the laser energy deposited) while the lattice temperature T_l remains roughly unchanged. In addition, core holes may be generated. We assumed that the interaction of an XUV pulse with copper and silver generates one core hole per primitive unit cell by the excitation of core-level electrons [48]. At room temperature and under ambient pressure, copper (silver) has a filled shell ionic core [Mg] $3p^6$ ([Zn] $4p^6$). We simulated the excitation of core holes by removing one core electron from a $3p_{3/2}$ orbital for copper and one electron from a $4p_{3/2}$ orbital for silver, respectively, and adding it to the conduction band in order to maintain charge neutrality (see figure 3.1). The schematic illustration of core hole generation from $2p$ core state is sketched in figure 3.1. Core holes are very unstable and short lived, and are expected to decay via Auger processes on a femtosecond-time scale. However, they are excited again and again by the XUV pulse, making their influence non-negligible during the pulse duration. For an ultrashort XUV pulse we expect copper and silver atoms with one core hole to be close to their original lattice positions. So, at the instant an XUV pulse interacts with copper or silver, the system is in an exotic, highly ionized, yet crystalline state, of which the phonon spectrum is unknown.

3.3 Theoretical modelling of the warm dense state

Theoretically and computationally, recent advances in finite-temperature ab initio electronic structure methods enable to study the phonon dynamics of WDM. Taking into account the above mentioned facts on core hole generation (Section 3.2), we explored the dynamic evolution of the potential energy surface of WDM using accurate *first principle* density functional theory (DFT) calculations. As the excited electrons and the other electrons in the system feel the potential produced by the core hole, we used the all-electron full-potential linearized augmented plane wave ab initio program WIEN2k [51], which explicitly includes the core electrons, in order to compute self-consistently screening effects and other changes in the total energy and atomic force constants (AFC) of the system.

In order to obtain the AFC one must assume that interactions between the atoms beyond a certain range are negligible. In our systems we neglected the forces beyond the sixth nearest neighbor distance and an additional assumption, that fifth-neighbour constants are negligible, was made since the sublattice containing the atom at $(\frac{1}{2}\frac{1}{2}0)$ contains two other atoms of the type $(\frac{3}{2}\frac{1}{2}0)$ within the stipulated range. The force constants were calculated by displacing an arbitrary (ith) atom from its equilibrium position ($\mathbf{R}_i$) along the $\alpha = z$-direction by $u_i^\alpha = 0.122$ and 0.139 a_0 (a_0 = Bohr radius) in copper and silver, respectively. Then the AFC on the jth ($\mathbf{R}_j$) atom $A_{ij\alpha\beta}$ can be

obtained by,

$$A_{ij\alpha\beta} = -\frac{\partial F_j^\beta}{\partial u_i^\alpha}, \tag{3.1}$$

where F_j^β is the force on the jth atom produced due to the displacement u_i^α of the ith atom. The dynamical matrix of face-centered cubic (fcc) copper and silver over the first Brillouin zone (BZ), $D_{\alpha\beta}(\mathbf{q})$ was computed from the AFC within a supercell of fixed volume containing 32 atoms using,

$$D_{\alpha\beta}(\mathbf{q}) = \sum_j A_{ij\alpha\beta}\ \exp(-i\mathbf{q}\,.\,(\mathbf{R}_i - \mathbf{R}_j)), \tag{3.2}$$

where $\mathbf{q}$ is the phonon wave vector. Diagonalization of $D_{\alpha\beta}(\mathbf{q})/M$, where M is the atomic mass of copper or silver, gave us phonon frequencies $\omega_i^2(\mathbf{q})$, i=1,. . .,3.

To study the effect of T_e on the potential energy surface of WDM, the evolution of the phonon spectrum as a function of T_e was analyzed. We note that the electronic occupation numbers immediately following XUV excitation may be different from the Fermi distribution assumed in our present work. Even though electron-electron interactions quickly thermalize the electrons, the initial nonthermal occupancies may have a transient effect on the lattice properties that would be interesting to investigate but is outside the scope of the present study. We performed our calculations with muffin-tin radii of 2.11 a_0 and 2.58 a_0 on the basis of the criterium that no more than 0.01 core electrons should "leak out" of their muffin-tin spheres, and $RK_{max} = 8$ and 7 to fix the size of the basis sets for copper and silver, using a sufficiently fine $\mathbf{k}$ grid of 14x14x14. We calculated the effects of various laser fluences by changing T_e within the framework of electronic-temperature-dependent DFT [52]. In addition, we analyzed the nonequilibrium state existing in the presence of one core hole per atom as well as hot electrons for the noble metals copper and silver.

3.4 Results

In order to study the structural dynamics of warm dense noble metals, we computed both electronic and phonon band structures, densities of states, etc. The discussion about the properties are the following:

3.4.1 Atomic force constants (AFC)

The theory of the lattice dynamics of crystals can be discussed in terms of AFC, the force constants between different atoms in the lattice. The model is exact, in the sense

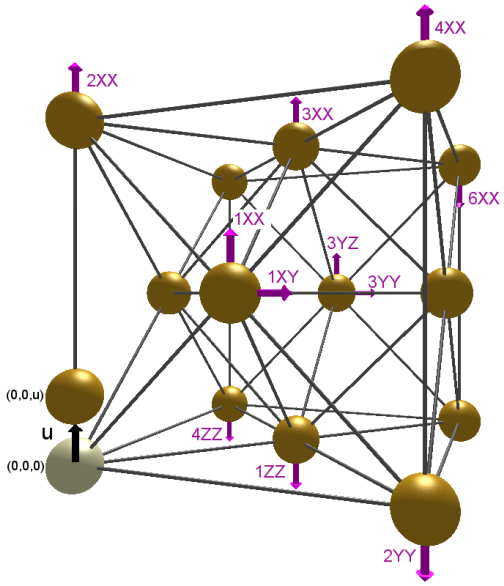

Figure 3.2: Face centered cubic structure of a Cu crystal. The purple arrows indicate the directions of atomic forces upto sixth nearest neighbors when the reference atom at (0,0,0) is moved along the z direction to (0,0,u) by a small displacement u. The labels indicate atomic force constants and are the same as in Table 3.I (room temperature).

that from a given complete and unique set of force constants, complete knowledge of the eigenvalues and eigenvectors of the phonon spectrum can be derived. However, atomic force constants are the best way of representing all the interactions in the crystal lattice that give rise to its dynamics, particularly in metals.

We studied the phonon dynamics of noble metals in warm dense regime using the AFC in the presence of core holes. Our computed AFC for copper and silver with and without a core hole at two different T_e are presented in Table 3.I. There are in total eleven inequivalent AFC acting in our supercells [53], whose directions we show in figure 3.2. Other than the fifth-neighbour constants, which are incorporated into the first neighbour values, the $3XZ$, $4XY$ and $6YZ$ force constants do not appear in the results because of cancellation as a consequence of symmetry about the reference atom. Comparison of AFC in mHa/a_0^2 determined by interplanar force constant decomposition (Svensson *et al* [54]) and by decoupling transformation (Vanderwal [53]) with our computed AFC at room temperature (Table 3.I) indicates that they are in very good agreement. The AFC label $n\alpha\beta$ in Table 3.I refers to the displacement of the reference atom in the direction α and the resulting force on the nth nearest-neighbor atom in the direction β.

We further observed that all force constants upto sixth nearest neighbors are changed in the core hole state, especially the forces on the first nearest neighbors

Elements	AFC	Svensson *et al* (1967) results	Vanderwal (1977) results	DFT results		
				Room temperature	Cold core hole	Hot core hole (30,000 K)
Cu	1ZZ	-0.91	-0.74	-0.62	-2.80	-4.63
	1XY	9.52	9.57	8.71	17.15	19.56
	1XX	8.42	8.35	7.75	13.48	15.18
	2XX	0.23	0.29	0.72	3.72	3.59
	2YY	-0.15	-0.07	-0.27	-0.74	-0.34
	3XX	0.41	0.36	0.41	0.22	0.07
	3YY	0.20	0.15	0.09	0.56	0.03
	3YZ	0.12	0.17	0.15	0.05	-0.02
	4XX	0.08	0.02	0.01	-0.55	0.04
	4ZZ	-0.19	-0.15	-0.02	-0.01	-0.01
	6XX	0.09	-0.04	-0.01	0.31	-0.01
Ag	1ZZ			-0.99	-3.16	-3.98
	1XY			6.95	14.55	16.37
	1XX			6.15	11.48	12.65
	2XX			0.63	2.85	2.19
	2YY			-0.24	-0.58	-0.28
	3XX			0.38	0.12	0.18
	3YY			0.09	0.35	0.08
	3YZ			0.13	-0.03	0.00
	4XX			0.12	-0.38	0.04
	4ZZ			-0.02	-0.02	-0.01
	6XX			-0.02	0.18	-0.01

Table 3.I: Comparison of atomic force constants (AFC) in mHa/a_0^2.

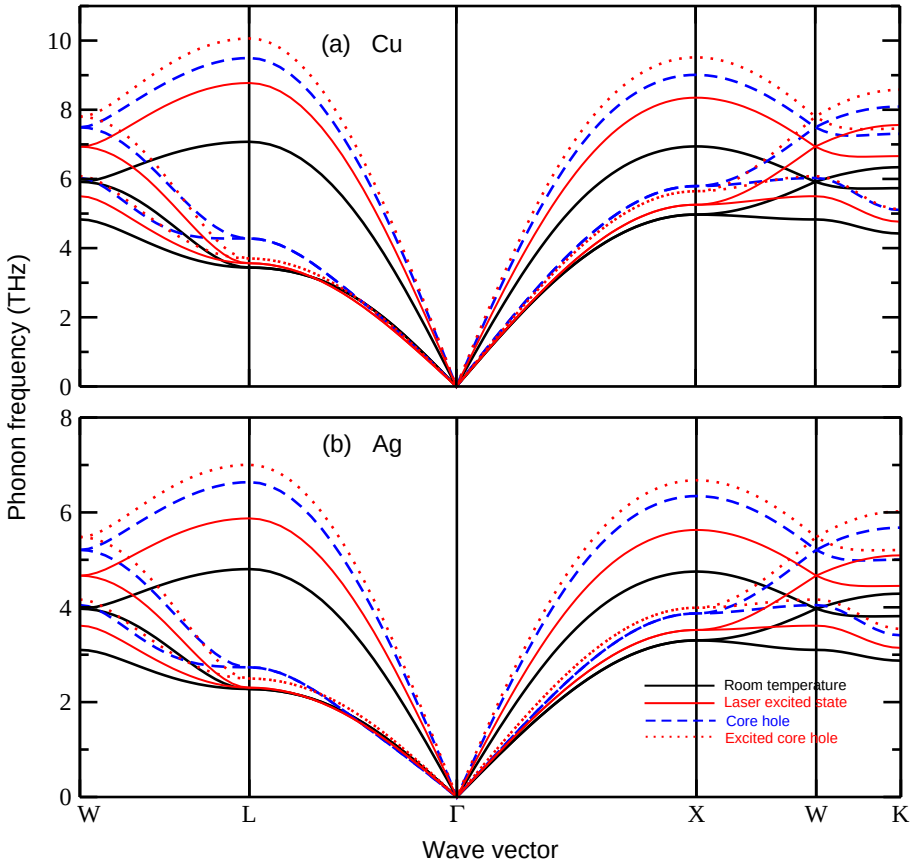

Figure 3.3: Phonon dispersion spectrum of (a) copper and (b) silver. Black solid curves show our results for room temperature, red solid curves at $T_e = 30{,}000$ K without core hole. Blue dashed curves represent the state with one core hole per atom and red dotted curves are for the core-hole state with hot electrons at $T_e = 30{,}000$ K.

($1ZZ$, $1XY$ and $1XX$) are affected most by the presence of a core hole and are playing an important role in the phonon dynamics of noble metals. Apparently, the drastic increase with T_e in the AFC of the first neighbors are responsible for the phonon hardening in warm dense copper and silver. From our T_e-dependent calculations we found that: The higher the excitation fluence, the greater the potential energy gradient and the more intense the AFC, and thus results in the hardening of the potential energy surface.

3.4.2 Phonon dispersion spectrum and bond hardening

In order to analyze the electronic-temperature-dependent potential energy surface, we determined the phonon dispersion spectra of our systems with one core hole per atom at various T_e upto 30,000 K. In figure 3.3 we see that the presence of core holes affects

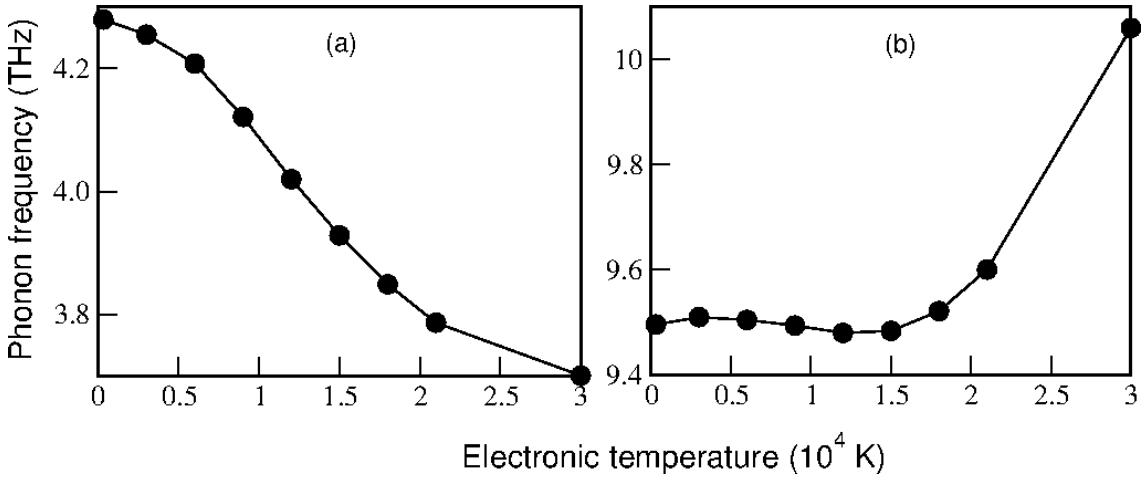

Figure 3.4: Transverse (a) and longitudinal (b) acoustic phonon mode frequencies of copper at the L-point in the BZ with one core hole per atom as a function of the electronic temperature.

the materials in the same way as the presence of hot electrons alone [48], *i.e.*, the AFC of both copper and silver increase and all phonon modes harden. In the presence of a core hole, however, the T_e affects the bonds differently: Most of the phonon modes are hardening and few of them are softening. In both copper and silver, all longitudinal modes are showing hardening in the core-hole-excited state when T_e is raised from room temperature to 30,000 K (figure 3.3), but the transverse modes near the L- and X-points in the BZ of copper and near the L-point in the BZ of silver are showing bond softening compared to the spectrum with a core hole. In more detail, figure 3.4 shows the temperature-dependent transverse and longitudinal acoustic phonon frequencies of copper at the L-point in the first BZ with one core hole per atom. The transverse acoustic (figure 3.4a) mode shows an increasing degree of softening with increasing T_e while the longitudinal acoustic (figure 3.4b) mode shows hardening upto 3000 K, then undergoes a weak softening until 12,000 K and a sharp hardening afterwards. Averaged over all modes in the first BZ the potential energy surface of both copper and silver harden in the warm dense regime as a function of T_e.

3.4.3 Electronic band structure

In solid-state physics, the electronic band structure of a solid describes the ranges of band energy, that an electron within the solid may have. It successfully uses a material's band structure to explain many physical properties of solids, such as electrical resistivity, optical absorption, etc. We have studied the electronic band structure of copper and silver at room temperature without and with core holes [48]. We found that

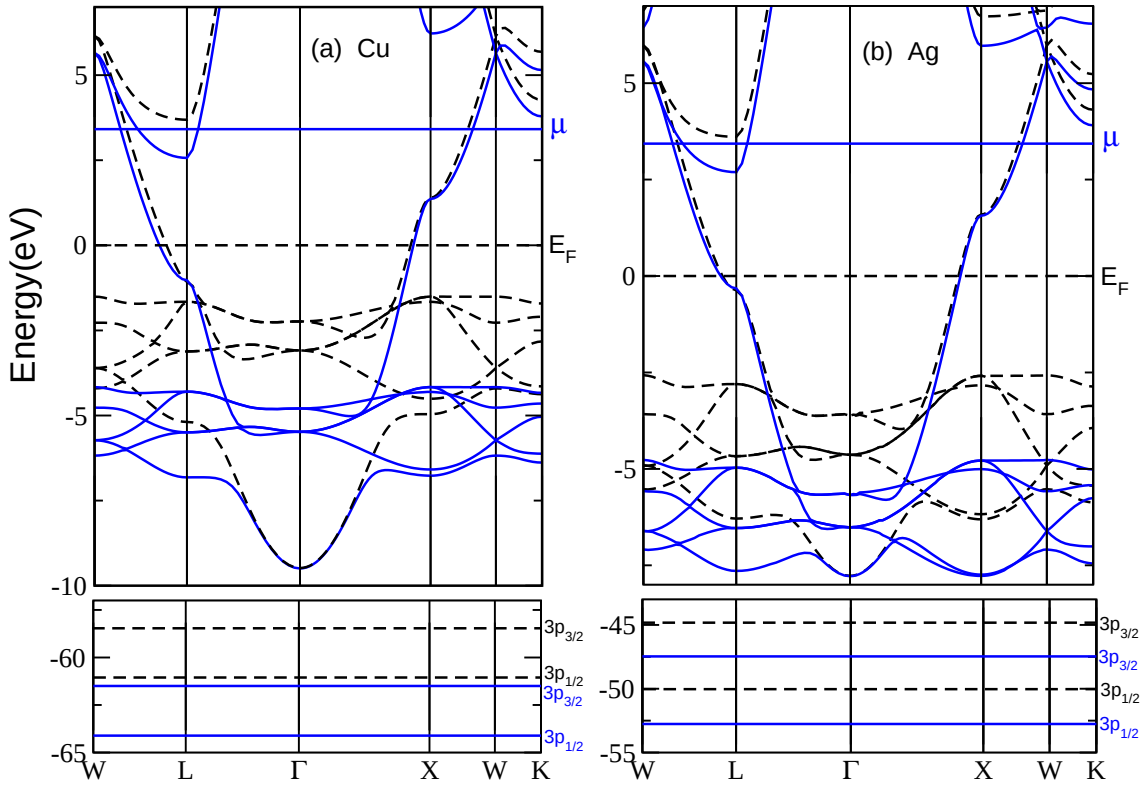

Figure 3.5: Electronic band structure of (a) copper and (b) silver in the electronic ground state (black dashed) and in the presence of one core hole per atom (blue solid).

the electronic band structures of copper and silver are strongly affected by the core hole. In figure 3.5 we plotted the influence of the presence of core holes on the electronic band structure of copper and silver with respect to the ground state. The ionic coordinates are assumed to be in the initial crystal structure. The observed changes due to the excitation are relative to the position of the bottom of the s bands, which we keep fixed. In the presence of an extra positive charge, appreciable changes can be mainly observed in the position of the core levels, which undergo a strong red shift of several eV, which is almost independent of the wave vector $\mathbf{q}$. The core levels of copper ($3p$ states) are showing significant red shift than that of silver ($4p$ states). Moreover, the s conduction band as well as the d bands are also strongly affected by the core holes. The chemical potentials (E_F) are shifted upward in the presence of core hole (μ).

3.4.4 Electronic and phonon densities of states

The strengthening of bonds in the warm dense regime of noble metals can be explained from the AFC and densities of states. In figure 3.6 we plotted our computed electronic

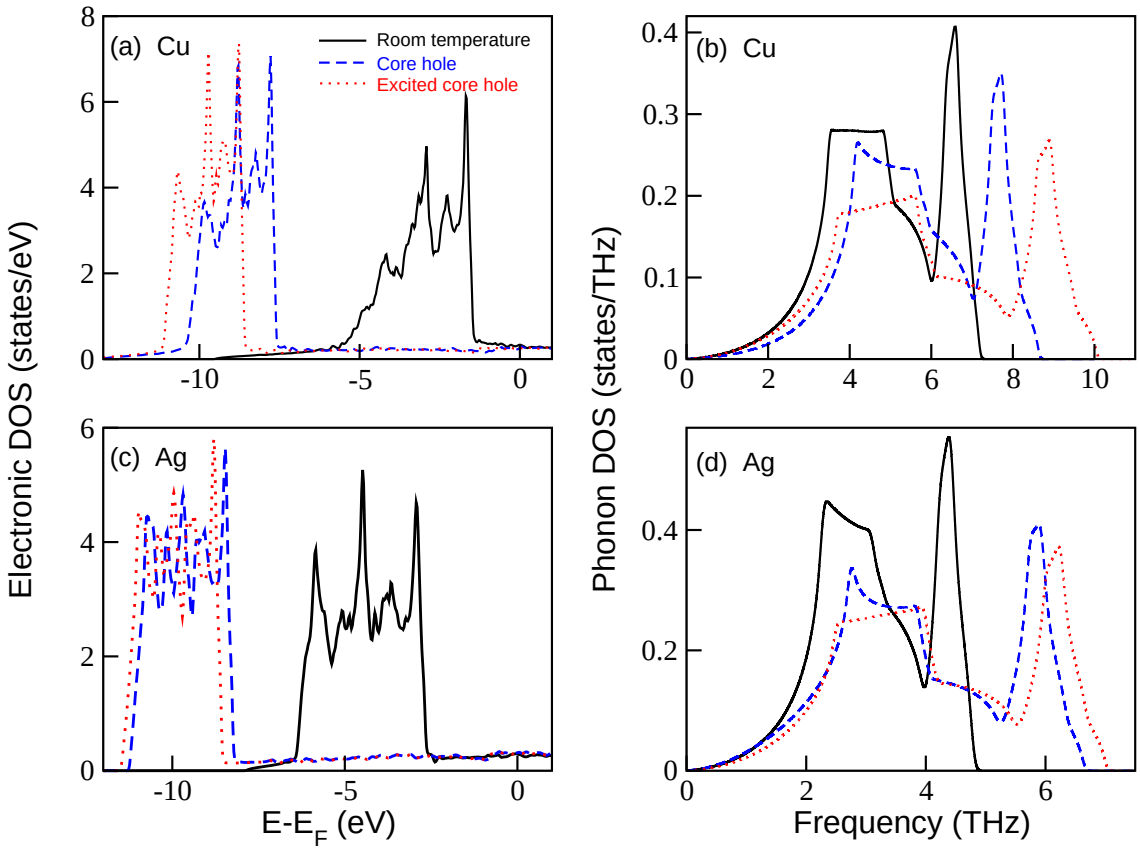

Figure 3.6: Electronic and phonon densities of states of copper (a and b) and silver (c and d) at room temperature (black solid), in the presence of cold (blue dashed) and hot, T_e = 30,000 K (red dotted) electrons with one core hole per atom.

and phonon DOS of copper and silver, both at room temperature and with cold and hot core-hole states. The comparison reveals that the DOSs change considerably. In the case of the electronic DOS (figure 3.6a and c), each of which we plotted with reference to its own Fermi level, the presence of a core hole shifts the d bands towards lower energies, while its width becomes significantly smaller, implicating that the $3d$ states of copper and silver become more localized, when a core hole is excited [46]. The Fermi levels move towards higher energy regions.

The noble metals show dramatic changes in the phonon DOS upon core hole and its excited states. A blue shift appears in both longitudinal and transverse acoustic modes (figure 3.6b and d) of copper and silver in the presence of core hole, however there also appear a redistribution of weight resulting in a reduction of phonon DOS, which means the phonon modes become less degenerate in the presence of cold and hot core hole.

3.5 Road of warm dense noble metals to the plasma state

In many materials, when electrons are excited, the average bonding force is weakened and the solid cannot maintain its crystal structure [10, 55]. In contrast, Mazevet *et al.* [56] simulated a superheated state of ordered, electronically stabilized warm dense gold and also found that its melting temperature increases in the laser-excited state [57]. From our work we realized that the average AFC of copper and silver become stronger both in the cold and hot core-hole-excited state compared to the ground state. figure 3.3 shows that the lattice remains stable even at $T_e = 30{,}000$ K. In general, the variation of the effective interatomic potential should change the mechanical stability of the lattice, but in the case of noble metals we found no indication of any phonon mode instability both in the presence of core holes alone, and with core holes and hot electrons. So, it is clear that nonthermal melting cannot be the pathway for the relaxation of warm dense copper and silver. Instead, the laser-excited hardening of the phonon modes in warm dense noble metals leads to conclude that these systems relax thermally into a plasma state.

For the description of the plasma properties of WDM, the presence of an ordered crystal lattice should be taken into account. We can expect that the crystal structure will have an influence on the plasma properties that are related to the highly excited lattice vibrations. In the case of WDM with a highly ordered crystal, the relaxation is a faster process than in the gaseous plasma [58]. The experiments performed on warm dense silicon [59] and aluminum [60] samples suggest a very low electron-phonon coupling time. The electronic excitation of silicon weakens the covalent bonding, softens the lattice, and results in an electronically driven disordered lattice [57]. Such a laser-induced instability induces ultrafast nonthermal melting in silicon [50]. In the case of nearly free-electron metals like aluminum, the lattice stability appears to be mostly unaffected by the electronic excitation [57] and such solids shows thermal melting on the picosecond time scale after the excitation [61]. In contrast, it is observed that in warm dense copper, which was created without a core hole in Ref. [1], the energy exchange rate between electrons and lattice vibrations is temperature dependent and is about 3 to 6 times faster [1] than the theoretically computed electron-phonon coupling constant [2]. In analogy to the above-mentioned finding, that the electron-lattice relaxation is more efficient in the solid than in the plasma phase [58], we suggest that the excess stability of the lattice attained in copper and silver at higher T_e due to an XUV or laser excitation may be responsible for the fast energy exchange rate (electron-phonon coupling constant) in warm dense noble metals.

We have theoretically studied a very transient, exotic state of highly ionized crystalline noble metals copper and silver. We observed how the electronic and phonon

DOS as well as the electronic band structure and phonon dispersion spectra are changed in core-hole states, both with cold and hot electrons. We found that the change in the AFC of the first nearest neighbors due to the presence of core holes and hot electrons cause the hardening of the potential energy surface. Redistribution of the electron densities of states in the presence of core hole and after the increase of T_e cause the system to gain extra stability. Our observations demonstrate that the relaxation of WDM and the equilibrium state reached after the relaxation depends on the structural dynamics. This work is a first step towards a more complete theoretical understanding of ultrafast structural dynamics of warm dense noble metals. The method presented here is applicable to study the potential landscape and temperature relaxation in highly nonequilibrium solids and WDM systems.

CHAPTER 4

Transient phonon vacuum squeezing due to femtosecond-laser-induced bond hardening in noble metals

4.1 Introduction

Vacuum squeezing is a fundamental quantum mechanical effect involving a state in which the uncertainty in one of two conjugate variables drops below that of the vacuum state. It is mathematically characterized by a nonpositive Glauber-Sudarshan P distribution [62] and has no classical analogue. At absolute zero the atoms in a crystal undergo quantum oscillations about their equilibrium positions, in which the motions obey Heisenberg uncertainty principle. These oscillations are equivalent to vacuum fluctuations which is the fundamental limit of any measurements.

Photons have been squeezed strongly with squeezing factors close to 1 [64] towards applications in the fields of quantum communication [65] and gravitational wave detection [66,67]. A variety of squeezed states were proposed for other bosons, in particular, those associated with atomic vibrations in quantum dots [68,69], quantum wells [70,71], molecules [72,73], and polaritons [74,75]. In crystals, the excitation and measurement of squeezed phonons can be of great importance for fundamental explorations and for studying the ultrafast dynamics of excited states on atomic length scales [76,77], but it is hard to achieve.

Seventeen years ago it has been shown that in transparent solids, femtosecond-laser excitation can lead via second-order Raman scattering to a squeezed phonon state [3,4,78]. However, this excitation mechanism is very weak, which explains why

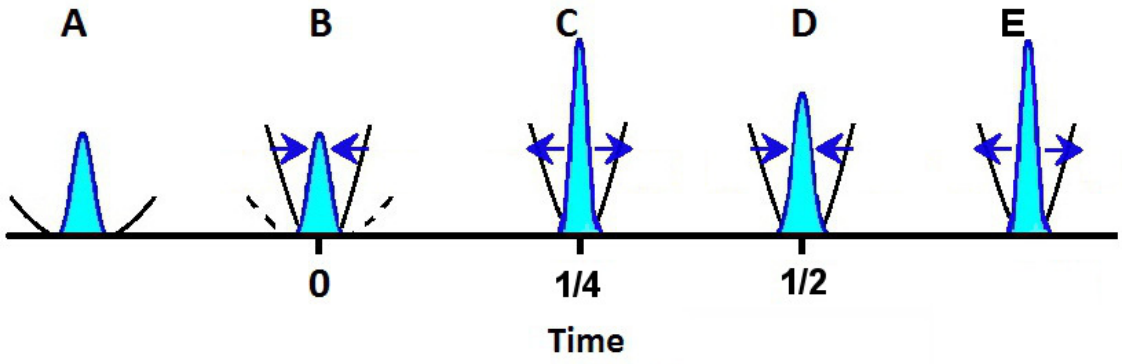

Figure 4.1: Illustration of real-space squeezing. Black curves represent potential energy surfaces and blue shaded are phonon wave packets.

the maximum reported squeezing factor is only of the order of 10^{-6} [4, 78]. Recently, squeezed states have also been observed in an opaque semimetal, where, however, as a consequence of laser-induced bond softening the variance of the atomic displacements (the expectation value of the square of the displacement minus the square of the expectation value of the displacement — mean-square displacement) increases and consequently does not drop below that of the vacuum state [5]. In the present study, we theoretically explore the possibility of generating vacuum squeezed longitudinal phonons at different points in the Brillouin Zone (BZ) of copper and silver (point group O_h), which is shown in the inset of figure 4.2, in contrast to semimetals, bond hardening after ultrashort laser excitation [48]. After presenting the quantum mechanical origin of the femtosecond-laser-induced increase of phonon frequencies, we demonstrate under which excitation conditions a sizeable vacuum squeezing effect results and we point out how this phenomenon could provide the first direct experimental evidence of femtosecond-laser-induced bond hardening in metals.

4.2 Physical picture of vacuum phonon squeezing

In general, the interaction of a femtosecond-laser pulse with a solid produces hot electrons and holes, which lead to changes in the interatomic potential. Consequently the vibrational spectrum changes, giving rise to many interesting ultrafast structural phenomena [79, 80]. In metals, an intense laser pulse typically excites the electrons to temperatures of the order of 10,000 K, which thermalize with the lattice within a few picoseconds by electron-phonon collisions.

Microscopically, vacuum phonon squeezing means a breathing of the width of the phonon wave packet. In bond-softening materials, for example, semiconductors and semimetals [6,81] the laser-induced potential is shallower than in the electronic ground state. So, the phonon wave function, whose width is at sufficiently low ionic temperature initially equal to the zero-point motion $\langle Q_{0K}^2(0)\rangle$ and which is afterwards characterized by the expectation value $\langle Q^2(t)\rangle$, where Q is the phonon normal coordinate, is immediately following the femtosecond-laser pulse too narrow for the laser-modified potential. Therefore, it starts to broaden in an oscillatory fashion as follows from the time-dependent Schrödinger equation. After a quarter of a phonon period, the wave packet expanse in real space, the mean-square width, reaches a maximum and after half a phonon period, the wave packet reaches its minimum width, which, however, is not narrower than the initial state. Therefore the squeezing factor

$$S = 1 - \sqrt{\frac{\langle Q^2(t)\rangle}{\langle Q_{0K}^2(0)\rangle}} \tag{4.1}$$

with respect to the 0 K mean-square width before laser excitation $\langle Q_{0K}^2(0)\rangle$ cannot become positive in this case, which is the hallmark of vacuum phonon squeezing in real space. We note that the variance of the conjugate variable of Q, the phonon momentum P, which behaves oppositely, might squeeze below its 0 K width following femtosecond-laser-induced bond softening. In contrast, noble metals show laser-induced bond hardening, which is equivalent to a laser-modified potential that is narrower than the ground-state potential. In this case we found that the wave packet may initially squeeze in real space with S $>$ 0, depending on the degree of phonon hardening and the incoherent rate of energy transfer from the hot electrons to the lattice, which are both functions of the excitation fluence. If the phonon is not squeezed the variance should be a constant.

A cartoon of the physical concepts discussed before about the vacuum phonon squeezing in the case of laser-induced bond hardening materials is shown in figure 4.1. (A) Initially, the probability distribution corresponds to the ground state. (B) At a time t =0 the frequency of the oscillation suddenly changes to a higher value due to change in potential energy surface. (C) Now the wavefunction is no longer an eigenstate of the initial state, and the width of the probability distribution in real-space is "squeezed" to a smaller value than the width of the ground state probability distribution for the new, hardened potential. (D-F) The wavefunction evolves in time, resulting in an oscillation in the width of the probability distribution, depending on anharmonicities and phonon-phonon coupling.

4.3 Origin of bond hardening in noble metals

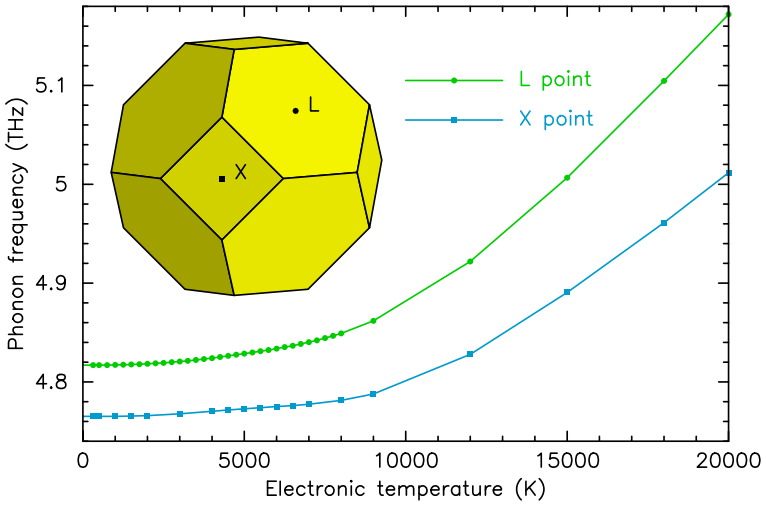

Figure 4.2: Ab initio computed longitudinal L- and X-point phonon frequencies in femtosecond-laser excited silver as a function of the laser-induced electronic temperature. The inset shows the first Brillouin zone of silver.

Recent theoretical [27, 57] and experimental [40] studies on noble metals predict a hardening of phonon modes after electronic excitation on extremely short timescales, shorter than the equilibration between the excited electrons and the lattice, which lasts picoseconds [82], in contrast to most of the materials, in which electronic excitation either softens or does not substantially effect the interatomic potential. figure 4.2 illustrates this for the longitudinal L- and X-point phonons in silver. Since the lattice vibrational frequencies have changed after excitation, the system no longer evolves in the ground-state potential and a perturbing potential arises from the atomic displacements. In particular, the atomic motions along longitudinal phonon directions cause the electronic distributions from neighboring atoms to increase their overlaps. As a result the bands broaden and the electronic density of states (DOS) changes. In order to quantify these changes we computed the DOS of silver in the ground state with and without atomic displacements along a longitudinal phonon direction. In both cases a high DOS peak between -6.5 and -2.5 eV below the Fermi level arising from the dispersion of the $4d$ electrons is superimposed on a lower and broader distribution starting at -8 eV belonging to the half-filled $5s$ band. We studied the difference in DOS in the central region of the s band (figure 4.3). The negative difference in DOS indicates that electrons in the $5s$ band are distributed over a wider energy range, away from the Fermi energy, when the atoms are displaced. Before laser excitation the phonon potential energy is a parabola, whose second derivative is proportional to the square of the phonon frequency. After femtosecond-laser excitation, the atoms move on a

laser-excited potential energy surface, viz, Mermin's free energy of the electrons at a constant high electronic temperature T_e. The relationship between the ground-state potential energy surface and the laser-excited phonon potential can be approximately described by a Sommerfeld expansion [84],

$$U(T_e) \approx U(0) - \frac{\pi^2}{6}(k_B T_e)^2 \,\mathrm{DOS}(E_F), \tag{4.2}$$

where k_B is Boltzmann's constant and $\mathrm{DOS}(E_F)$ is the electronic DOS at the Fermi energy. Because of the smaller electronic DOS at finite displacement, Mermin's free energy decreases less with increasing displacement after laser excitation leading to a steepening of the potential energy versus displacement, which is the origin of bond hardening in noble metals. It illustrates the strong correlation between electronic structure and lattice bonding. At electronic temperatures $T_e \sim 2000{-}8000$ K, at which our studies are concentrated, we found that the excitation of $5s$ electrons dominates the phonon hardening. This is in agreement with the finding of Ref. [2] that at these electronic temperatures, the electronic structures of noble metals resemble the free electron gas model, where only the s-band electrons overlap. At higher T_e, of the order of $\sim$ 10,000 K or more, a significant amount of d-band electrons is additionally excited, which — we found — contributes also to the bond hardening at very high fluences.

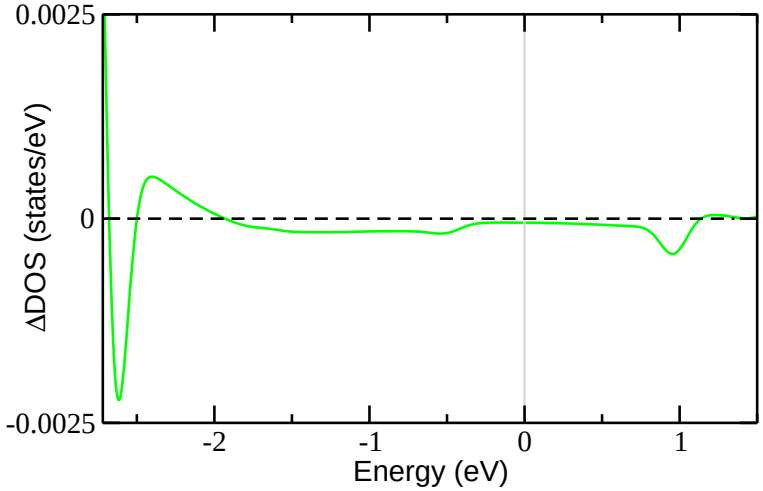

Figure 4.3: The difference in electronic ground-state DOS of silver around the centre of the half-filled $5s$ band, between without (black dashed) and with (green solid) atomic displacements in the direction of the L-point longitudinal phonon mode. Grey vertical line indicate the Fermi energy.

If the change of phonon frequency after femtosecond-laser excitation occurs on a time scale much faster than the period of lattice vibrational modes, dynamics of the variance of the atomic positions from their average values can result.

4.4 Time-dependent variance

For studying the possibility of vacuum phonon squeezing in laser-excited noble metals, it is necessary to calculate the time-dependent variance of the atomic displacements for coherent lattice oscillations and incoherent electron-phonon coupling.

4.4.1 Coherent atomic displacements

Time-dependent variance of the coherent laser-induced atomic displacements in the direction of particular phonon modes with wavevector $\mathbf{q}$ and branch index λ quantum mechanically using [5]:

$$\langle Q^2(t)\rangle_{coh} = \frac{\hbar M}{2}\sum_{\lambda'}\omega^i_{\mathbf{q}\lambda'}\left|\boldsymbol{\varepsilon}^*_{\mathbf{q}\lambda}\cdot\boldsymbol{\varepsilon}^i_{\mathbf{q}\lambda'}\right|^2\left[\left(\frac{\cos\omega_{\mathbf{q}\lambda}t}{\omega^i_{\mathbf{q}\lambda'}}\right)^2+\left(\frac{\sin\omega_{\mathbf{q}\lambda}t}{\omega_{\mathbf{q}\lambda}}\right)^2\right], \tag{4.3}$$

where $\hbar$ is Planck's constant, M is the atomic mass of copper or silver, and $\omega^i_{\mathbf{q}\lambda}$ ($\omega_{\mathbf{q}\lambda}$) and $\boldsymbol{\varepsilon}^i_{\mathbf{q}\lambda}$ ($\boldsymbol{\varepsilon}_{\mathbf{q}\lambda}$) are phonon frequencies and eigenvectors in the ground (laser-excited) state, which we calculated using state-of-the-art all-electron DFT methods.

The interatomic force constants of ground and excited states are computed by performing electronic-temperature dependent DFT [85] calculations using the all-electron full-potential linearized augmented plane wave code WIEN2k [51]. The calculations are done within a supercell of 32 atoms [53] by displacing an arbitrary atom from its equilibrium position along the z-direction by 0.122 and 0.139 a_0 (a_0 = Bohr radius) in copper and silver, respectively. We chose the muffin-tin radii of 2.11 a_0 and 2.58 a_0, and $RK_{max} = 8$ and 7 to fix the size of the basis sets for copper and silver with a 14x14x14 $\mathbf{k}$ grid. The phonon eigenvalues and eigenvectors are obtained from the resulting dynamical matrix. For more converged results we have calculated the phonon frequencies upto 5 million $\mathbf{k}$-points by using a computationally less time consuming non-self-consistent method [7, 84].

4.4.2 Incoherent electron-phonon coupling

In addition to the coherent oscillations of equation 4.3 there is an incoherent heat transfer from the hot electrons to the lattice, which we included by simulating the evolution of the lattice and electronic temperatures, T_l and T_e, in laser-excited copper and silver using the coupled equations of the two temperature model (TTM) [2, 86],

$$C_e\frac{\partial T_e}{\partial t} = -G(T_e - T_l), \tag{4.4}$$

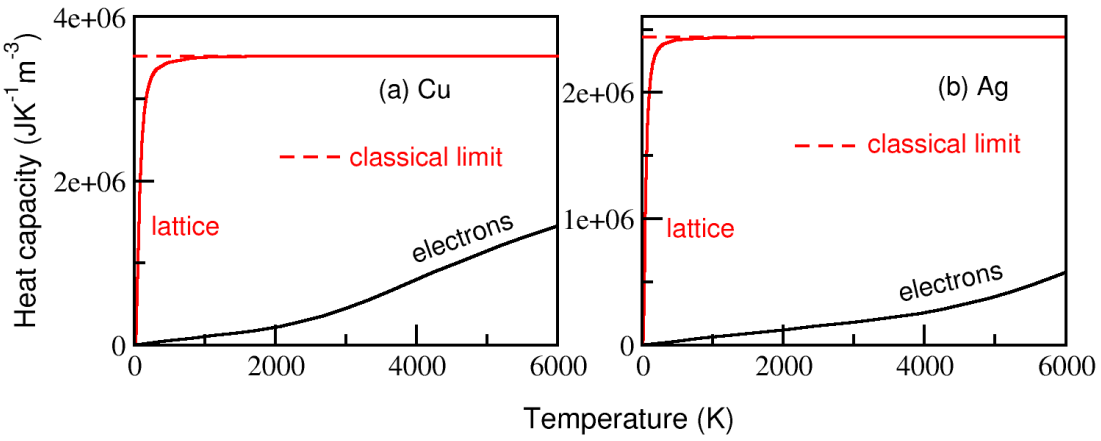

Figure 4.4: (a) Electron and lattice heat capacities of (a) copper and (b) silver as a function of their respective temperatures.

$$C_l \frac{\partial T_l}{\partial t} = G(T_e - T_l), \tag{4.5}$$

where $C_l(T_l)$ and $C_e(T_e)$ are respectively the lattice and electronic heat capacities and $G(T_e)$ is the electron-phonon coupling factor. Note that C_e and G depend on the electronic temperature and that equations 4.4 and 4.5 consider only the temporal dependencies $T_l(t)$ and $T_e(t)$ and do not include their depth dependence, describing noble metals in a thin film geometry [40].

TTM model accounts for the laser excitation of the conduction band electrons and subsequent energy relaxation process. To solve the equations of the TTM, we computed the heat capacities of electrons and phonons from our DFT results. The electronic heat capacity $C_e(T_e)$ calculated from the band energy E_{band} using:

$$C_e(T_e) = \frac{\partial E_{band}}{\partial T_e}, \tag{4.6}$$

in which E_{band} is calculated by $E_{band} = \sum_m n(\epsilon_m) \cdot \epsilon_m$, where $n(\epsilon_m)$ is the occupation number of the electronic Kohn-Sham level ϵ_m. The lattice heat capacity $C_l(T_l)$ is given by

$$C_l(T_l) = \frac{\partial E}{\partial T_l}. \tag{4.7}$$

The total energy of phonons E at temperature T_l in a crystal can be written as the sum of the energies over all phonon modes, $E = \sum_{\mathbf{q}p} \langle n_{\mathbf{q}p} \rangle \hbar\omega_p(\mathbf{q})$, where $\langle n_{\mathbf{q}p} \rangle$ is the occupancy of phonons of wave vector $\mathbf{q}$ and mode p (p=1,..., $3N$) with N number of atoms in a unit cell. figure 4.4 shows the temperature-dependent heat capacities of copper and silver. According to Dulong-Petit theory, when the temperature is above the

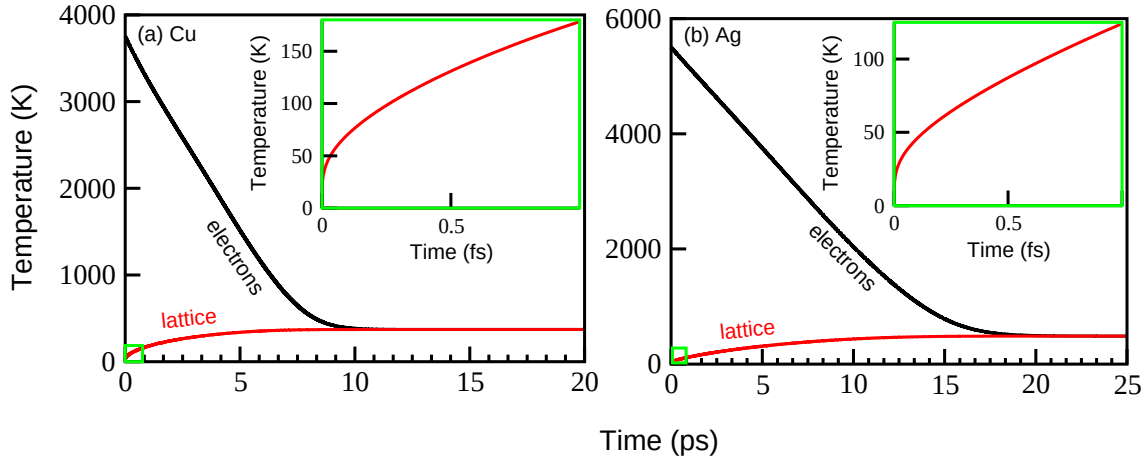

Figure 4.5: Evolution of electron and lattice temperatures after a laser excitation heating the electrons to 3750 (5500) K for (a) copper ((b) silver). The insets show the indicated regions enlarged.

Debye temperature ($T_D = 343.5$ K for copper and 215 K for silver), the heat capacity is very close to the classical value $3Nk_B$. For temperatures below T_D, quantum effects become important and $C_l(T_l)$ decreases to zero. From figure 4.4 one can see that the lattice heat capacities approaches to classical limit when the temperature is raised above T_D. The electron-phonon coupling data to solve the TTM used from Lin *et al.* [2, 87].

From the time-dependent lattice temperature we estimated the increase of the variance of phonons with quantum numbers $\{\mathbf{q}, \lambda\}$ due to incoherent lattice heating in the harmonic approximation to be

$$\Delta\langle Q^2(t)\rangle_{incoh} = \frac{\hbar}{2M\omega_{\mathbf{q}\lambda}}\left[\coth\left(\frac{\hbar\,\omega_{\mathbf{q}\lambda}}{2k_B T_l(t)}\right) - 1\right]. \tag{4.8}$$

We found that the lattice heats rather rapidly. For example, in copper (silver) a particular laser excitation heating the electrons to 3750 (5500) K, heats the lattice to 178 (124) K with an average heating rate of 0.18 (0.12) K/fs during the first 1 ps. See insets of figure 4.5(a) and (b)

4.4.3 Total variance

The total variance of squeezing and lattice heating is given by

$$\langle Q^2(t)\rangle_{tot} = \langle Q^2(t)\rangle_{coh} + \Delta\langle Q^2(t)\rangle_{incoh}. \tag{4.9}$$

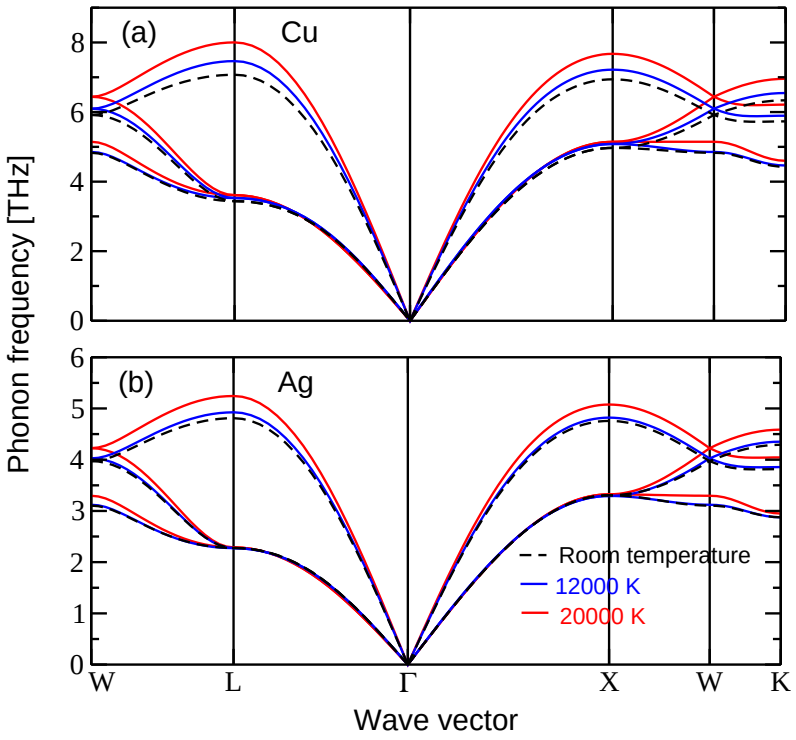

Figure 4.6: Phonon dispersion spectrum of (a) copper and (b) silver, before (at room temperature, black dashed curve) and after (at T_e = 12,000 K, blue solid curve and at 20,000 K, red solid curve) intense femtosecond-laser excitation.

Clearly, the incoherent lattice heating leads to an increase of the mean-square atomic displacements counteracting the squeezing effect. As we will show below, our calculations indicate that vacuum phonon squeezing can nevertheless be induced by a femtosecond-laser pulse.

4.5 Results

Femtosecond-laser pulses are known to induce bond hardening in noble metals [40, 57], but little is known about its origin and consequences. The following are the discussion on bond hardening and important results obtained, as a consequence of bond hardening in copper and silver.

4.5.1 Phonon dispersion spectrum

In order to confirm femtosecond laser-induced bond hardening in copper and silver over all points on the Brillouin zone (BZ), we calculated the full phonon spectra before and

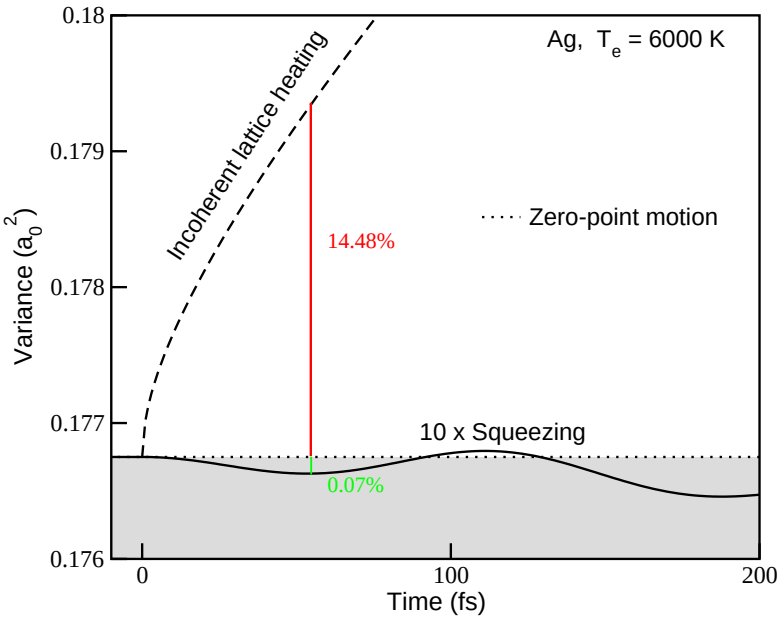

Figure 4.7: Time-dependent variance of the atomic displacements of silver averaged over the first BZ after the laser excitation leading to $T_e = 6000K$. The shaded region shows the zero-point motion in the initial state, dashed lines are due to incoherent lattice heating and black solid lines represent coherent variance (shown as 10 times of original data).

after laser excitation by performing *first principles* density functional theory (DFT) calculations. We calculated the effects of various laser fluences by changing T_e within the framework of electronic-temperature dependent DFT, and found that all phonon modes of both copper and silver harden as a function of T_e in the laser-excited potential (see figure 4.6). This is opposite to the behavior of most materials, which soften when electrons are excited. We obtained the greatest hardening at the L-point longitudinal mode, which frequency changes from 7.072 THz to 8.002 THz in copper and from 4.81 THz to 5.24 THz in silver, as T_e is elevated from room temperature to 20,000 K. Copper and silver are group 11 elements in the periodic table together with gold, which is so far the only element for which substantial laser-induced bond hardening has been observed [40].

4.5.2 Vacuum phonon squeezing: Average over first BZ

The time-dependent variance of the atomic displacement is observable from the time-resolved diffraction intensities through structure factors using time-dependent Debye-Waller theory [5, 40, 88]. Averaging over the first BZ, from equation 4.9 we found that the phonon squeezing is completely swamped by the effect of lattice heating. For example, in the case of silver after a laser excitation heating the electrons to 6000

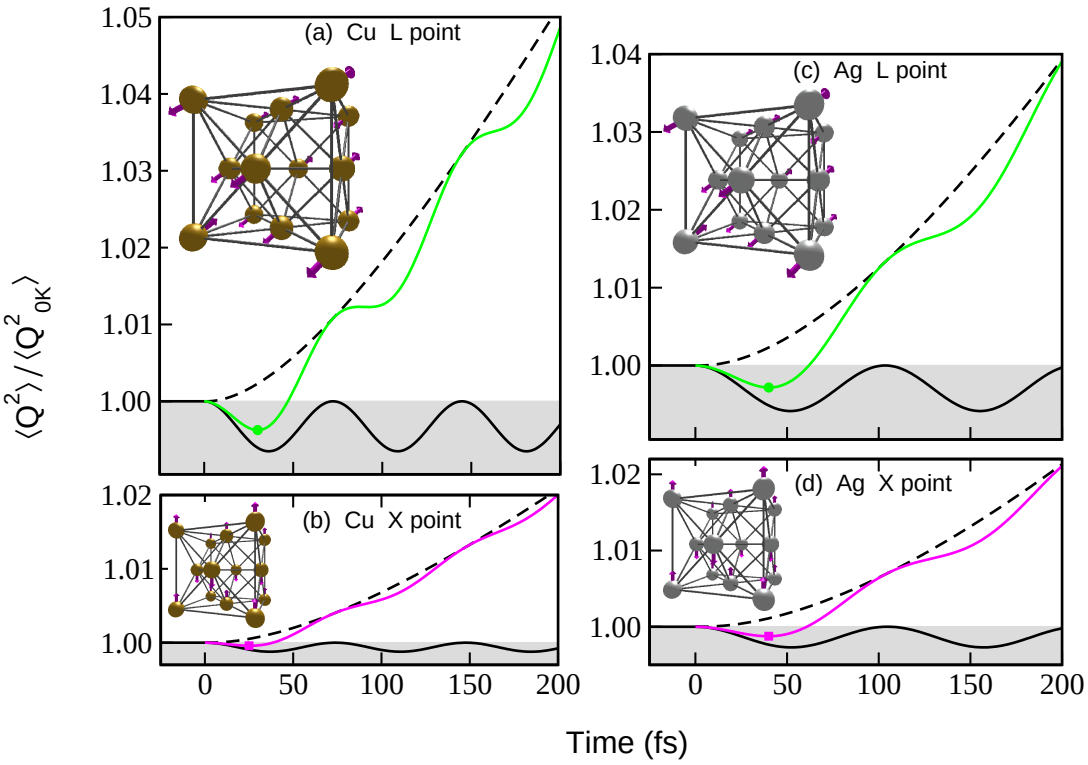

Figure 4.8: Normalized time-dependent variance of the atomic displacements (a) copper at the L-point (initial laser-induced $T_e = 3750$ K), (b) copper at the X-point (initial laser-induced $T_e = 2500$ K), (c) silver at the L-point (initial laser-induced $T_e = 5500$ K) and (d) silver at the X-point (initial laser-induced $T_e = 4500$ K). The solid black curves show coherent phonon squeezing and the dashed black curves incoherent lattice heating. The colored curves show the total variances. Filled symbols indicate the points of greatest squeezing. The shaded regions show the zero-point motion in the initial states.

K (figure 4.7), we found that coherent displacement $\langle Q^2(t)\rangle_{coh}$ decreases by 0.07% (green line in figure 4.7) due to phonon squeezing after 54 fs, whereas lattice heating $\Delta\langle Q^2(t)\rangle_{incoh}$ increases it by 14.48% (red line in figure 4.7) relative to the zero-point motion of the ground state potential. So, the incoherent lattice heating dominates the phonon squeezing.

4.5.3 Vacuum phonon squeezing: L- and X-points of longitudinal acoustic mode

Recent progress in time-resolved diffuse X-ray scattering techniques permits to explore the non-equilibrium lattice dynamics of particular phonon modes as well [89], by tracking both the average and mean-square displacement of atoms after intense laser excitation. Encouraged by this new development we studied the possibility of observ-

ing vacuum squeezing of longitudinal phonon modes at the L- and X-points in the BZ, which show a relatively large hardening after femtosecond-laser excitation (figure 4.6). The atomic displacements of the above mentioned points are illustrated in the insets of figure 4.8, whose main figures show the variance of the atomic displacements at the L- and X-point longitudinal modes of copper (silver) for an intense femtosecond-laser excitation leading to $T_e = 3750$ and 2500 (5500 and 4500) K. We see that immediately after the laser excitation $\langle Q^2(t)\rangle_{tot}$ dips below the zero-point motion (shaded regions in figure 4.8). The lowest values of $\langle Q^2(t)\rangle_{tot}$ have been reached after 30 (L-point) and 25 (X-point) fs in copper, and in both points after 40 fs in silver, they are denoted by filled symbols, which are the points with the greatest squeezing factors. Here we would like to mention that the TTM allows us to estimate the temperatures of the electrons and phonons averaged over all $\mathbf{q}$ vectors. However, the coupling strength of electrons with the lattice varies from point to point in the BZ and it is impossible to resolve a particular phonon mode using the TTM. In addition, even 40 fs are far too short for reaching thermal equilibrium among the lattice degrees of freedom [50, 89]. Consequently, at some points in the BZ, our approach based on the TTM is bound to underestimate the effects of lattice heating, while at other points it may overestimate $\Delta\langle Q^2(t)\rangle_{incoh}$. As our results indicate that vacuum phonon squeezing can be induced at different points in the BZ of copper and silver, we expect that the TTM, which provides the best currently available theoretical description of incoherent lattice heating, yields at least qualitatively correct order of magnitude predictions.

4.5.4 Squeezing factor

We repeated our simulations of femtosecond-laser-induced phonon squeezing for different excitation densities. The dependencies on electronic temperature of the momentum-resolved maximal squeezing factors for copper and silver at the L- and X-point longitudinal modes are shown in figure 4.9. We see that the squeezing factors increase with T_e up to a certain maximum value, after which they start to decrease. This decline is caused by the T_e dependencies of the electron-phonon coupling factor, which is nearly constant up to the temperature of ~ 3500 K for copper and ~ 5000 K for silver, and shows a significant strengthening at higher temperatures due to the thermal excitation of d band electrons (see figure 4.10) [2]. Vacuum squeezing in real space takes place only if $S > 0$. We found an optimal squeezing factor of 0.0019 (0.0014) at the L-point longitudinal mode of copper (silver) at $T_e = 3750$ (5500) K, which are three orders of magnitude greater than the previously reported quantum squeezing in a transparent $KTaO_3$ crystal [4]. From figure 4.8 it is clear, that the total variance dips steeper below the zero-point motion for the L-point than for the X-point in both copper and silver. In agreement, the greatest hardening occurs at the L-point compared to other phonon

wave vectors (see figure 4.6). In addition to the ultrafast bond hardening, which is a necessary condition for the achievement of vacuum squeezing, it is important to realize that squeezing can only overcome the lattice heating if copper (silver) is excited by an ultrafast pulse clearly shorter than the timescale of phonon squeezing, i.e., below 30 (40) fs.

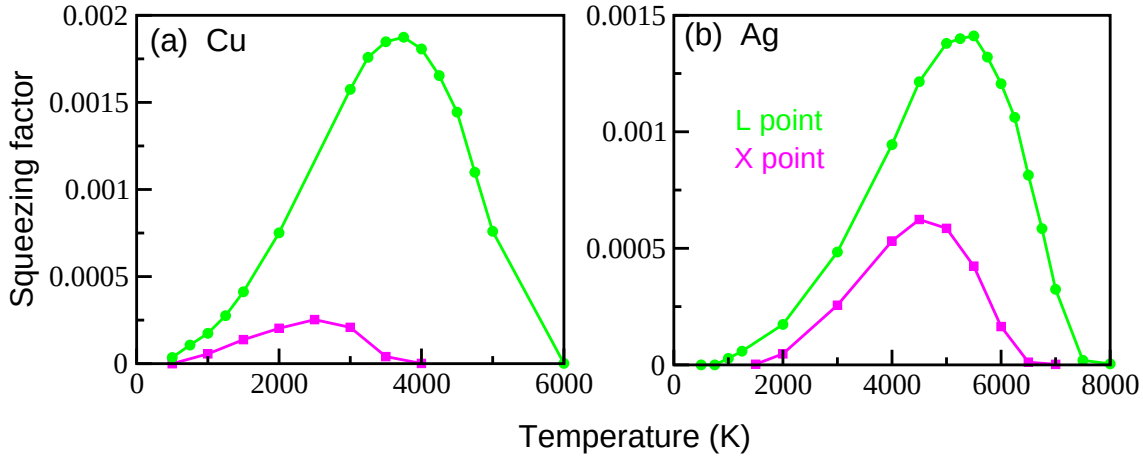

Figure 4.9: Momentum-resolved longitudinal squeezing factor S (a) copper and (b) silver at the L- (green circles) and X-point (pink squares) for various laser fluences heating the electrons to different initial temperatures. The squeezing effect reaches its maximum at laser fluences leading to T_e = 3750 and 2500 (5500 and 4500) K, respectively.

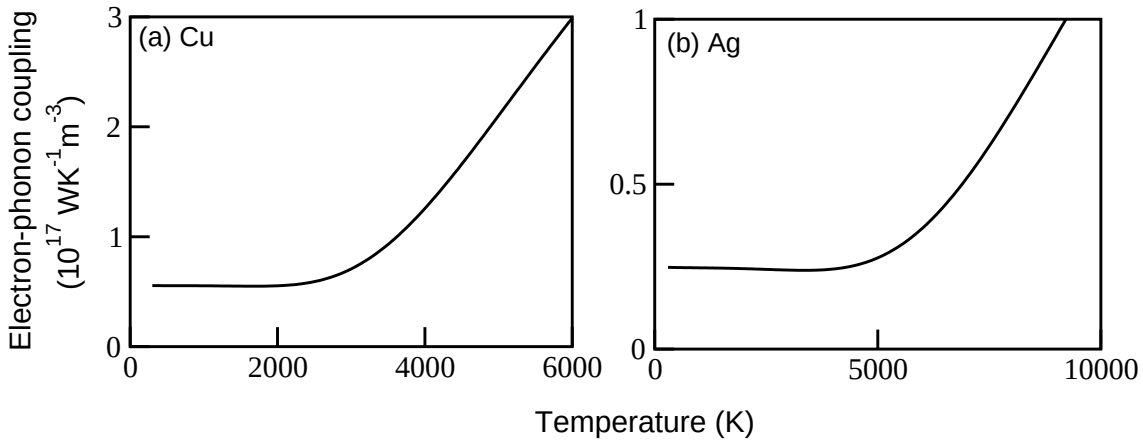

Figure 4.10: Electronic-temperature-dependent electron-phonon coupling of (a) copper and (b) silver from Ref. 2.

4.5.5 Direct evidence of bond hardening

Previously, ab initio calculations have predicted that hardening of phonon modes in gold due to increased T_e results in an increase of the melting time [40, 57], which provides strong evidence of bond hardening. The above mentioned observed delay in the melting time is small for aluminum, but has been shown to become large for gold [40]. We expect that such significant delay in melting should also be observable in silver. The conclusion that there is bond hardening on the basis of delayed melting relies, however, on electronic and lattice heat capacities and on the electron-phonon coupling parameter, which are calculated functions of the electronic excitation, and is therefore indirect. In contrast, the time-dependent variance of the atomic displacement is directly observable from the time-resolved diffraction intensities through structure factors using time-dependent Debye-Waller theory [5,40,88]. Recent progress in time-resolved diffuse X-ray scattering techniques permits to explore the non-equilibrium lattice dynamics of particular phonon modes as well [89, 90]. Measuring vacuum squeezing in real space by means of diffuse background scattering would thus provide direct evidence of bond hardening, because the coherent part of the squeezing (equation 4.3) depends only on the laser-modified potential.

Ultrafast electron and X-ray diffraction enable the direct observation of atomic motions with a time resolution of a few hundred femtoseconds or better. Using the above technique, it was found that the variance of the atomic displacements in bismuth [5] after femtosecond-laser excitation first grows and then performs a damped oscillation, both processes caused by the laser-induced changes of bond strengths. The above mentioned experiments were performed close to room temperature, so that the product of the variances of the conjugate phonon variables stayed well above the limit provided by the Heisenberg uncertainty principle (see figure 2(c) in [5]), but it has been anticipated that ultrafast-laser induced changes in the bond strengths at low temperatures may induce a vacuum phonon squeezed state [5]. Bismuth, however, exhibits laser-induced bond softening [6,81], which leads to an initial broadening of the phonon wave packet preventing vacuum squeezing in real space. Based on this and on the general fact that intense laser pulses produce a rapid lattice heating through electron-phonon interactions [86], one might be tempted to conclude that vacuum phonon squeezing in absorbing materials is not possible. Nevertheless, we found that copper and silver show, in contrast to bismuth, bond hardening upon ultrashort-laser excitation [48,91].

Our maximum predicted vacuum phonon squeezing factor in noble metals is of the order of 10^{-3}. Provided one could find materials with greater bond hardening or a smaller electron-phonon coupling factor it might be possible to improve this result by one or two orders of magnitude. Although we have in this work concentrated on copper and silver, because the behaviour of their bonding properties upon laser excitation was

unknown, based on their chemical and physical similarities we expect that vacuum phonon squeezing could also be achieved in gold.

CHAPTER 5

Decay of coherent phonons in antimony

5.1 Introduction

Developments in time- and angle-resolved optical spectroscopy [92, 93], and time-resolved diffraction techniques [94] using powerful femtosecond-pulsed lasers now allow direct time domain investigations of phonon motion, and phonon-phonon and electron-phonon couplings. The interaction of a femtosecond-laser pulse with a material leading to sudden changes in the potential energy surface, may give rise to many interesting ultrafast structural phenomena, such as, generation of coherent phonon oscillations, thermal phonon squeezing, nonthermal melting, etc.

Irradiating a solid with an ultrashort laser pulse will make the selected phonons, which normally vibrate with random phases, oscillate in phase. This is called the coherent excitation of phonons, which is a general phenomenon occurring whenever ultrashort laser pulses interact with solids. A necessary condition to produce coherent phonons is the availability of Raman-active transitions and a laser pulse with pulse duration less than the oscillation period of phonons. In quantum mechanics, the coherent state is a minimum uncertainty state and its fluctuation properties are like those of the vacuum state. However, laser-excited coherent phonons involve the motion of all or a macroscopic number of atoms in a solid and can safely be treated classically. In crystals, the excitation and measurement of coherent oscillations can be of great importance for fundamental explorations and for studying the ultrafast dynamics of the excited states on atomic length scales. The magnitude and dynamics of coherent phonons will depend on the specifics of the electronic structure and electron-phonon, and phonon-phonon interactions of the material.

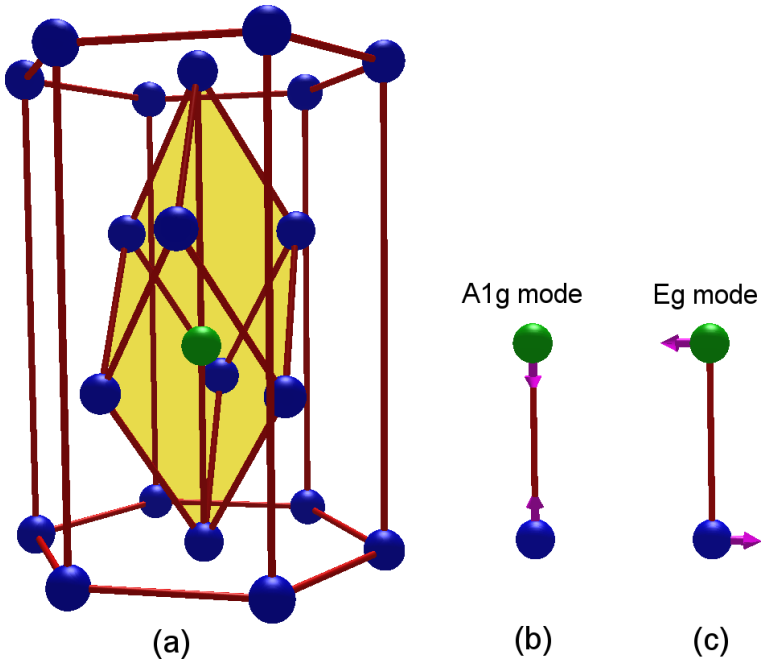

Figure 5.1: (a) Crystal structure of antimony. The second atom along the trigonal axis is marked in green color. (b) In the A_{1g} phonon mode the atoms move in the direction of the trigonal axis. (c) In the two doubly degenerate E_{1g} phonon modes the atoms move in the perpendicular plane.

Antimony (Sb) has been the focus of many studies of high amplitude coherent phonon generation because it has higher melting point than for example Bi, which makes Sb more resilient to ultrashort laser irradiation. In Sb the coherent phonon generation is due to a displacement of $A1$ symmetry of the ion quasi-equilibrium coordinate produced by electronic excitation, which is the displacive excitation of coherent phonons. The aim of this work is to provide a better description of phonon dynamics in laser-excited Sb on the picosecond time scale.

5.2 Crystal structure of Antimony (Sb)

Sb is group Vb semimetal with rhombohedral A7 [95] crystal structure, with lattice parameters $a = 4.3007$ Å, $c = 11.2221$ Å and $\alpha = 57.1075°$, which can be derived from a simple cubic lattice rombohedrally distorted along the body diagonal. The direction of the trigonal axis is usually chosen as the z-axis. There are two atoms in the unit cell, the second located a fractional distance z along the trigonal axis. The center of the inversion symmetry lies midway between these two atoms. In its equilibrium configuration the internal displacement parameter, $z = 0.2336$, instead of 0.25 in the

original cubic lattice. If $z = 0.25$, i.e., half way along the trigonal axis and $\alpha = 60°$, this would be a simple cubic structure with one atom per cubic unit cell. The observed deviation from cubic symmetry is caused by the so-called Peierls distortion, introducing a small band gap over a certain range in the Brillouin zone, which is responsible for several characteristic properties of Sb. A unit cell of Sb is shown in figure 5.1(a).

5.3 Phonon modes in Sb

Having two atoms in each unit cell, Sb has six phonon branches, three acoustic and three optical phonons. The optical phonon modes are Raman active, namely one totally symmetric A_{1g} mode, which is the Peierls distortion mode parallel to the trigonal axis and two doubly degenerate E_g modes, which are perpendicular to the trigonal axis. The motion of atoms in a unit cell corresponding to each mode are schematically shown in figure 5.1(b) and (c).

5.4 Coherent phonon generation

The strong coupling between the A_{1g} phonon mode and the excited electrons lead to a predominantly displacive generation of coherent A_{1g} phonon in Sb [96]. Displacive excitation (see figure 5.2) was proposed for the totally symmetric modes in opaque materials. Because of the Peierls distortion, which is of electronic origin, the equilibrium structure of Sb is very sensitive to the excitation of electrons. When the electrons are excited, the structure relaxes towards the more symmetric configuration. That means the value of z shifts towards the value 0.25, with increased excitation. This cause the changes in atomic position in Sb after laser excitation, so that the atoms oscillate about their new equilibrium positions. The strong coupling between the A_{1g} phonon and the excited electrons leads to the generation of large amplitude coherent phonons. The phonon-phonon interaction processes can cause a gradual decay of coherent phonon oscillations. This is because of the interaction between the phonon modes result in the decay of a phonon into other phonon modes. The rate of decay depends on how strongly the phonon modes are coupled.

The coherent phonon generation is schematically illustrated in figure 5.2. Before the laser excitation the atoms are at the equilibrium positions (z) of the ground state potential. Interaction of a femtosecond laser pulse with a solid results in an abrupt change in the free energy of the crystal lattice, which responds to the new excited electronic state by moving towards a new equilibrium position $z^{'}$. Such atomic displacement in a crystal after laser excitation induces the coherent oscillations of the

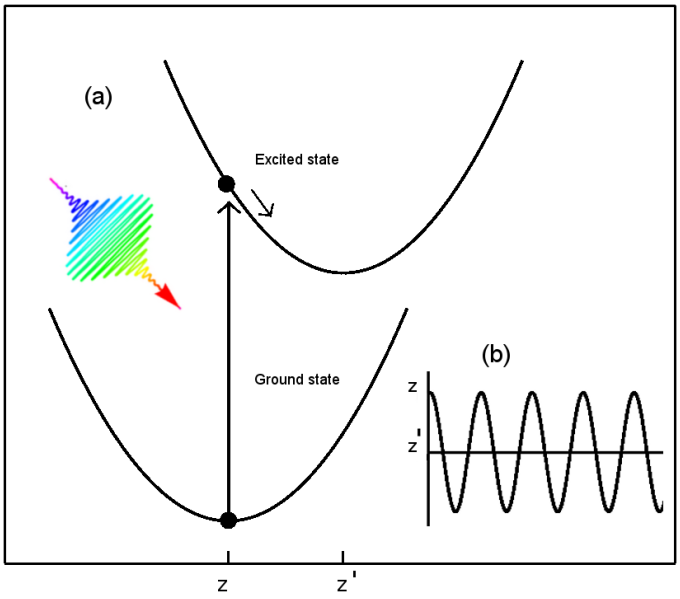

Figure 5.2: Schematic illustration of coherent phonon generation. (a) The curves show the potential energy surface of ground and excited electronic states along the trigonal axis. The vertical arrow indicates the transition of the atom from the ground to excited state. (b) The atom starts to oscillate coherently around the new equilibrium position $z^{'}$ in the excited state.

atoms around their new equilibrium positions. Figure 5.2(b) represents the coherent phonon oscillation around new equilibrium position $z^{'}$.

We performed studies on the decay of coherent phonons in femtosecond-laser-excited Sb. The dynamic evolution of the excited state potential energy surface along the A_{1g} phonon coordinate is explored using accurate molecular dynamic simulations. In our work, the oscillations of the A_{1g} mode are calculated from the variation of the parameter z.

5.5 Methods

We performed a microscopic theoretical study of the coherent phonon in Sb upon laser excitation using electronic-temperature-dependent density functional theory. In order to be able to study a sufficiently large supercell we developed our own Code for Highly-excIted Valence Electron Systems (CHIVES) (see section 2.6.3) [28], which uses norm conserving Goedecker-Teter-Hutter relativistic pseudopotentials [23]. CHIVES provides a more natural description of ultrafast phenomena and is orders of magnitude faster than other existing codes [97]. We used a primitive Gaussian basis set for Sb

with exponents $a_1 = 1.73466\ a_0^{-2}$ (s orbital), $a_2 = 1.17728\ a_0^{-2}$ (s and p orbitals), $a_3 = 0.24788\ a_0^{-2}$ (s p and d orbitals) and $a_4 = 0.06955\ a_0^{-2}$ (s and p orbitals) together with a regular three dimensional grid to describe the Hartree, exchange and correlation potentials, and the local density approximation. For our systems we used 2x2x2 **k**-grid.

Two approaches based on an ab-initio calculations [6, 27] have been proposed to describe the nonequilibrium electron distributions. In Ref. [6] it was assumed that electrons and holes can be described by two Fermi-Dirac distributions with the same temperature but different chemical potential. While in Ref. [27] it has been assumed that electrons and holes can be described by a unique Fermi-Dirac distribution. For Sb we used the second method with single chemical potential for both electrons and holes because Giret *et al.* [98] firmly establish that a single chemical potential approach, which is reliable for describing the excited electrons and provides a complete scenario for the generation of coherent phonons in solids with A7 crystal structures.

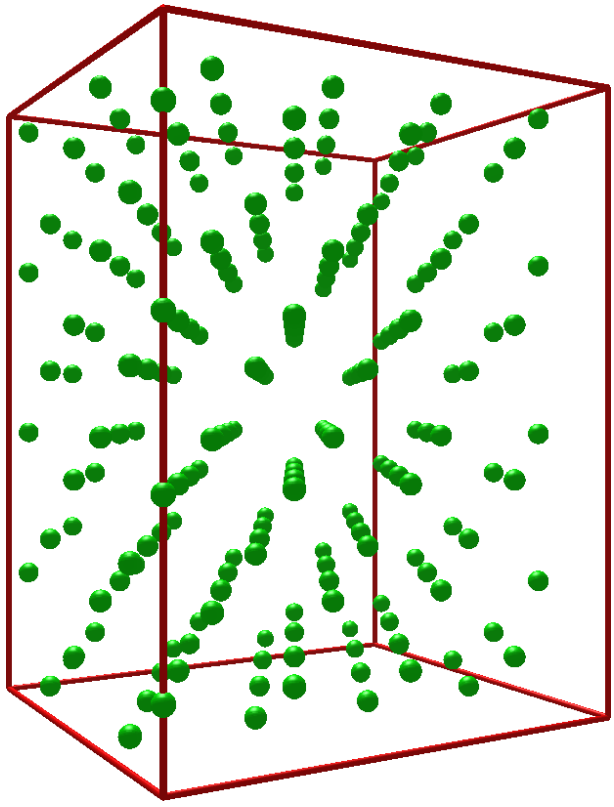

Figure 5.3: Antimony supercell with 192 atoms.

To study the coherent phonon dynamics we performed molecular dynamics simulations on supercells with N = 72, 144 and 192 atoms. In figure 5.3 we show the atomic positions of our 192 atom supercell. To get the equilibrium positions, we relaxed each supercell to the minimum potential energies possible. All phonon modes of Sb are cal-

culated by displacing an arbitrary atom from its equilibrium position by 0.001 a_0 along x, y and z directions. Using the computed forces on all the atoms and the symmetry of the lattice we constructed the 3Nx3N dynamical matrix, whose orthonormal eigenvectors e_i are phonon directions, which are directly related to the phonon eigenvectors ϵ_i, and obtained the phonon frequencies ν_i from the eigenvalues. Using the computed forces in the velocity Verlet scheme, we performed molecular dynamics simulations with a time step of 5 fs. We initialized and scaled the atomic velocities υ and displacements u in the direction of ϵ_i, using inverse transform sampling and 6N true random numbers r_i lying uniformly on [0,1] so as to reproduce a Maxwell-Boltzmann distribution with initial lattice temperature $T_l^{(i)} = 0.95$ mHa (300 K), using

$$\upsilon_i^{(i)} = \sqrt{2k_B T_l^{(i)}}\ f(2r_i - 1), \qquad i = 1, ..., 3N \tag{5.1}$$

$$u_i^{(i)} = \sqrt{\frac{2k_B T_l^{(i)}}{\omega_i^{(i)2}}} f(2r_{i+3N} - 1), \qquad i = 1, ..., 3N \tag{5.2}$$

where f is the inverse error function, $\omega = 2\pi\nu$ and the superscript (i) represent the initial values before laser excitation. And are scaled by

$$\upsilon_i^{(i)} = \alpha\, \upsilon_i^{(i)}, \tag{5.3}$$

$$u_i^{(i)} = \alpha\, u_i^{(i)}, \tag{5.4}$$

where α is the scaling factor calculated from the total energy of the system,

$$\alpha = \sqrt{\frac{\frac{3}{2}(N-1)\, k_B\, T_l^{(i)}}{\frac{M}{2} \sum_i [\, {\upsilon_i^{(i)}}^2 \ + \ {\omega_i}^2\, {u_i^{(i)}}^2]}}\,. \tag{5.5}$$

Before applying a femtosecond-laser pulse, we thermalized each supercell at room temperature using initialized atomic velocities and displacements. Then, we let the system evolve for a sufficiently long time, until the initial kinetic energy is fairly distributed between kinetic and potential degrees of freedom. The lattice temperature T_l and its time average $\langle T_l(0:t)\rangle$ (figure 5.4) are calculated at each step of thermalization using,

$$T_l(t) = \frac{\sum_{i=1}^{N} \frac{1}{2} M v_i^2(t)}{\frac{3}{2}(N-1)k_B}. \tag{5.6}$$

The evolution of interatomic coordinate $z(t)$ during the thermalization process are studied from:

$$z(t) = \frac{1}{N} \sum_{i=1}^{N} (-1)^i\ \Delta z_i(t). \tag{5.7}$$

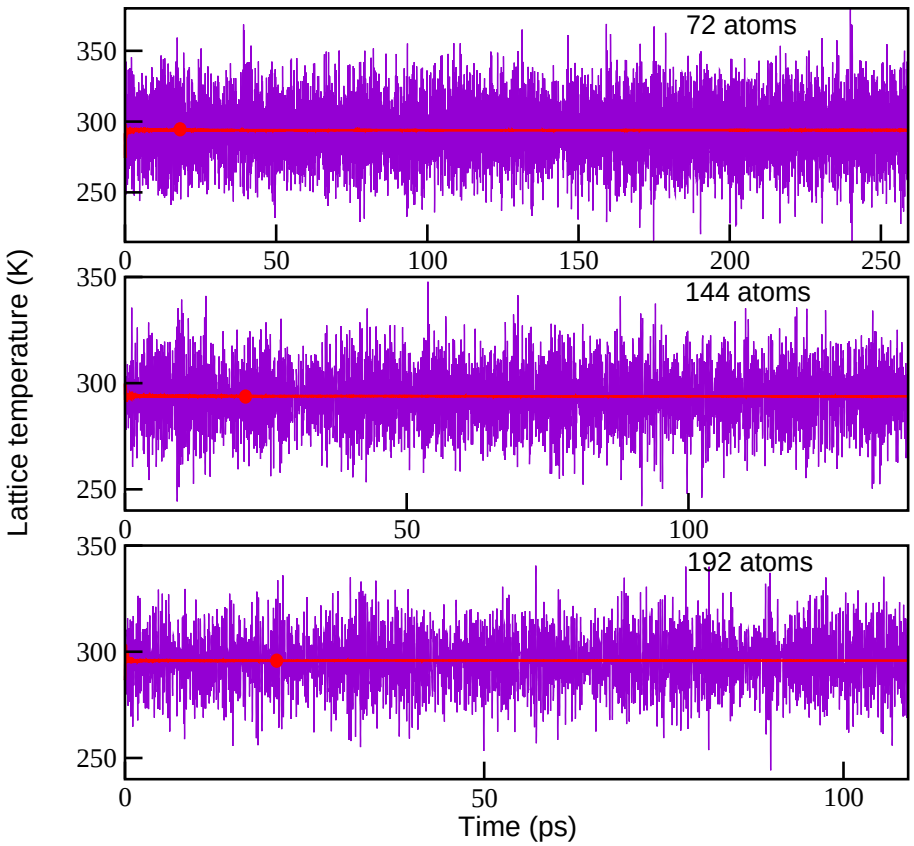

Figure 5.4: Thermalization dynamics: Time-averaged lattice temperature for different supercells. Thermal equilibrium is reached after $\sim$ 20 ps (filled symbols).

The time average of interatomic coordinate $\langle z(0:t)\rangle$ is shown in figure 5.5. We found that the systems thermalized after $\sim$ 20 ps (see figure 5.4 and 5.5). We performed molecular dynamics simulations at every 1 ps snapshots from themalization after 20 ps. Starting from these snapshots we increased the electronic temperature T_e in order to simulate the effects of femtosecond-laser excitation on Sb at various fluences. We averaged our results of molecular dynamics simulations over the number of independent runs (N_{runs}),

$$\bar{z}(t) = \frac{1}{N_{runs}} \sum_{i=1}^{N_{runs}} z_i(t), \tag{5.8}$$

where $\bar{z}(t)$ is the mean value of the internal coordinate z at a time t and $z_i(t)$ is the value in the i^{th} run at time t. The time-dependent errors $\Delta\bar{z}(t)$ for the displacement were calculated from

$$\Delta\bar{z}(t) = \sqrt{\frac{\sum_{i=1}^{N_{runs}}[z_i(t) - \bar{z}(t)]^2}{N_{runs}(N_{runs}-1)}}. \tag{5.9}$$

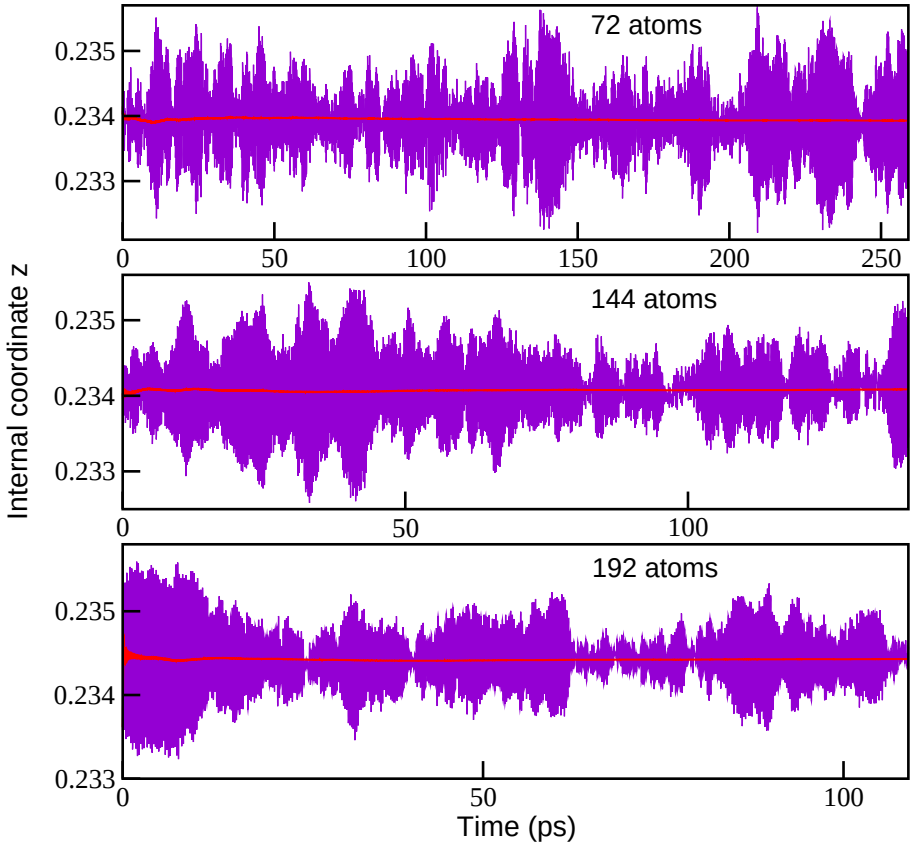

Figure 5.5: Thermalization dynamics: Time-averaged internal coordinate z for different supercells.

In our simulations, the initial T_l was set to 300 K and T_e after femtosecond-laser excitation varied from 1000 to 4000K. We used the frozen phonon method to investigate the effect of anharmonicity of the A_{1g} phonon mode. The laser-induced shift (z'') of potential minimum along the z-direction is studied from the anharmonic coupling between the phonon modes using the equation (see Appendix B for derivation),

$$dV^{ph-ph} = \frac{1}{2}\, k_B T_l \sum_{i=4}^{3N-1} \frac{1}{(\omega_i^2)}\, \frac{\partial(\omega_i^2)}{\partial(z'')}\, dz'' \,, \tag{5.10}$$

by integrating equation 5.10 with respect to z'' one will get the potential energy of the phonon modes V^{ph-ph} as the following,

$$V^{ph-ph} = \frac{1}{2}\, k_B T_l \sum_{i=4}^{3N-1} \ln(\omega_i^2) + C \,, \tag{5.11}$$

where ω is the coherent phonon frequency, and C is an integration constant. Here we would like to mention that the higher harmonics [99] arising from the coupling

between phonon modes in Sb would be interesting to investigate but is out of the scope of present study.

As mentioned before, the coherent phonon oscillation can be directly determined by plotting z as a function of time, which is equivalent to projecting the atomic coordinates onto the A_{1g} phonon eigenvector. The frequencies, amplitudes, shifts in z and decay times of the coherent A_{1g} mode at various T_e for different supercells were determined by fitting the time-domain data to a damped harmonic oscillation with a single exponential decay:

$$\Phi(t) = A_0 + A\ \exp(\frac{-t}{\tau})\ \cos(\omega t), \tag{5.12}$$

where A_0 is the shift in z, A is the amplitude, ω is the frequency and τ is the decay time of the coherent phonon oscillations.

5.6 Results

Femtosecond-laser induced changes in potential energy surfaces, coherent phonon dynamics and phonon-phonon coupling of Sb are studied from molecular dynamics simulations using the code CHIVES. The following are the important results obtained:

5.6.1 Femtosecond-laser induced Coherent phonon dynamics

From thermalization dynamics we observed that the system reaches thermal equilibrium after a particular time ($\sim$ 20 ps). After 20 ps the equilibrium ionic temperature reached a constant value in the range of 294-296 K (see figure 5.4). We investigated the phonon dynamics in laser-excited Sb below the limit of a structural phase transition.

Table 5.I: The single exponential fitting parameters of A_{1g} phonons for different supercells at T_e = 3000 K.

Supercell (N)	Number of runs N_{runs}	Shift (A_0) z	Amplitude (A) z	Frequency ($\frac{\omega}{2\pi}$) THz	Decay time (τ) ps
72	240	0.2358	-0.00185	3.2135	2.8454
144	120	0.2359	-0.00195	3.2137	2.8069
192	90	0.2362	-0.00185	3.2066	2.6991

In order to understand the decay of coherent phonons and phonon-phonon interaction in our systems after femtosecond-laser excitation, we studied the time-dependent coherent oscillation and kinetic energy of the A_{1g} mode (see figure 5.6) during the first

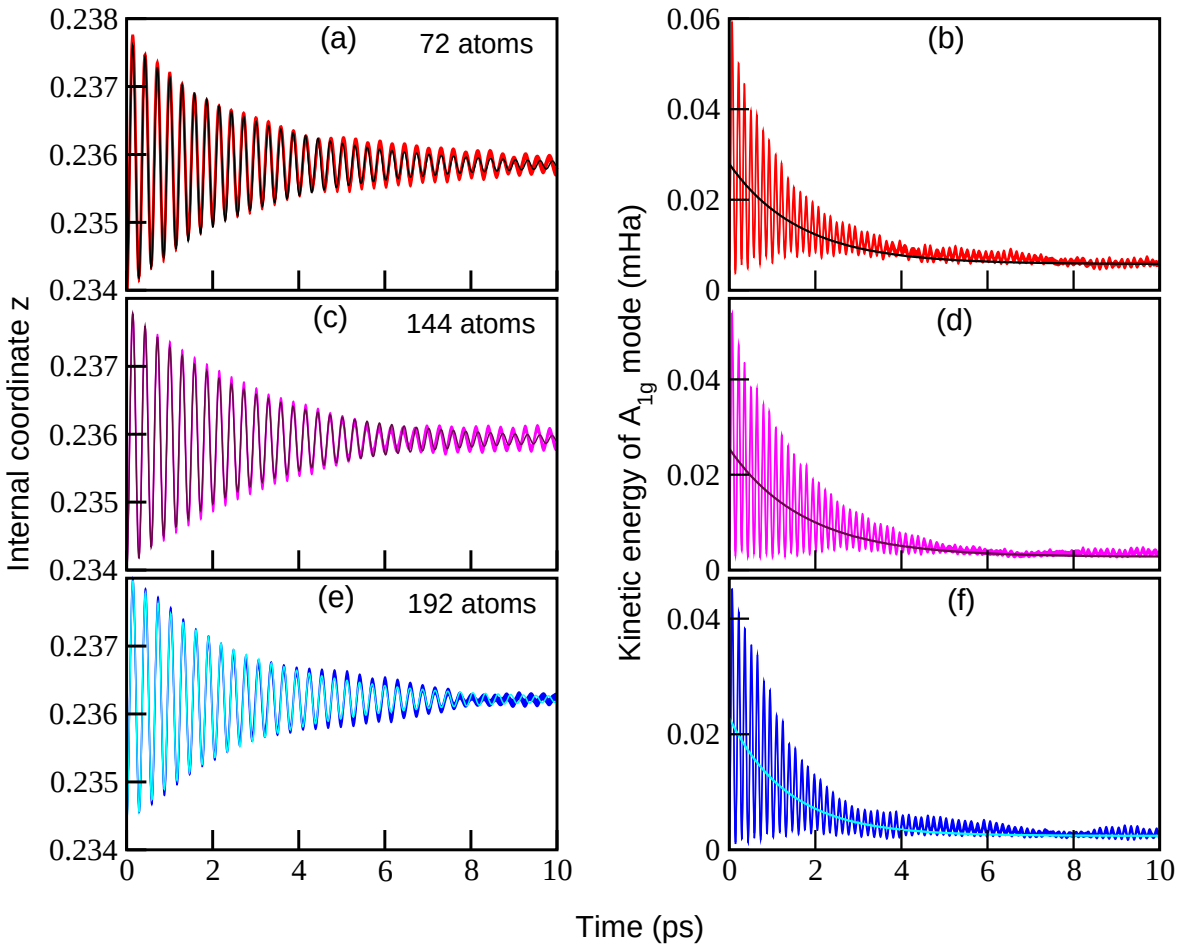

Figure 5.6: Ab-initio molecular dynamics results: Time-dependent atomic coordinates along the direction of the A_{1g} mode (first column) and kinetic energies (second column) for different supercells ((a) and (b) for N = 72 atoms (red), (c) and (d) for 144 atoms (pink), and (e) and (f) for 192 atoms (blue)) at $T_e = 3000$ K. The shaded areas are the standard deviations of the averages and the solid curves represent the exponential fit of the data.

10 ps after femtosecond-laser excitation leading to electronic temperature $T_e = 3000$ K. In order to obtain good statistics, the results of 72 atom supercell is averaged over 240 runs, 144 atom supercell is averaged over 120 runs and of 192 atom supercell is averaged over 90 runs. We plotted the results $\bar{z}(t) \pm \Delta\bar{z}(t)$ in figure 5.6. The shaded areas represent the standard deviations of the averages and the solid curves are the exponential fits. Fitting the damped oscillation with a single exponential decay gives the phonon decay time $\tau = 2.85$, 2.81, and 2.70 ps for supercells N = 72, 144 and 192, respectively, which are in reasonable agreement with the experimentally observed decay time for antimony $\tau = 2.9$ps [8,9,100,102]. The decay rate obtained from the work indicates that the decay of coherent phonons in Sb is dominated by anharmonic decay.

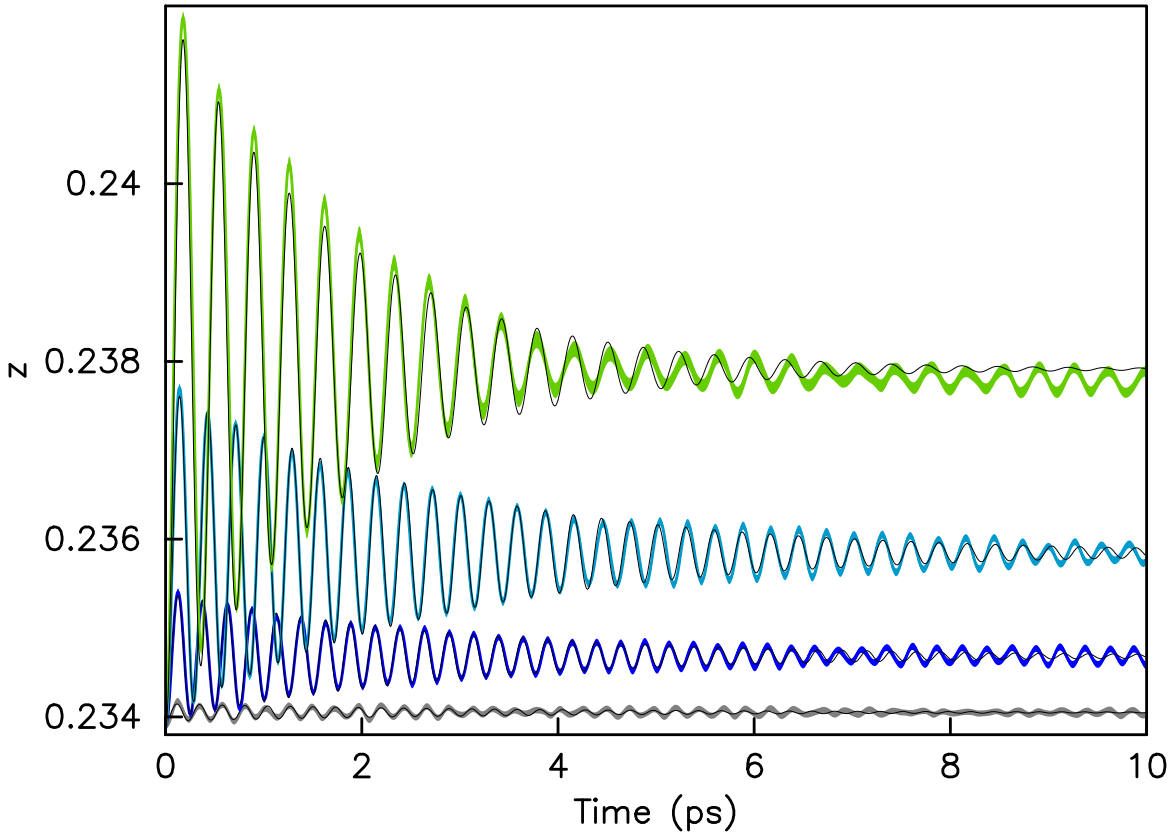

Figure 5.7: Time-dependent internal coordinates along the direction of A_{1g} mode for different laser excitation leading to T_e = 1000 (grey), 2000 (blue), 3000 (cyan) and 4000 (green) K. The shaded areas represent standard deviations of the averages and the solid curves represent the single exponential fits.

The fitting paremeters of the damped harmonic oscillation with a single exponential decay are tabulated in Table 5.I.

In order to analyse the temperature-dependent coherent phonon dynamics in Sb, we have studied the A_{1g} phonon mode decay at different laser fluences (T_e =1000, 2000, 3000 and 4000 K) using a supercell having 72 atoms. In figure 5.7 we have drawn the displacement z of the A_{1g} mode. As above, we fitted the coherent oscillations to a damped harmonic oscillator with a single exponential decay. The fitted parameters are tabulated in Table 5.II. From Table 5.II one can see that the decay times τ for A_{1g} coherent phonons in Sb vary with the laser fluence. The shift (A_0) in z increases with T_e. Peierls distortion disappears when z reaches the value 0.25, where the system undergoes solid-solid phase transition [101]. The frequency of coherent phonon oscillation ω decreases with T_e.

Table 5.II: The single exponential fitting parameters of A_{1g} phonons for 72 atom supercells at different T_e.

T_e	Shift (A_0)	Amplitude (A)	Frequency ($\frac{\omega}{2\pi}$)	Decay time (τ)
K	z	z	THz	ps
1000	0.2341	-0.0009	4.3241	3.4471
2000	0.2347	-0.0071	3.9857	2.9195
3000	0.2358	-0.0185	3.4872	2.8454
4000	0.2379	-0.0411	2.7714	1.7277

5.6.2 Laser-excited potential energy surfaces

Table 5.III: The internal coordinate for ground state (z), laser-excited state ($z^{'}$) and shifted ($z^{''}$), calculated from equation 5.11, due to anharmonic coupling at T_e = 3000 K.

Supercell (N)	z	$z^{'}$	$z^{''}$
72	0.2335	0.2349	0.2358
144	0.2337	0.2350	0.2359
192	0.2340	0.2353	0.2362

We observed that the coherent phonon oscillations, starting from the equilibrium reduced atomic coordinates z, are not oscillating around the new reduced coordinates $z^{'}$ after laser excitation (figures 5.6 and 5.7). For a detailed description, in the case of the 72 atom supercell at T_e = 4000 K (figure 5.8), the reduced atomic coordinates at the ground state z and laser-excited state $z^{'}$ are 0.2335 and 0.2363 respectively. But from figure 5.8 it is clear that the coherent phonon of the above system oscillates around a new value $z^{''}$ = 0.2379 (Table 5.II) instead of 0.2363, which is because there is a strong anharmonic coupling between the phonon modes in Sb.

Insight into the phonon coupling of Sb can be gained by considering the laser-induced evolution of the potential energy surface of crystalline Sb along the direction of the Peierls distortion. The shift in z due to anharmonic coupling was calculated using equation 5.11 for a range of values of z about its equilibrium, at T_e = 3000 K for all supercells and are in perfect agreement with the single exponential fitting data of our molecular dynamics simulations (Table 5.I and 5.III).

For detailed description about the properties of potential energy surfaces, we analyzed 72 atom supercell using equation 5.11 at different laser fluences (T_e = 1000, 2000, 3000 and 4000 K), see figure 5.9. From figure 5.9 it is clear that the minimum of potential energy surface shifted from 0.2341 to 0.2379 after laser excitation leading to

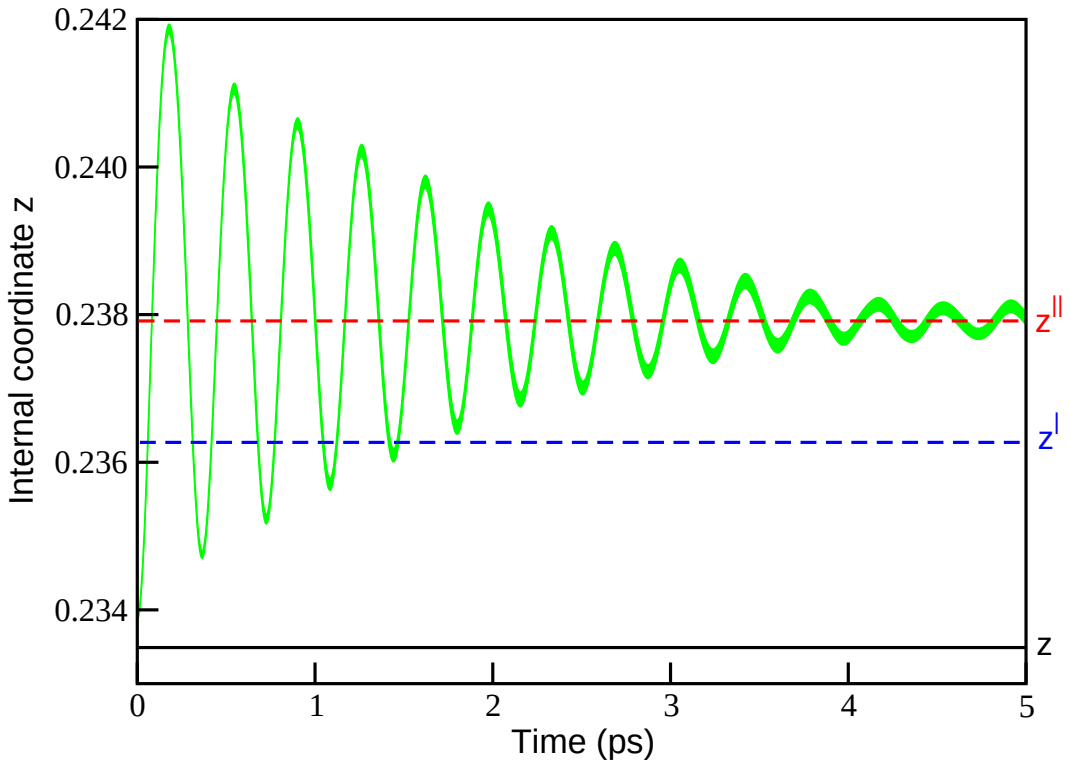

Figure 5.8: Coherent A_{1g} phonon oscillation in the 72 atom supercell at T_e = 4000 K. z and $z^{'}$ are the internal lattice parameter at the ground state and laser-excited state, respectively. The coherent A_{1g} mode oscillats around a new value $z^{''}$ due to anharmonic coupling.

T_e from 1000 to 4000 K. As mentioned above, the coherent A_{1g} phonons of Sb oscillate around new equilibrium positions, which are additionally shifted due to phonon-phonon coupling. The laser-induced shift of potential minimum along the z-direction gives the driving force to the coherent A_{1g} phonon oscillations. We found that the position of minimum shifts linearly with T_e, as the minimum approaches equidistant from two neighboring atoms, i.e., $z = 0.25$ with an accompanying loss of Peierls distortion. Based on the T_e dependence of potential energy surface we can establish a correlation between ultrafast phonon dynamics and dynamical evolution of the potential energy surface of Sb upon laser excitation.

In the electronic ground state the total energy of the system was minimized for z = 0.2335. At this equilibrium state we obtained A_{1g} and E_g phonon frequencies of 4.6832 and 3.2304 THz, respectively, which are in reasonable agreement with the experimentally observed values 4.5 and 3.3 THz [8,102]. The femtosecond-laser excitation hardly affects the potential energy surface of the solid. The excited state potential energy surfaces are flatter than that of ground state. As a consequence all phonon modes of Sb are softened. From figure 5.9 one could observe that potential energy surface softens with T_e. In figure 5.10 we plot the T_e-dependent A_{1g} mode frequency upto

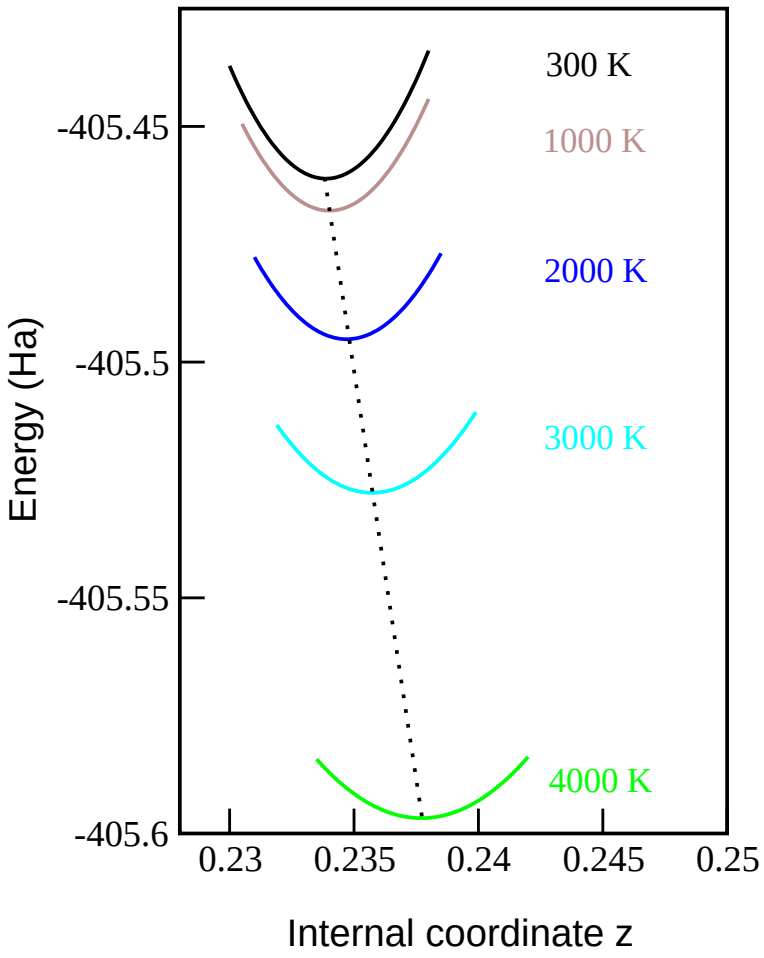

Figure 5.9: Laser-excited potential energy surfaces of Sb at various laser fluences.

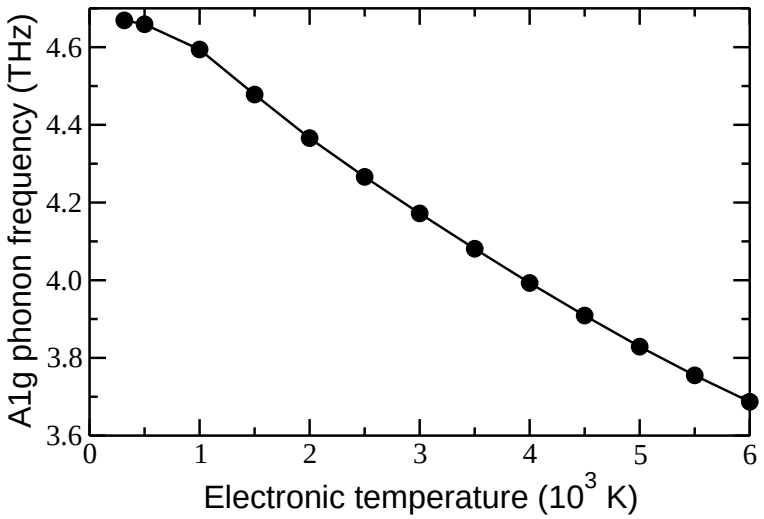

Figure 5.10: Coherent A1g phonon frequencies of Sb as a function of T_e.

6000 K and we found that with increasing T_e the frequency redshifts. The change in equilibrium value of internal coordinate z in the excited state is the dominating factor in the softening of the optical modes in Sb [103].

5.6.3 Thermal squeezing

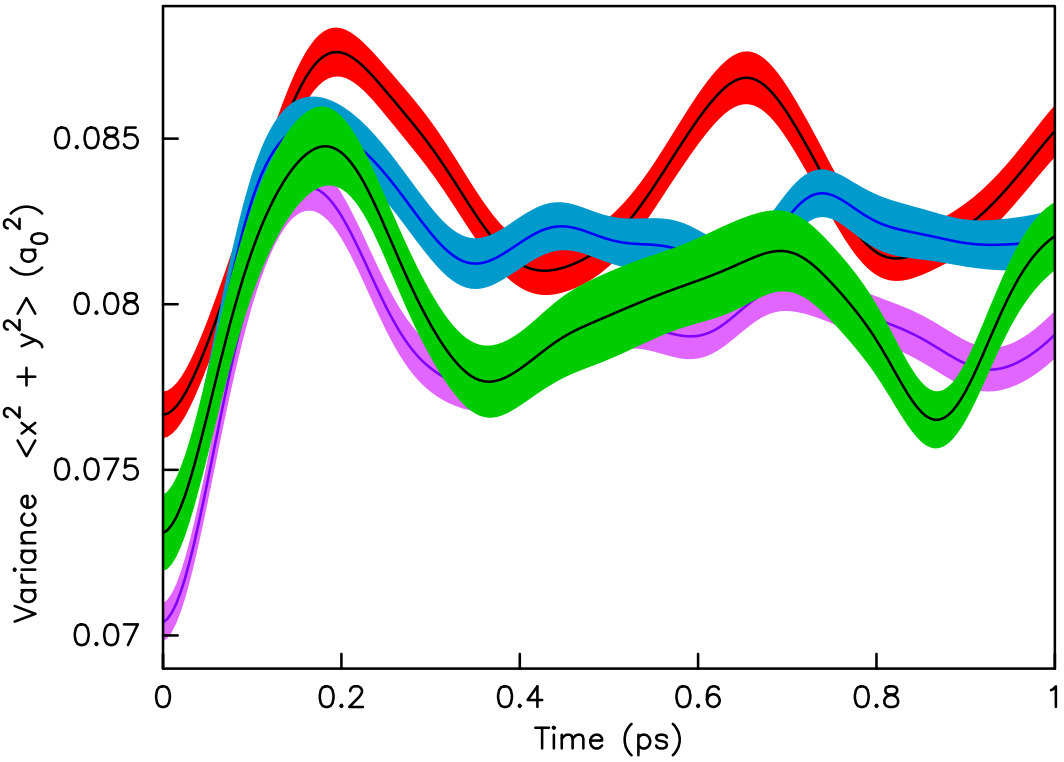

Figure 5.11: Time-dependent variance, $\langle \Delta x^2 + \Delta y^2 \rangle$ of the atomic displacements at the electronic temperature of 4000 K for super cells having N = 72 (red), 144 (pink), 192 (blue) and 288 (green) atoms. The shaded areas represent standard deviations of the averages (solid curves).

When an ultrashort laser pulse softens the interatomic bonds of a solid without changing the crystal structure, the atoms will, after the laser pulse, on average move further away from their ground state position than before laser excitation, which manifests itself as a decrease of X-ray- or electron-diffracted Bragg intensities [5]. In addition, as a function of time, some oscillations in the Bragg peak intensities can be observed [5]. This process is called thermal phonon squeezing [50].

The microscopic mechanism of femtosecond-laser-induced thermal squeezing [50] for an ensemble of nearly degenerate phonon modes is the following: Before laser excitation the thermal distribution of the atomic displacements is in equilibrium with

the harmonic potential. Through a femtosecond-laser pulse the potential softens almost instantaneously rendering the initial distribution function too narrow (squeezed) for the actual potential, so that, on average, the atoms start to move outward, After a quarter of a phonon period the distribution reaches its maximum width, which is wider than the equilibrium distribution of the laser-excited potential. Thereupon the distribution narrows again and after half a period, the displacements are back near their initial absolute values, albeit with opposite signs. The narrowness of the initial distribution is however not fully regained due to anharmonicities and phonon-phonon interactions. Depending on the strength of these effects, further oscillations may be observed.

In Sb, the laser pulse changes the equilibrium z coordinate. As a consequence, by measuring ultrafast changes in Bragg peaks that are only sensitive to the variance $\langle \Delta x^2 + \Delta y^2 \rangle$ of the in-plane atomic positions, Johnson *et al.* [5] could observe thermal phonon squeezing in Bi, which is isostructural to Sb. Here we analyzed the variance $\langle \Delta x^2 + \Delta y^2 \rangle$ of our molecular dynamics runs for Sb after femtosecond-laser excitations of moderate intensities (T_e = 1000 - 4000 K). See figure 5.11, for further insight into the nature of atomic motions for different supercells (N = 72, 144, 192, and 288) after laser excitation leading to T_e = 4000 K. We expect that the same pathways are follow during the initial stages of thermal phonon squeezing at low excitation densities and during nonthermal melting at high excitation densities. So, the studies of thermal phonon squeezing at low fluences should help to understand the ultrafast structural changes in Sb at higher excitation fluences. Such studies between thermal phonon squeezing and nonthermal melting in Sb are important and have not been studied.

5.7 Discussion

Using CHIVES we simulated for the first time the full atomic dynamics of Sb after femtosecond-laser excitation without approximations to the number of atomic degrees of freedom or the maximal degree of their coupling. In particular, we studied the A_{1g} phonon decay time and time evolution of the atomic paths on laser-excited potential energy surfaces.

Twenty years ago it has been experimentally observed [9, 100] that the decay time of 2.9 ps for coherently excited A_{1g} phonon in Sb at room temperature during the first 5 ps after femtosecond-laser excitation and for further oscillations the decay time surprisingly increases. The precise value of the decay time after 5 ps of femtosecond-laser excitation has not been reported. From our molecular dynamics study we observed only one decay time upto 10 ps after laser excitation, which is in agreement with first decay time of Ref. [9, 100].

Misochko *et al.* [104, 105] observed that in Bi after a few ps of laser excitation the coherent phonon oscillations die out and then revive, and proposed that such collapse-revival is the direct consequence of the spatially inhomogeneous electronic softening. Later Diakhate *et al.* [106] demonstrated that for large systems the oscillation approached the classical limit without collapse-revival. In agreement, in the present study we found that the average over a sufficient number of runs gives a good statistics and the collapse-revival was not observed in any of the system sizes.

Atomic motion can be studied from the time-dependent variance of the atomic displacement from which we notice that N = 72 already gives a sufficient sampling of all phonon modes in the first Brillouin zone. Previous studies on Bi [11] shows that, even if the pure dephasing contributes to the decay process, the decay of the coherent phonons are dominated by anharmonic coupling (energy relaxation). Since Sb is isostructural to Bi and As, these elements can exhibit similar electronic and lattice properties under femtosecond-laser excitation.

In conclusion, we have developed a thermodynamical model to simulate the time evolution of the A_{1g} phonon coordinate following the arrival of the laser pulse of a given fluence on Sb. We show that intense ultrashort laser pulses not only induce coherent phonons in Sb but also interactions between them. The phonon-phonon interaction is strongly dependent on the laser fluence. We have analyzed the coherent phonon dynamics on supercells having upto 192 atoms for a particular laser excitation and on 72 atom supercell for different laser fluences near and below the structural phase transition. We found that our results are in perfect agreement with and can be helpful to understand previous experimental results [9, 100]. We also studied the changes in the potential energy surface after femtosecond-laser excitation and found laser-induced phonon softening in Sb. Due to rapid improvements in laser technology and the ability to produce very short ($\sim$ 10 - 100 fs) and powerful ($\sim$ 1 - 10 mJ/cm^2) laser pulses, there is an increasing need for theoretical insight into the interactions for such laser pulses with matter. For the duration of the application of such a laser pulse, its electromagnetic field generates a coherent superposition of excited electron and hole states in the material.

Our work demonstrates that the fast equilibrium dynamics of the laser excited nonequilibrium carrier population can induce a significant structural response in crystalline solids. The magnitude and dynamics of this effects depends on the electronic structure and electron-phonon interactions of the material.

CHAPTER 6

Conclusion and outlook

In this thesis we have discussed theoretical models to describe the ultrafast structural response of different solids to an intense femtosecond-laser excitation on the basis of density functional theory. Our approaches provide theoretical frameworks for the treatment of non-equilibrium states in solids and the calculation of the time-dependent potential energy surfaces. We have studied the structural responses of copper, silver and antimony upon femtosecond-laser excitation at different laser fluences. Quantitative agreements have been found with the existing experimental and theoretical results and predictions have also been made.

The interaction of an intense femtosecond-laser pulse with solids has remained an active area of research. Laser-induced structural responses on variety of materials are addressed in this thesis. In this final chapter, we review some of the key conclusions of this thesis and briefly discuss areas where further work is needed. The following are the main results obtained:

- **Warm dense noble metals:** We have theoretically studied the changes in the bonding properties of transient, exotic state of highly ionized warm dense noble metals, in particular copper and silver by performing electronic-temperature-dependent density functional theory calculations. The electronic and phonon densities of states and band structures are studied for cold and hot electronic states of noble metals in the presence of core hole. We found that the system gains extra stability in warm dense regime due to the hardening of potential energy surface. Such extreme hardening of phonon modes cause the relaxation processes of warm dense noble metals to be faster than the theoretically expected values. We also found that in such a system there is no indication of any phonon mode instability, which indicates that the system relaxes thermally into a plasma state.

- **Vacuum phonon squeezing:** The fundamental quantum mechanical effect called vacuum phonon squeezing as well as the conditions under which a significant squeezing effect can be obtained were studied using density functional theory. We found that at low electronic excitation the phonon hardening in noble metals is due to the overlapping of excited valence s electrons. We also found that vacuum squeezed states can be produced in copper and silver at various points of the Brillouin zone and we analyzed the momentum-resolved squeezing factors for both copper and silver at the X- and L-point longitudinal mode. The maximal squeezing factors obtained for copper (0.0019) and silver (0.0014) at L-point longitudinal mode are three orders of magnitude greater than the ones previously obtained in $KTaO_3$ (10^{-6}) [4]. We have indicated, how measuring vacuum phonon squeezing in real space through momentum- and time-resolved x-ray scattering would provide direct evidence of bond hardening in noble metals.

- **Coherent phonon dynamics:** We have developed a thermodynamical model to simulate the time evolution of the coherent A_{1g} phonon coordinate following the arrival of the laser pulse of a given fluence on antimony. We shown that intense ultrashort laser pulses not only induce coherent phonons in antimony but also interactions between them. The phonon-phonon interaction is strongly dependent on the laser fluence. We have studied the phonon dynamics of antimony in the low fluence regime from molecular dynamics simulations using our in-house density functional theory code CHIVES [97]. We computed the A_{1g} phonon mode decay constant for different laser fluences in supercells upto 192 atoms. We have analyzed the temperature-dependent decay constant and decay channel(s) of A_{1g} phonon mode using the 72 atom supercell of antimony. The decay channel(s) were studied from phonon-phonon coupling.

Our work demonstrates that the fast equilibration dynamics of the laser excited nonequilibrium carrier population can induce a significant structural response in crystalline solids. The future of this work lies in developing the code CHIVES, the most efficient and fast basis of any future density functional theory calculation for a precise description of the nonequlibrium states of materials. Then to study the structural dynamics after different excitation fluences on large material classes (semiconductors, insulators, metals, rare earth metals) using the codes WIEN2k and CHIVES. The following are some specific problems to study:

- **Warm dense aluminum and life time of core hole:** In nearly free-electron metals like aluminum, the electron density of states and lattice stability appears to be mostly unaffected by the electronic excitation. It is suggested that such solids show very low electron-phonon coupling in the warm dense regime compared to that of warm dense noble metals [60]. Warm dense aluminum is expected

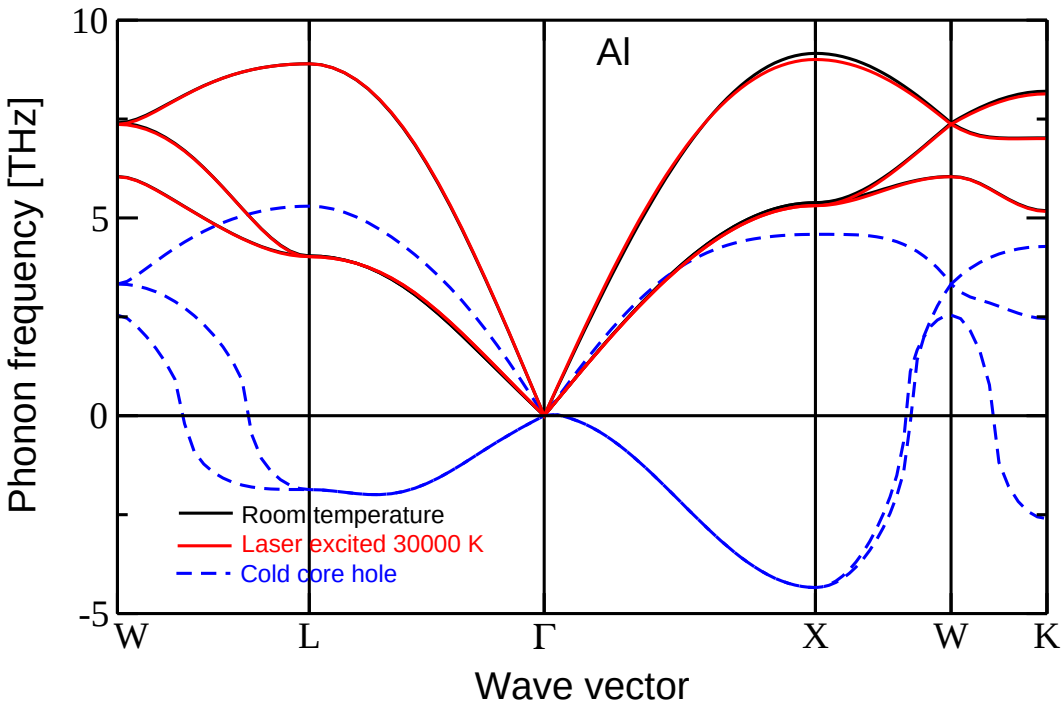

Figure 6.1: The phonon dispersion spectra of aluminum. Black solid curves show at room temperature, red solid curves at T_e = 30,000 K without core hole and blue dashed curves represent the state with one core hole per atom at room temperature.

to relax via nonthermal melting on a picosecond time scale after the excitation. It will be very interesting to study the structural dynamics of warm dense aluminum: Bonding properties, relaxation process, decay time of core holes, etc., because to the best of our knowledge the above mentioned properties are not yet studied in a free-electron like metals. As a preliminary step towards this work, we have analyzed the phonon dispersion spectra of aluminum (see figure 6.1) at laser-excited (T_e = 30,000 K) and core-hole excited states (1 core-hole per atom). From figure 6.1 it clear that in the electronic excited state, even at T_e = 30,000 K, the phonon modes are effected negligibly small (red solid curves in figure 6.1), but there is a significant effect due to the presence of core hole. The system becomes unstable in the core hole state. This is an indication of warm dense aluminum relaxes through nonthermal melting.

- **Vacuum squeezing factor in gold and to find other materials with improved squeezing factor:** Based on the chemical and physical similarities of noble metals, we expect that vacuum phonon squeezing could also be achieved in gold. From the trend of maximal squeezing factor we obtained in copper and silver at L-point longitudinal mode, we expect that the maximal squeezing will be less in gold than in copper and silver (see figure 6.2). It will be very interesting

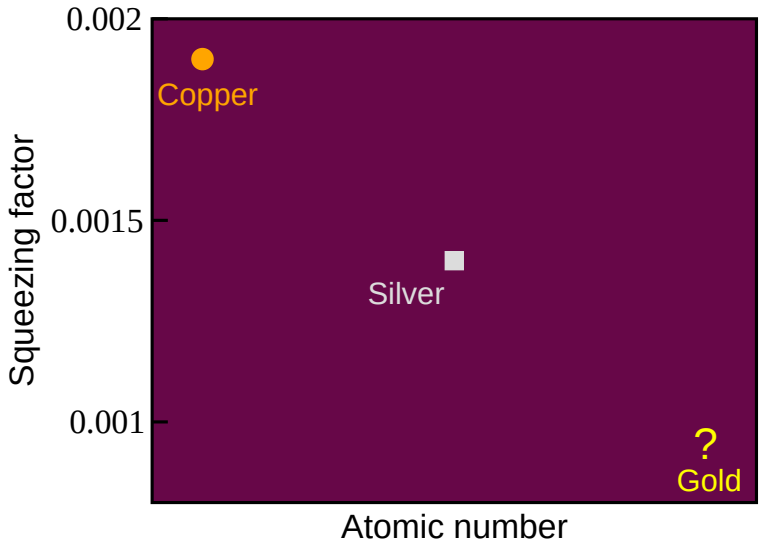

Figure 6.2: Maximum obtained squeezing factor for noble metals at L-point longitudinal mode.

to find the maximal squeezing factor for gold by studying various points in the Brillouin zone.

From our studies on copper and silver we found that bond hardening is responsible for the generation of vacuum phonon squeezed states and electron-phonon coupling will control the size of squeezing effect. Our maximum predicted vacuum phonon squeezing factor is of the order of 10^{-3}. One could find materials with greater bond hardening or a smaller electron-phonon coupling factor to improve this result by one or two orders of magnitude. For example, we expect that alkali metals show greater bond hardening because their valence band contains only s electrons. From the present research work we found that at low fluence excitation s electrons are responsible for bond hardening in noble metals.

- **Solid-solid structural phase transition and nonthermal melting in antimony:** The study of ultrafast reversible and irreversible structural changes has attracted attention in the last years, mainly due to recent advances in time-resolved x-ray and electron diffraction techniques [107]. Sb shows a sequence of phase transitions as a function of pressure. At low temperatures and normal pressure, Sb crystallizes in the Peierls distorted A7 structure, at 8.6 GPa there is a transition to a complex host-guest structure through simple cubic structure and at 28 Gpa, Sb assumes the body-centerd cubic structure [108].

  Different pump-prob experimentals have been performed on antimony: The excitation of A_{1g} and E_g coherent phonons have been confirmed [109,110]. From one of those studies, the existence of a laser-induced solid-solid transition to a so far unknown phase has been suggested [110]. In order to study possible phase tran-

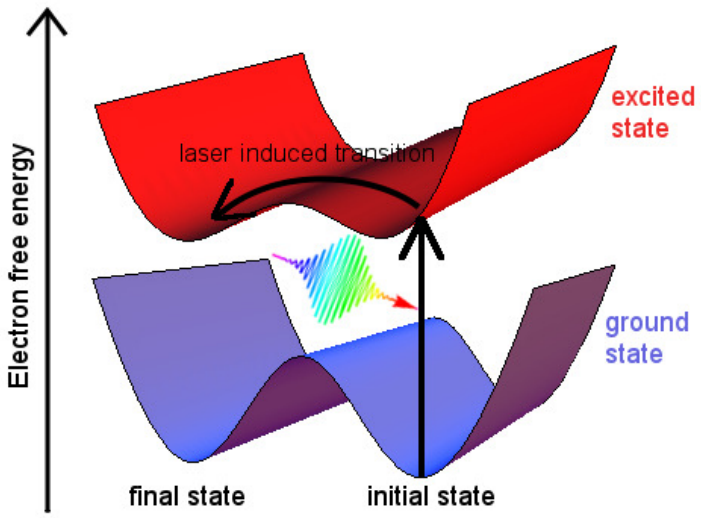

Figure 6.3: Illustration of the mechanism of an ultrafast phase transition through laser-induced modification of potential energy surfaces.

sitions that can be induced by a femtosecond-laser pulse far out of equilibrium, we intended to perform molecular dynamics simulations and to compare the free energies of antimony in the $A7$, simple cubic, host-guest, and bcc structures. In Sb we expect that a femtosecond-laser pulse can undo the Peierls distortion, while its structure transform from $A7$ to complex host-guest structure. The phase transition should occur to the undistorted phase on a timescale faster than the time required for electron-phonon thermalization. Characteristics of this phase transition is that the value of internal coordinate increases towards 0.25. By performing molecular dynamics simulations using CHIVES, one can study the laser-induced structural effects, such as, phonon squeezing, nonthermal melting, laser-induced undoing of the Peierls-Jones distortion, etc. Thus, antimony continues a fascinating solid, in which all so far known laser-induced nonthermal structural effects are expected to occur.

The mechanism of laser-induced ultrafast solid-to-solid phase transitions is visualized in figure 6.3. Two different structural phases of a given material in thermodynamical equilibrium correspond to two minima of the potential energy surface. A thermal transition between both minima is an extremely slow process, because a high potential barrier has to be overcome. However, a femtosecond-laser ex-

citation (i.e., an almost instantaneous electron heating) can effect both minima differently, like it is sketched in figure 6.3. Instance, the minimum corresponding to the initial state might become unstable at high electron temperatures, while the other minimum is less affected. Consequently a very fast phase transition takes place.

The study of the interaction of intense laser pulses with solids will undoubtedly continue for time. It is clear that for reasons related to new technological applications, study of laser-matter interaction remains an active and exciting research subject for both theoreticians and experimentalists.

Appendices

APPENDIX A

A.1 Two-center overlap integrals

Two-center overlap integrals over unnormalized cartesian Gaussian function [25,26] are of the form:

$$\langle a \mid b \rangle = \int_{-\infty}^{+\infty} \phi(r, \alpha, a, A)\ \phi(r, \beta, b, B)\ dr \tag{A.1}$$

and are located at A and B having orbital exponents α and β respectively. We first separate the integral into its orthogonal components:

$$S = E_{AB}\ S_x(a_x, b_x)\ S_y(a_y, b_y)\ S_z(a_z, b_z), \tag{A.2}$$

where the notation $S_x(a_x, b_x)$ expresses its functional dependence on the cartesian angular components. The x component can be expressed as,

$$S_x(a_x, b_x) = \int_{-\infty}^{+\infty} (x - A_x)^{a_x}\ (x - B_x)^{b_x}\ e^{-(\alpha+\beta)(x-P_x)^2}\ dx. \tag{A.3}$$

where $E_{AB} = e^{-\frac{\alpha\beta}{\alpha+\beta}|A-B|^2}$ and $P_x = \frac{\alpha A_x + \beta B_x}{\alpha+\beta}$.
Using a binomial expansion in the polynomial part,

$$(x-A_x)^{a_x}\ (x-B_x)^{b_x} = \sum_{i=0}^{a_x}\sum_{j=0}^{b_x} \binom{a_x}{i}\binom{b_x}{i}(x-P_x)^{i+j}(P_x-A_x)^{a_x-i}(P_x-B_x)^{b_x-j}, \tag{A.4}$$

which gives:

$$\begin{aligned} S_x(a_x, b_x) = \sum_{i=0}^{a_x}\sum_{j=0}^{b_x} \binom{a_x}{i}\binom{b_x}{i}(P_x - A_x)^{a_x-i}\ (P_x - B_x)^{b_x-j} \\ \int_{-\infty}^{+\infty} (x - P_x)^{i+j}\ e^{-(\alpha+\beta)(x-P_x)^2}\ dx. \end{aligned} \tag{A.5}$$

Odd values of $i + j$ results in odd function whose integral part will vanish. For even values of $i + j$, the solution for integral part is,

$$\int_{-\infty}^{+\infty} (x - P_x)^{i+j}\ e^{-(\alpha+\beta)(x-P_x)^2}\ dx = \left(\frac{\pi}{\alpha+\beta}\right)^{\frac{1}{2}} \left(\frac{(i+j-1)!!}{[2(\alpha+\beta)]^{\frac{i+j}{2}}}\right). \tag{A.6}$$

In such case $S_x(a_x, b_x)$ becomes,

$$\begin{aligned} S_x(a_x, b_x) = \left(\frac{\pi}{\alpha+\beta}\right)^{\frac{1}{2}} \sum_{i=0}^{a_x} \sum_{j=0}^{b_x} \binom{a_x}{i} \binom{b_x}{i} \\ (P_x - A_x)^{a_x - i}\ (P_x - B_x)^{b_x - j} \left(\frac{(i+j-1)!!}{[2(\alpha+\beta)]^{\frac{i+j}{2}}}\right). \end{aligned} \tag{A.7}$$

One should keep in mind that the summation term exists only for the even values of $i+j$. equation A.7 can be written as a generalized form for x, y and z components. However, further reductions in the number of operations can be obtained using a recurrence relation. Recurrence relations let us efficiently calculate the overlap integrals of higher angular values from previously obtained results with lower angular values.

A.2 Recurrence relations

One of the properties of cartesian Gaussian function is: The derivative of a Gaussian function can be expressed as a sum of Gaussians of higher and lower angular values (see Section 2.6.2),

$$\phi(r, \alpha, a+1, A) = \frac{1}{2\alpha}\ \frac{\partial}{\partial A}\phi(r, \alpha, a, A) + \frac{N(a)}{2\alpha}\ \phi(r, \alpha, a-1, A). \tag{A.8}$$

In the previous section we derived two expressions for $S_x(a_x, b_x)$, equation A.3 and equation A.7. To get the recurrence relation for x component, we have to compare the first derivative of $S_x(a_x, b_x)$ from equation A.3 and equation A.7.

- Derivative from equation A.3:

$$\begin{aligned} \frac{\partial}{\partial A_x} S_x(a_x, b_x) = \int_{-\infty}^{+\infty} (x - B_x)^{b_x} \frac{\partial}{\partial A_x} \left[(x - A_x)^{a_x}\ e^{-(\alpha+\beta)(x-P_x)^2}\right] dx \\ \Rightarrow -a_x S_x(a_x - 1, b_x) + 2\alpha(x - P_x) S_x(a_x, b_x). \end{aligned} \tag{A.9}$$

  equation A.9 $\pm\ 2\alpha\ S_x(a_x, b_x)$ gives:

$$\frac{\partial}{\partial A_x} S_x(a_x, b_x) = -a_x S_x(a_x - 1, b_x) + 2\alpha S_x(a_x + 1, b_x) + 2\alpha(A_x - P_x) S_x(a_x, b_x). \tag{A.10}$$

- Derivative from equation A.7:

$$\frac{\partial}{\partial A_x} S_x(a_x, b_x) = K \; \frac{\partial}{\partial A_x} \Big[(P_x - A_x)^{a_x - i} \; (P_x - B_x)^{b_x - j} \Big], \tag{A.11}$$

where $K = \left(\frac{\pi}{\alpha+\beta} \right)^{\frac{1}{2}} \sum_{i=0}^{a_x} \sum_{j=0}^{b_x} \binom{a_x}{i} \binom{b_x}{i} \left(\frac{(i+j-1)!!}{[2(\alpha+\beta)]^{\frac{i+j}{2}}} \right)$ is a constant. For simplicity of further derivation, we can assume $i = j = 0$ in equation A.11.
Therefore,

$$\begin{aligned} \frac{\partial}{\partial A_x} \Big[(P_x - A_x)^{a_x} \; (P_x - B_x)^{b_x} \Big] = & -a_x \; \frac{\beta}{\alpha + \beta} \; S_x(a_x - 1, b_x) \\ & + b_x \; \frac{\alpha}{\alpha + \beta} \; S_x(a_x, b_x - 1). \end{aligned} \tag{A.12}$$

By comparing equation A.10 and equation A.12, one can write the recurrence relation for x component as the following:

$$\begin{aligned} S_x(a_x + 1, b_x) = (P_x - A_x) S_x(a_x, b_x) & + \frac{a_x}{2(\alpha + \beta)} S_x(a_x - 1, b_x) \\ & + \frac{b_x}{2(\alpha + \beta)} S_x(a_x, b_x - 1). \end{aligned} \tag{A.13}$$

The generalized form of recurrence relation $\langle a + 1 \mid b \rangle$ for all three components x, y and z, which will be used to generate the two-center overlap integrals over s, p and d cartesian Gaussian functions is given by

$$\langle a + 1 \mid b \rangle = (P - A) \; \langle a \mid b \rangle + \frac{N(a)}{2(\alpha + \beta)} \; \langle a - 1 \mid b \rangle + \frac{N(b)}{2(\alpha + \beta)} \; \langle a \mid b - 1 \rangle. \tag{A.14}$$

The overlap integral between an orbital ($a = s, p, d$, etc) centered at A with the projector of another orbital ($b = s, p, d$, etc) centered at B can be calculated by

$$\langle a \mid r^2 b \rangle = \frac{\partial}{\partial \beta} \big(\langle a \mid b \rangle \big) \tag{A.15}$$

The force integrals can be calculated as

$$\nabla \; \langle a \mid b \rangle = \frac{\partial}{\partial A} \big(\langle a \mid b \rangle \big) \tag{A.16}$$

Example: The overlap integral between two s ($a = b = 0$) orbitals centered at A and B is

$$\begin{aligned} \langle s \mid s \rangle &= \int_{-\infty}^{+\infty} \; \phi(r, \alpha, 0, A) \; \phi(r, \beta, 0, B) \; dr, \\ &\Rightarrow \Big(\frac{\pi}{\alpha + \beta} \Big)^{\frac{3}{2}} \; \exp\Big[- \frac{\alpha\beta}{\alpha + \beta} \mid A - B \mid^2 \Big]. \end{aligned} \tag{A.17}$$

The overlap integral between s orbital centered at A and the projector of another s orbital centered at B

$$\begin{aligned} \langle s \mid r^2 s\rangle &= \frac{\partial}{\partial\beta}\big(\langle s \mid s\rangle\big), \\ &\Rightarrow \Big[\frac{3}{2(\alpha+\beta)} + \frac{\alpha^2(A-B)^2}{(\alpha+\beta)^2}\Big]\ \langle s \mid s\rangle. \end{aligned} \tag{A.18}$$

A.3 The expressions implemented in CHIVES

From the recurrence relation $\langle a+1 \mid b\rangle$ for two-center overlap integrals [equation A.14] one can obtain the functional forms of overlap integrals for s, p and d orbitals, which is tabluted in Table A.I. The expressions for overlap integrals between orbital and projectors are derived from equation A.15 (see Table A.II). The force intergrals between the orbitals (Table A.III) and between orbitals and projectors (Table A.IV) were formulated from equation A.16 and are implemented in our code CHIVES.

$\langle s \mid s\rangle$	$\left(\frac{\pi}{\alpha+\beta}\right)^{\frac{3}{2}}\ \exp\Big[-\frac{\alpha\beta}{\alpha+\beta}\mid A-B\mid^2\Big]$
$\langle s \mid p_j\rangle$	$(P_j - B_j)\ \langle s \mid s\rangle$
$\langle s \mid d_{ij}\rangle$	$(P_i - B_i)\ \langle s \mid p_j\rangle + \frac{\delta_{ij}}{2(\alpha+\beta)}\ \langle s \mid s\rangle$
$\langle p_i \mid s\rangle$	$(P_i - A_i)\ \langle s \mid s\rangle$
$\langle p_i \mid p_j\rangle$	$(P_i - A_i)\ \langle s \mid p_j\rangle + \frac{\delta_{ij}}{2(\alpha+\beta)}\ \langle s \mid s\rangle$
$\langle p_i \mid d_{jk}\rangle$	$(P_k - B_k)\ \langle p_i \mid p_j\rangle + \frac{\delta_{jk}}{2(\alpha+\beta)}\ \langle p_i \mid s\rangle + \frac{\delta_{ik}}{2(\alpha+\beta)}\ \langle s \mid p_j\rangle$
$\langle d_{ij} \mid s\rangle$	$(P_j - A_j)\ \langle p_i \mid s\rangle + \frac{\delta_{ij}}{2(\alpha+\beta)}\ \langle s \mid s\rangle$
$\langle d_{ij} \mid p_k\rangle$	$(P_j - A_j)\ \langle p_i \mid p_k\rangle + \delta_{jk}\ \langle p_i \mid s\rangle$
$\langle d_{ij} \mid d_{kl}\rangle$	$(P_i - A_i)\ \langle p_j \mid d_{kl}\rangle + \frac{\delta_{ik}}{2(\alpha+\beta)}\ \langle p_j \mid p_l\rangle + \frac{\delta_{il}}{2(\alpha+\beta)}\ \langle p_j \mid p_k\rangle + \frac{\delta_{ij}}{2(\alpha+\beta)}\ \langle s \mid d_{kl}\rangle$

Table A.I: Two-center overlap integrals over s, p and d cartesian Gaussian functions.

$\langle s \mid r^2 s\rangle$	$\left[\frac{3}{2(\alpha+\beta)} + \frac{\alpha^2(A-B)^2}{(\alpha+\beta)^2}\right] \langle s \mid s\rangle$
$\langle s \mid r^4 s\rangle$	$\left[\frac{3}{2(\alpha+\beta)} + \frac{\alpha^2(A-B)^2}{(\alpha+\beta)^2}\right] \left(\langle s \mid r^2 s\rangle + \frac{\langle s\mid s\rangle}{\alpha+\beta}\right)$
$\langle p_i \mid r^2 s\rangle$	$(P_i - A_i)\ \langle s \mid r^2 s\rangle + \frac{(P_i-B_i)}{\alpha+\beta}\ \langle s \mid s\rangle$
$\langle p_i \mid r^4 s\rangle$	$(P_i - A_i)\ \langle s \mid r^4 s\rangle + 2\frac{(P_i-B_i)}{\alpha+\beta}\ \left[\langle s \mid r^2 s\rangle + \frac{\langle s\mid s\rangle}{\alpha+\beta}\right]$
$\langle d_{ij} \mid r^2 s\rangle$	$(P_j - A_j)\ \langle p_i \mid r^2 s\rangle + \frac{(P_j-B_j)}{\alpha+\beta}\ \langle p_i \mid s\rangle$
$\langle d_{ij} \mid r^4 s\rangle$	$(P_j - A_j)\ \langle p_i \mid r^4 s\rangle + 2\frac{(P_j-B_j)}{\alpha+\beta}\ \left[\langle p_i \mid r^2 s\rangle + \frac{\langle p_i\mid s\rangle}{\alpha+\beta}\right]$
$\langle s \mid r^2 p_j\rangle$	$(P_j - B_j)\ \left[\langle s \mid r^2 s\rangle + \frac{\langle s\mid s\rangle}{\alpha+\beta}\right]$
$\langle p_i \mid r^2 p_j\rangle$	$(P_i - A_i)\ \langle s \mid r^2 p_j\rangle + \frac{(P_i-B_i)}{\alpha+\beta}\ \langle s \mid p_j\rangle + \frac{\delta_{ij}}{2(\alpha+\beta)}\ \left[\langle s \mid r^2 s\rangle + \frac{\langle s\mid s\rangle}{\alpha+\beta}\right]$
$\langle d_{ij} \mid r^2 p_k\rangle$	$(P_j - A_j)\ \langle p_i \mid r^2 p_k\rangle + \frac{(P_j-B_j)}{\alpha+\beta}\ \langle p_i \mid p_k\rangle + \frac{\delta_{ik}}{2(\alpha+\beta)}\ \left[\langle p_i \mid r^2 s\rangle + \frac{\langle p_i\mid s\rangle}{\alpha+\beta}\right]$

Table A.II: The overlap integrals between orbitals and projectors for s, p and d orbitals.

$\nabla_i \langle s \mid s \rangle$	$2\alpha \langle p_i \mid s \rangle$
$\nabla_i \langle s \mid p_j \rangle$	$(P_j - B_j) \nabla_i \langle s \mid s \rangle + \delta_{ij} \frac{\alpha}{\alpha+\beta} \langle s \mid s \rangle$
$\nabla_i \langle s \mid d_{jk} \rangle$	$(P_j - A_j) \nabla_i \langle s \mid p_k \rangle + \delta_{ij} \frac{\alpha}{\alpha+\beta} \langle s \mid p_k \rangle$
$\nabla_i \langle p_j \mid s \rangle$	$(P_j - A_j) \nabla_i \langle s \mid s \rangle - \delta_{ij} \frac{\beta}{\alpha+\beta} \langle s \mid s \rangle$
$\nabla_i \langle p_j \mid p_k \rangle$	$(P_j - A_j) \nabla_i \langle s \mid p_k \rangle - \delta_{ij} \frac{\beta}{\alpha+\beta} \langle s \mid p_k \rangle + \frac{\delta_{jk}}{2(\alpha+\beta)} \nabla_i \langle s \mid s \rangle$
$\nabla_i \langle p_j \mid d_{kl} \rangle$	$(P_j - A_j) \nabla_i \langle s \mid d_{kl} \rangle - \frac{\delta_{ij}}{2(\alpha+\beta)} \left[2\langle s \mid d_{kl} \rangle + \nabla_i \langle s \mid p_l \rangle \right] + \frac{\delta_{jl}}{2(\alpha+\beta)} \langle s \mid p_k \rangle$
$\nabla_i \langle d_{jk} \mid s \rangle$	$(P_j - A_j) \nabla_i \langle p_k \mid s \rangle - \delta_{ij} \frac{\beta}{\alpha+\beta} \langle p_k \mid s \rangle + \frac{\delta_{ij}}{2(\alpha+\beta)} \nabla_i \langle s \mid s \rangle$
$\nabla_i \langle d_{jk} \mid p_l \rangle$	$(P_k - A_k) \nabla_i \langle p_j \mid p_l \rangle - \delta_{ik} \frac{\beta}{\alpha+\beta} \langle p_j \mid p_l \rangle - \delta_{kl} \frac{\beta}{2\alpha(\alpha+\beta)} \nabla_i \langle s \mid p_j \rangle$
$\nabla_i \langle d_{jk} \mid d_{lm} \rangle$	$(P_j - A_j) \nabla_i \langle p_k \mid d_{lm} \rangle - \delta_{ij} \frac{\beta}{\alpha+\beta} \langle p_k \mid d_{lm} \rangle + \frac{\delta_{jl}}{2(\alpha+\beta)} \nabla_i \langle p_k \mid p_m \rangle + \frac{\delta_{jm}}{2(\alpha+\beta)} \nabla_i \langle p_k \mid p_l \rangle$

Table A.III: Force integrals for s, p and d orbitals.

$\nabla_i \langle s \mid r^2 s\rangle$	$\left[\frac{3}{2(\alpha+\beta)} + \frac{\alpha^2(A-B)^2}{(\alpha+\beta)^2}\right] \nabla_i \langle s \mid s\rangle + \frac{2\alpha^2(A-B)}{(\alpha+\beta)^2} \langle s \mid s\rangle$
$\nabla_i \langle s \mid r^4 s\rangle$	$\left[\frac{3}{2(\alpha+\beta)} + \frac{\alpha^2(A-B)^2}{(\alpha+\beta)^2}\right] \nabla_i \langle s \mid r^2 s\rangle + \left[\frac{3}{2(\alpha+\beta)} + \frac{2\alpha^2(A-B)^2}{(\alpha+\beta)^2}\right] \frac{\nabla_i \langle s\|s\rangle}{\alpha+\beta}$ $+\frac{2\alpha^2(A-B)}{(\alpha+\beta)^2} \left[\langle s \mid r^2 s\rangle + \frac{2\langle s\|s\rangle}{\alpha+\beta}\right]$
$\nabla_i \langle p_j \mid r^2 s\rangle$	$(P_j - A_j) \nabla_i \langle s \mid r^2 s\rangle + \frac{(P_j-B_j)}{\alpha+\beta} \nabla_i \langle s \mid s\rangle + \frac{\delta_{ij}}{A_j-B_j}\langle p_j \mid r^2 s\rangle$
$\nabla_i \langle p_j \mid r^4 s\rangle$	$(P_j - A_j) \nabla_i \langle s \mid r^2 s\rangle + \frac{2(P_j-B_j)}{\alpha+\beta} \left[\nabla_i \langle s \mid r^2 s\rangle + \frac{\nabla_i \langle s\|s\rangle}{\alpha+\beta}\right]$ $+\frac{\delta_{ij}}{A_j-B_j}\langle p_j \mid r^2 s\rangle$
$\nabla_i \langle d_{jk} \mid r^2 s\rangle$	$(P_j - A_j) \nabla_i \langle p_k \mid r^2 s\rangle + \frac{(P_j-B_j)}{\alpha+\beta} \nabla_i \langle p_k \mid s\rangle + \frac{\delta_{ij}}{A_j-B_j}\langle d_{jk} \mid r^2 s\rangle$
$\nabla_i \langle d_{jk} \mid r^4 s\rangle$	$(P_j - A_j) \nabla_i \langle p_k \mid r^4 s\rangle + \frac{2(P_j-B_j)}{\alpha+\beta} \left[\nabla_i \langle p_k \mid r^2 s\rangle + \frac{\nabla_i \langle p_k\|s\rangle}{\alpha+\beta}\right]$ $+\frac{\delta_{ij}}{A_j-B_j}\langle d_{jk} \mid r^4 s\rangle$
$\nabla_i \langle s \mid r^2 p_j\rangle$	$(P_j - B_j) \nabla_i \langle s \mid r^2 s\rangle + \frac{\nabla_i \langle s\|p_j\rangle}{\alpha+\beta} + \delta_{ij}\frac{\alpha}{\alpha+\beta} \langle s \mid r^2 s\rangle$
$\nabla_i \langle p_j \mid r^2 p_k\rangle$	$(P_j - A_j) \nabla_i \langle s \mid r^2 p_k\rangle + \frac{P_j-B_j}{\alpha+\beta} \nabla_i \langle s \mid p_k\rangle + \frac{\delta_{ij}}{\alpha+\beta} \left[-\beta\langle s \mid r^2 p_k\rangle$ $+\frac{\alpha}{\alpha+\beta}\langle s \mid p_k\rangle\right]+\frac{\delta_{jk}}{2(\alpha+\beta)} \left[\nabla_i \langle s \mid r^2 s\rangle + \frac{\langle s\|s\rangle}{\alpha+\beta}\right]$
$\nabla_i \langle d_{jk} \mid r^2 p_l\rangle$	$(P_j - A_j) \nabla_i \langle p_k \mid r^2 p_l\rangle + \frac{P_j-B_j}{\alpha+\beta} \nabla_i \langle p_k \mid p_l\rangle + \frac{\delta_{ij}}{\alpha+\beta} \left[-\beta\langle p_k \mid r^2 p_l\rangle$ $+\frac{\alpha}{\alpha+\beta}\langle p_k \mid p_l\rangle\right]+\frac{\delta_{jl}}{2(\alpha+\beta)} \left[-\frac{\beta}{\alpha}\nabla_i \langle s \mid r^2 p_k\rangle + \frac{\langle s\|p_k\rangle}{\alpha+\beta}\right]$

Table A.IV: The force integrals between orbital and projectors for s, p and d orbitals.

APPENDIX B

B.1 Potential energy of phonon-phonon interaction

Consider a crystal formed by N number of atoms having mass M and the equilibrium position of the atoms is at z. But the actual position of the atoms is $z^{''} = z + u$, where u is a shift from the equilibrium position and the atoms oscillate around $z^{''}$.

The interaction potential among the atoms can be expressed as a function of the shift u:

$$V(z^{''}) = V_0(z^{''}) + \sum_{i=1}^{3N-1} \frac{1}{2}\, M\omega_i^2 u_i^2, \tag{B.1}$$

where ω is the phonon frequency around the actual position of the atoms $z^{''}$.

One can expand equation B.1 using Taylor's series,

$$V(z^{''}) = V_0(z^{''}) + \sum_{i=1}^{3N-1} \frac{1}{2}\, M\omega_i^{(0)^2}\, u_i^2 + \sum_{i=1}^{3N-1} \frac{1}{2}\, M\, \frac{\partial(\omega_i^2)}{\partial z^{''}}\bigg|_{z^{''}=z} (z^{''} - z)\, u_i^2, \tag{B.2}$$

where $\omega^{(0)}$ is the phonon frequency at equilibrium position z.

The total force exerted on the system due to shift in equilibrium position can be calculated as,

$$F_{z^{''}} = -\frac{\partial V}{\partial z^{''}}. \tag{B.3}$$

From equation B.1, the expression for force becomes,

$$F_{z^{''}} = -\frac{\partial V_0(z^{''})}{\partial z^{''}} - \sum_{i=1}^{3N-1} \frac{1}{2}\, M \frac{\partial(\omega_i^2)}{\partial z^{''}}\bigg|_{z^{''}=z} u_i^2 \tag{B.4}$$

$$= -\frac{\partial V_0(z^{''})}{\partial z^{''}} - \sum_{i=1}^{3N-1} \frac{1}{2}\, k_B T_l\, \frac{1}{(\omega_i^2)}\, \frac{\partial(\omega_i^2)}{\partial z^{''}}\bigg|_{z^{''}=z} \tag{B.5}$$

$$= -\frac{\partial V_0(z^{''})}{\partial z^{''}} - \frac{1}{2}\, k_B T_l \sum_{i=1}^{3N-1} \frac{\partial \ln(\omega_i^2)}{\partial z^{''}}\bigg|_{z^{''}=z} \tag{B.6}$$

where k_B is the Boltzmann constant and T_l is the lattice temperature.

When all atoms are at equilibrium, the force of the system must be zero, since there can be no net force at equilibrium. So one can neglect the term $\frac{1}{2}\, M{\omega_i^{(0)}}^2\, u_i^2$ in equation B.2. From equation B.2 and B.6, one can write the expression for interaction potential as the following:

$$V(z^{''}) = V_0(z^{''}) + \underbrace{\frac{1}{2}\, k_B T_l \sum_{i=1}^{3N-1} \frac{1}{(\omega_i^2)}\, \frac{\partial(\omega_i^2)}{\partial z^{''}}\bigg|_{z^{''}=z} (z^{''} - z)}_{V^{ph-ph}}. \tag{B.7}$$

The second term on right-hand side of equation B.7 is the phonon-phonon coupling potential V^{ph-ph},

$$dV^{ph-ph} = \frac{1}{2}\, k_B T_l \sum_{i=4}^{3N-1} \frac{1}{(\omega_i^2)}\, \frac{\partial(\omega_i^2)}{\partial(z^{''})}\, dz^{''}, \tag{B.8}$$

by integrating with respect to $z^{''}$,

$$V^{ph-ph} = \frac{1}{2}\, k_B T_l \sum_{i=4}^{3N-1} \ln(\omega_i^2) \;+\; C, \tag{B.9}$$

where C is the integration constant and the integer i starts from four, since by omitting three translational modes ($\omega = 0$) and the A_{1g} mode.

Bibliography

[1] B. I. Cho, K. Engelhorn, A. A. Correa, T. Ogitsu, C. P. Weber, H. J. Lee, J. Feng, P. A. Ni, Y. Ping, A. J. Nelson, D. Prendergast, R. W. Lee, R. W. Falcone, and P. A. Heimann, Phys. Rev. Lett. **106**, 167601 (2011).

[2] Z. Lin, L. V. Zhigilei, and V. Celli, Phys. Rev. B **77**, 075133 (2008).

[3] X. Hu and F. Nori, Phys. Rev. Lett. **79**, 4605 (1997).

[4] G. A. Garrett, A. G. Rojo, A. K. Sood, J. F. Whitaker, and R. Merlin, Science **275**, 1638 (1997).

[5] S. L. Johnson, P. Beaud, E. Vorobeva, C. J. Milne, É. D. Murray, S. Fahy, and G. Ingold, Phys. Rev. Lett. **102**, 175503 (2009).

[6] É. D. Murray, S. Fahy, D. Prendergast, T. Ogitsu, D. M. Fritz, and D. A. Reis, Phys. Rev. B **75**, 184301 (2007).

[7] E. S. Zijlstra, J. Walkenhorst, and M. E. Garcia, Phys. Rev. Lett. **101**, 135701 (2008).

[8] T. K. Cheng, S. D. Brorson, A. S. Kazeroonian, J. S. Moodera, G. Dresselhaus, M. S. Dresselhaus, and E. P. Ippen, Appl. Phys. Lett. **57**, 1004 (1990).

[9] H. J. Zeiger, J. Vidal, T. K. Cheng, E. P. Ippen, G. Dresselhaus, and M. S. Dresselhaus, Phys. Rev. B **45**, 768 (1992).

[10] S. Hunsche, K. Wienecke, T. Dekorsy, and H. Kurz, Phys. Rev. Lett. **75**, 1815 (1995).

[11] M. Hase, K. Mizoguchi, H. Harima, and S. -i. Nakashima, Phys. Rev. B **58**, 5448 (1998).

[12] M. F. DeCamp, D. A. Reis, P. H. Bucksbaum, and R. Merlin, Phys. Rev. Lett. **64**, 092301 (2001).

[13] M. Born and J. R. Oppenheimer, *"Zur Quantentheorie der Molekeln" [On the Quantum Theory of Molecules]*; Annalen der Physik (in German) **389** 457 (1927).

[14] W. G. Richards and J. A. Horsley, *Ab Initio Molecular Calculations for Chemists*; Oxford University Press: London, pp 1-40, 1970.

[15] P. Hohenberg and W. Kohn, Phys. Rev. **136(3B)**, 864 (1964).

[16] W. Kohn and L. J. Sham, Phys. Rev. **140(4A)**, 1133 (1965).

[17] D. M. Ceperley and B. J. Alder, Phys. Rev. Lett. **45**, 566 (1980).

[18] J. P. Perdew and Y. Wang, Phys. Rev. B **33**, 8800 (1986).

[19] J. P. Perdew, K. Burke, and M. Ernzerhof, Phys. Rev. Lett. **77**, 3865 (1996).

[20] J. C. Slater, Phys. Rev. **51**, 846 (1937).

[21] D. J. Singh, *Planewaves, Pseudopotentials and the LAPW method*, Kluwer Academic Publishers, Boston, 1994.

[22] http://en.wikipedia.org/wiki/Pseudopotential

[23] S. Geodecker, M. Teter, and J. Hutter, Phys. Rev. B **54**, 1703 (1996).

[24] C. Hartwigsen, S. Geodecker, and J. Hutter, Phys. Rev. B **58**, 3641 (1998).

[25] S. Obera and A. Saika, J. Chem. Phys. **84**, 3963 (1986).

[26] M. H-. Gordon and J. A. Pople, J. Chem. Phys. **89**, 5777 (1988).

[27] E. S. Zijlstra, T. Zier, B. Bauerhenne, S. Krylow, P. M. Geiger, and M. E. Garcia, Appl. Phys. A **114**, 1 (2014).

[28] E. S. Zijlstra, N. Huntemann, A. Kalitsov, M. E. Garcia, and U. v. Barth, Modelling Simul. Mater. Sci. Eng. **17**, 015009 (2009).

[29] J. VandeVondele and J. Hutter, J. Chem. Phys. **127**, 114105 (2007).

[30] J. P. Perdew and Y. Wang, Phys. Rev. B **45**, 13244 (1992).

[31] H. O. Jeschke, M S. Diakhate, and M. E. Garcia, Appl. Phys. A **96**, 33 (2009).

[32] U. Zastrau *et al.*, Phys. Rev. E **81**, 026406 (2010).

[33] K. Widmann, T. Ao, M. E. Foord, D. F. Price, A. D. Ellis, P. T. Springer, and A. Ng, Phys. Rev. Lett. **92**, 125002 (2004).

[34] U. Zastrau *et al.*, Phys. Rev. E **78**, 066406 (2008).

[35] R. R. Fäustlin *et al.*, Phys. Rev. Lett. **104**, 125002 (2010).

[36] R. Davidson, *Frontiers in High Energy Density Physics: The X-Games of Contemporary Science.* (National Academic Press, 2003).

[37] T. Guillot, Science **286**, 72 (1999).

[38] M. Ross, Nature (London) **292**, 435 (1981).

[39] M. Koenig *et al.*, Appl. Phys. Lett. **72**, 1033 (1998).

[40] R. Ernstorfer, M. Harb, C. T. Hebeisen, G. Sciaini, T. Dartigalongue, and R. J. D. Miller, Science **323**, 1033 (2009).

[41] C. E. Starrett, and D. Saumon, Phys. Rev. E **87**, 013104 (2013).

[42] U. Zastrau *et al.*, Laser and Particle Beams **30**, 45 (2012).

[43] B. Nagler *et al.*, Nature Physics **5**, 693 (2009).

[44] S. M. Vinko *et al.*, Nature Physics **482**, 59 (2012).

[45] S. M. Vinko *et al.*, Phys. Rev. Lett. **104**, 225001 (2010).

[46] P. A. Loboda, N. A. Smirnov, A. A. Shadrin, and N. G. Karlykhanov, High Energy Density Physics **7**, 361 (2011).

[47] http://www-als.lbl.gov/index.php/about-the-als/als-in-the-news/657

[48] E. S. Zijlstra, F. Cheenicode Kabeer, B. Bauerhenne, T. Zier, N. Grigoryan, and M. E. Garcia, Appl. Phys. A **110**, 519 (2013).

[49] F. Cheenicode Kabeer, E. S. Zijlstra, and M. E. Garcia, Phys. Rev. B **89**, 100301(R) (2014).

[50] E. S. Zijlstra, A. Kalitsov, T. Zier, and M. E. Garcia, Phys. Rev. X. **3**, 011005 (2013).

[51] P. Blaha, K. Schwarz, G. K. H. Madsen, D. Kvasnicka, and J. Luitz, *WIEN2k, An Augmented Plane Wave + Local Orbitals Program for Calculating Crystal Properties* (Karlheinz Schwarz, Techn. Universität Wien, Austria, 2001).

[52] N. D. Mermin, Phys. Rev. **137**, A1441 (1965).

[53] J. J. Vanderwal, J. Phys. C: Solid State Phys. **10**, 525 (1977).

[54] E. C. Svensson, B. N. Brockhouse, and J. M. Rowe, Phys. Rev. **155**, 619 (1967).

[55] M. Harb *et al.*, Phys. Rev. Lett. **100**, 155504 (2008).

[56] S. Mazevet, J. Clérouin, V. Recoules, P. M. Anglade, and G. Zerah, Phys. Rev. Lett. **95**, 085002 (2005).

[57] V. Recoules, J. Clérouin, G. Zerah, P. M. Anglade, and S. Mazevet, Phys. Rev. Lett. **96**, 055503 (2006).

[58] G. E. Norman, I. Yu. Skobelev, and V. V. Stegailov, Contrib. Plasma Phys. **51**, 411 (2011).

[59] P. Celliers, A. Ng, G. Xu, and A. Forsman, Phys. Rev. Lett. **68**, 2305 (1992).

[60] D. Riley, N. C. Woolsey, D. McSherry, I. Weaver, A. Djaoui, and E. Nardi, Phys. Rev. Lett. **84**, 1704 (2000).

[61] A. Mančić *et al.*, Phys. Rev. Lett. **104**, 035002 (2010).

[62] See, for example, W. P. Scheich: "Quantum Optics in Phase Space" (Wiley, Berlin, 2001).

[63] Ö. E. Müstecaploglu and A. S. Shumovsky, Appl. Phys. Lett. **70**, 3489 (1997).

[64] H. Vahlbruch, M. Mehmet, N. Lastzka, B. Hage, S. Chelkowski, A. Franzen, S. Gossler, K. Danzmann, and R. Schnabel, Phys. Rev. Lett. **100**, 033602 (2008).

[65] H. P. Yuen and J. H. Shapiro, IEEE Trans. Inf. Theory **24**, 657 (1978).

[66] C. M. Caves, Phys. Rev. D **23**, 1693 (1981).

[67] See, for example, the special issue on squeezed states, Appl. Phys. B, 55, No. 3 (1992).

[68] D. E. Reiter, S. Sauer, J. Huneke, T. Papenkort, T. Kuhn, A. Vagov, and V. M. Axt, J. Phys.: Conf. Ser. **193**, 012121 (2009).

[69] J. M. Daniels, T. Papenkort, D. E. Reiter, T. Kuhn, and V. M. Axt, Phys. Rev. B **84**, 165310 (2011).

[70] V. A. Kovarski, phys. stat. sol. (b) **175**, K77 (1993).

[71] T. Papenkort, V. M. Axt, and T. Kuhn, Phys. Rev. B **85**, 235317 (2012).

[72] J. Janszky and A. V. Vinogradov, Phys. Rev. Lett. **64**, 2771 (1990).

[73] A. Zazunov, D. Feinberg, and T. Martin, Phys. Rev. Lett. **97**, 196801 (2006).

[74] M. Artoni and J. L. Birman, Phys. Rev. B **44**, 3736 (1991).

[75] X. Hu and F. Nori, Phys. Rev. B **53**, 2419 (1996).

[76] B. G. Levi, Physics Today **5**0, 18 (1997).

[77] D. A. Reis, Physics **2**, 33 (2009).

[78] G. A. Garrett, J. F. Whitaker, A. K. Sood, and R. Merlin, Optics Express **1**, 385 (1997).

[79] P. Stampfli, and K. H. Bennemann, Phys. Rev. B **42**, 7163 (1990).

[80] K. H. Bennemann, J. Phys.: Condens. Matter **23**, 073202 (2011).

[81] E. S. Zijlstra, L. E. Díaz-Sánchez, and M. E. Garcia, Phys. Rev. Lett. **104**, 029601 (2010).

[82] M. Ligges *et al.*, Appl. Phys. Lett. **94**, 101910 (2009).

[83] F. Cheenicode Kabeer, N. S. Grigoryan, E. S. Zijlstra, and M. E. Garcia, Phys. Rev. B **90**, 104303 (2014).

[84] N. S. Grigoryan, E. S. Zijlstra, and M. E. Garcia, New J. Phys. **16**, 013002 (2014).

[85] N. D. Mermin, Phys. Rev. **137**, A1441 (1965).

[86] S. I. Anisimov, B. L. Kapeliovich, and T. L. Perelman, Sov. Phys. JETP **39**, 375 (1974).

[87] `http://www.faculty.virginia.edu/CompMat/electron-phonon-coupling/`

[88] S. L. Johnson *et al.*, Acta. Cryst. A **66**, 157 (2010).

[89] M. Trigo *et al.*, Phys. Rev. B **82**, 235205 (2010).

[90] M. Trigo *et al.*, Nat. Phys. **9**, 790 (2013).

[91] O. V. Sergeev and V. V. Stegailov, in *Physics of Extreme States of Matter*, edited by V. E. Fortov *et al.*, (Institute of Problems of Chemical Physics, Chernogolovka, 2011).

[92] T. Hertel, E. Knoesel, M. Wolf, and G. Ertl, Phy. Rev. Lett. **76**, 535 (1996).

[93] F. Schmitt, P. S. Kirchmann, U. Bovensiepen, R. G. Moore, L. Rettig, M. Krenz, J. -H. Chu, N. Ru, L. Perfetti, D. H. Lu, M. Wolf, I. R. Fisher, and Z. -X. Shen, Science **321**, 1649 (2008).

[94] D. M. Fritz, D. A. Reis, B. Adams, R. A. Akre, J. Arthur, C. Blome, P. H. Bucksbaum, A. L. Cavalieri, S. Engemann, S. Fahy *et al.*, Science **315**, 633 (2007).

[95] Y. Liu and E. Allen, Phy. Rev. B **52**, 1566 (1995).

[96] K. Ishioka, M. Kitajima, and O. V. Misochko, J. Appl. Phys. **103**, 123505 (2008).

[97] E. S. Zijlstra, T. Zier, B. Bauerhenne, S. Krylow, P. M. Geiger, and M. E. Garcia, Appl. Phys. A **114**, 1 (2014).

[98] Y. Giret, A. Gellé, and B. Arnaud, Phy. Rev. Lett. **106**, 155503 (2011).

[99] E. S. Zijlstra, L. L. Tatarinova, and M. E. Garcia, Phys. Rev. B **74**, 220301 (2006).

[100] T. K. Cheng, J. Vidal, H. J. Zeiger, G. Dresselhaus, M. S. Dresselhaus, and E. P. Ippen, Appl. Phys. Lett. **59**, 1922 (1991).

[101] E. S. Zijlstra, N. Huntemann, and M. E. Garcia, New J. Phys. **10**, 033010 (2008).

[102] X. Wang, K. Kunc, I. Loa, U. Schwarz, and K. Syassen, Phys. Rev. B **74**, 134305 (2006).

[103] É. D. Murray, D. M. Fritz, J. K. Wahlstrand, S. Fahy, and D. A. Reis, Phys. Rev. B **72**, 60301 (2005).

[104] O. V. Misochko, K. Ishioka, M. Hase, and M. Kitajima, J. Phys.: Condens. Matter **18**, 10571 (2006).

[105] O. V. Misochko, M. Hase, K. Ishioka, and M. Kitajima, Phy. Rev. Lett. **92**, 197401 (2004).

[106] M. S. Diakhate, E. S. Zijlstra, and M. E. Garcia, Appl. Phys. A **96**, 5 (2009).

[107] P. Baum, D. -S. Yang, and A. H. Zewail, Science **318**, 788 (2007).

[108] U. Häussermann, K. Söderberg, and R. Norrestam, J. Am. Chem. Soc. **124**, 15359 (2002).

[109] J. J. Li, J. Chen, D. A. Reis, S. Fahy, and R. Merlin, Phys. Rev. Lett. **110**, 047401 (2013).

[110] D. Fausti, O. V. Misochko, and P. H. M. van Loosdrecht, Phys. Rev. B **80**, 161207(R) (2009).

List of symbols and abbreviations

Abbreviations	*Details*
XUV	Extreme ultraviolet
DFT	Density functional theory
LA	Longitudinal acoustic
CHIVES	Code for Highly-excIted Valence Electron Systems
WDM	Warm dense matter
HF	Hartree-Fock
LDA	Local density approximation
GGA	Generalized gradient approximation
MT	Muffin-tin
I	Interstitial region
APW	Augmented plane wave
LAPW	Linearized augmented plane wave
LO	Local orbital
GTH	Geodecker-Teter-Hutter
AFC	Atomic force constants
FCC	Face centered cubic
BZ	Brillouin zone
DOS	Density of state
TTM	Two-temperature model

Symbols	***Details***
T_e	Electronic temperature
T_l	Lattice temperature
N	Number of atoms in supercell
t	Time
s	Seconds
ps	Picoseconds
fs	Femtoseconds
K	Kelvin
m	Meter
cm	Centimeter
J	Joules
R	Atomic coordinate
r	Electronic coordinate
M	Atomic mass
m_e	Electronic mass
$\hat{T}$	Kinetic energy
$\hat{V}$	Potential energy
F_{HK}	Hohenberg-Kohn functional
$\hat{H}_{KS}$	Kohn-Sham Hamiltonian
V_{xc}	Exchange-correlation potential
ρ	Density
ψ	Wave function
ϕ	Single-particle wavefunction
ψ_{pseudo}	Pseudowavefunction
V_{pseudo}	Pseudopotential
R_{MT}	Muffin-tin radius
S_{MT}	Muffin-tin sphere
l	Angular momentum quantum number
ϵ_m	Kohn-Sham energy
k_{max}	Plane wave cutoff
erf	Error function
Z_{ion}	Ionic charge
r_{loc}	Local radius
S_e	Electronic entropy
a_0	Bohr units
F_e	Helmholtz free energy
$n(\epsilon_m, t)$	Occupation of Kohn-Sham level

$D(\mathbf{q})$	Dynamical matrix
$\mathbf{q}$	Phonon wavevector
ω	Phonon frequency
ϵ	Phonon eigenvector
Q	Phonon normal coordinate
P	Phonon momentum
$\langle Q^2 \rangle$	Variance of the atomic displacement
S	Squeezing factor
k_B	Boltzmann's constant
E_F	Fermi energy
$\hbar$	Planck's constant
C_e	Electronic heat capacity
C_l	Lattice heat capacity
G	Electron-phonon coupling
E_{band}	Band energy
A_{1g}	Totally symmetric mode of Peierls distorted structure
T_D	Debye temperature
z	Internal coordinate of $A7$ crystal structure
v	Velocity
u	Displacement
N_{runs}	Number of runs
τ	Decay time
V^{ph-ph}	Potential energy of phonon modes
THz	Terahertz
GPa	Gigapascals
δ	Kronecker delta function

Publications based on this thesis

1. *Modeling of material properties after ultrashort laser and XUV excitation,*
   E. S. Zijlstra, F. Cheenicode Kabeer, B. Bauerhenne, T. Zier, N. S. Grigoryan, and M. E. Garcia,
   Appl. Phys. A **110**, 519 (2013).

2. *Road of warm dense noble metals to the plasma state: Ab initio theory of the ultrafast structural dynamics in warm dense matter,*
   F. Cheenicode Kabeer, E. S. Zijlstra, and M. E. Garcia,
   Phys. Rev. B **89**, 100301(Rapid Communication) (2014).

3. *Transient phonon vacuum squeezing due to femtosecond-laser-induced bond hardening,*
   F. Cheenicode Kabeer, N. S. Grigoryan, E. S. Zijlstra, and M. E. Garcia,
   Phys. Rev. B **90**, 104303 (2014).

4. *Decay paths of coherent phonons in antimony,*
   F. Cheenicode Kabeer, E. S. Zijlstra, and M. E. Garcia,
   (in preparation).

Selected conferences and workshops attended

- *Summer School 2011 on Exciting Excitations: From Methods to Understanding*, Waldbreitbach, Germany,
  (July, 2011) [poster].
- *CINSAT Herbstkolloquium*, University of Kassel, Germany,
  (October, 2011) [poster].
- *Deutsche Physikalische Gesellschaft (DPG) Spring Meeting*, Berlin, Germany,
  (March, 2012) [talk].
- *School on Efficient Algorithms in Computational Physics*, Bad Honnef, Germany,
  (September, 2012).
- *CINSAT Frühjahrskolloquium*, Friedrichroda, Germany,
  (February, 2013) [poster].
- *Deutsche Physikalische Gesellschaft (DPG) Spring Meeting*, Regensburg, Germany,
  (March, 2013) [talk].
- *Deutsche Physikalische Gesellschaft (DPG) Spring Meeting*, Berlin, Germany,
  (March, 2014) [talk].
- *Workshop on System far from equilibrium : from solid states physics to warm dense matter*, Institut Poincaré, Paris,
  (June, 2014) [talk].
- *HoW exciting! Hands-on Workshop on Excitations in Solids 2014*, Humboldt Universität zu Berlin, Germany,
  (August, 2014) [poster].

Fellowships, Honours and Awards

2011-2014	Promotionsstipendium der Universität Kassel, Germany.
2010	Marie Curie Initial Training Fellowship, IFIN-HH, Romania.
2009	Cleared Graduate Aptitude Test in Engineering (GATE), India.
2008	First rank in M. Sc Physics, Department of Physics, Calicut University, Kerala, India.
2006	Fourth rank in B. Sc Physics in Calicut University, Kerala, India.